Uncertainties in proton therapy:

Analysis of the effects of density changes, calibration curve errors and setup errors in proton dose distributions.

A treatment planning study performed on water phantoms and craniospinal treatment plans.

Grete May Engeseth

Master thesis in Health Sciences

Faculty of Medicine and Dentistry

Department of Public Health and Primary Care

University of Bergen

2014

Acknowledgements

CONTENTS

ABSTRACT

Aim: To analyse the dosimetric effects of density changes, calculation curve errors and geometric errors in proton dose distributions.

Methods: Single field optimized treatment plans were created on homogenous and heterogeneous water phantoms. Intensity modulated craniospinal treatment plans were created on CT image data sets from 6 pediatric patients. Setup errors were simulated by shifting the isocenter for ±1 to ±5 mm along the x-, z-and y-axis. Calibration curve errors were simulated by increasing or decreasing the relative stopping power by 1% to 5%. Density changes were simulated by introducing bone and air in the beam path.

Result: Air and bone resulted in a change in proton range with a factor of +0,94 and – 0,48, respectively. The $V_{95\%}$ was >97% for the CTV regardless of any setup-and calibration curve error, though hotspots and cold spots occurred in the brain. A 3% overshoot caused an increased of 47% in the D_{mean} for the thyroid.

Conclusion: Density changes caused severe alterations of the proton range. Error-induced dose disturbances emerged mainly in areas of complex tissue heterogeneities. Following setup-and calibration curve errors, significant dose escalation were observed for organs at risk in close proximity to the target volume.

Keywords: radiotherapy, proton, active scanning technique, intensity modulated proton therapy, IMPT, range uncertainty, density changes, setup errors, craniospinal irradiation, pediatric.

1 INTRODUCTION

1.1 Radiation therapy

Radiation therapy plays an important role in the fight against cancer, either as the preferred primary treatment or adjuvant to surgery and/or chemotherapy. Conventional radiotherapy with photons and electrons are well known and established modalities. During the last decades the radiation treatment technology has evolved rapidly. With the development of advanced treatment delivery techniques like Intensity Modulated Radiation Therapy (IMRT) (1) and Volumetric Modulated Arc Therapy (VMAT) (2), highly sophisticated treatment plans can be designed and delivered. Less common than conventional radiotherapy with photons is radiotherapy with protons. The use of protons in cancer treatment was proposed by Robert R. Wilson in a paper published in Radiology as early as 1946 (3), and used for cancer treatment for the first time 8 years later at the Lawrence Berkeley Laboratory. Today proton therapy is the subject of increasing interest, both worldwide and in Norway. Norway is at present in the beginning of the planning stage in preparing of several regional proton therapy facilities. Globally there are approximately 40 proton centers in operation, and several more are under construction and in the planning phase. As of the end of 2012 around 94 000 patients have received radiotherapy with protons (4).

The main goal of any radiation therapy technique is to deliver sufficient high dose to kill the tumor cells and at the same time spare normal organs and healthy tissue as much dose as possible. The main rationale for using proton beams in cancer treatment is for the most part its favourable physical properties; the deposition of the major proportion of the dose within a few millimetres in a well defined depth (the Bragg Peak), followed by a sharp dose fall-off and a subsequent negligible dose deposition thereafter. This allows for sparing of normal tissue and organs at risk, and at the same time achieve adequate target dose coverage and dose conformity. Typical treatment sites for which applying proton therapy is considered advantageous are the central nervous system, the lungs, the gastrointestinal canal, for the prostate, for ocular melanomas, for head and neck and for paediatric cancers. When it comes to the clinical evidence of proton therapy, current data are not sufficient to conclude that the proton therapy is superior to over conventional radiotherapy for most diagnosis. For chordomas, however, there is evidence for better outcome with protons

compared to photons; this also applies for ocular melanomas. For prostate and hepatocellular carcinoma there is evidence for the efficacy of proton therapy, but not enough to claim that this modality provides a better standard of care than advanced photon therapy techniques. For malignancies in the Central Nervous System (CNS) in paediatric patients, the results are promising, but here also still too few clinical trials have been conducted and one cannot yet conclude (5). However, dose planning studies performed with the intention to compare proton and photon dose distributions, clearly demonstrates superior normal tissue sparing, decreased integral dose with protons and excellent dose coverage, especially in the treatment of the brain and the spinalcanal (craniospinal irradiation) (6, 7). The latter is important, considering that the risk of late effects and second cancer is dose dependent, and well documented for this patient group (8).

Thus, proton therapy may offer treatment plans with improved dose conformation to the target volume, sparing of critical structures and reduction of integral dose to healthy tissue. However, in proton therapy several uncertainties exist that have to be addressed both during planning and execution of the treatment. Proton therapy is, as photon therapy is, commonly planned based on information from Computer Tomography (CT) images. A CT scan yields cross-sectional images based on the absorption of x-rays, and provides images of high quality with detailed anatomical information, as well as a "map" over the tissue densities in the scanned volume (9). The CT scan is acquired with the patient in the treatment position and is used for the delineating of the treatment planning volumes, and for computing the depth of the proton penetration (proton range) in the patient, used for the calculation of the dose distribution in the patient. During execution of the treatment, the goal is to exactly reproduce the situation present at planning, but in every clinical situation, variations occur treatment (10, 11). Unless accounted for, any inaccuracy in the estimation of the proton range in the patient, inaccuracies in the patient positioning (setup errors), patient- and/or organ motion and anatomic changes during the radiotherapy course (weight loss, tumor shrinkage etc.) could lead to severe alterations of the planned dose distribution (12-14).

1.2   Aim and research questions

The main aim of this work has been the investigation and quantification of the potential alteration of proton dose distributions in phantoms and in patient geometries in the presence of

1) Geometric errors,

2) Proton range estimation errors and

3) Tissue density changes in the beam path.

The study is divided into a theoretical part and a clinical part.

The theoretical part is a simulation study performed on water phantoms.

The clinical part is a robustness analysis of craniospinal treatment plans.

1.2.1   Water phantom dose calculations

The following research question were investigated in the water phantom study:

I.   How does a change of tissue composition in the beam path affect the proton particle range and the depth dose distribution?

II.   How do geometric errors affect the proton dose distribution in homogenous and heterogeneous water phantoms?

1.2.2   Robustness analysis of craniospinal treatment plans

The following research questions were investigated in the robustness analysis:

I.   How do range estimation errors affect the doses to the target volume and organs at risk?

II.   How do setup errors affect the doses to target volumes and the organs at risk?

1.3   Structure of the thesis

This thesis is structured in the following way: Chapter 2 presents the theoretical background, here radiation physics, biology and technical aspects are presented, the

treatment planning process is thoroughly described and the problem of uncertainty in proton therapy is introduced and discussed. Chapter 3 describes the study and the simulation procedures. In chapter 4 the results are presented. A discussion of the results in relation to theory and previous research is done in Chapter 5. Chapter 6 contains the conclusion and possible clinical implications.

The author performed all the proton treatment planning and uncertainty simulations in this thesis. Unless otherwise specified all figures were produced by the author.

2 THEORY

2.1 Radiation physics and biology

2.1.1 The physical properties of photon beams

A photon is considered as massless and carries no electric charge. When a photon beam traverses matter interactions will occur and lead to energy being transferred from the radiation to the irradiated material. The most common interaction processes that contribute to energy absorption when irradiating matter with photons are the Photoelectric Absorption, the Compton Scattering and Pair production.

2.1.1.1 The Photoelectric Effect

The Photoelectric Effect is an inelastic collision between an incoming photon and an atomic electron. The process can occur if the photon energy is equal or larger than the binding energy of the orbital electron. The photon will be absorbed and transfer all its energy to the electron in the process. The electron is then ejected from the atom. The probability for this interaction to take place depends on the atomic number of the irradiated material and the photon energy. The probability increases with increasing atomic number and decreases with increasing photon energy (15, p. 441).

2.1.1.2 Compton Scattering

Compton Scattering occurs when an incoming photon interacts with an atomic orbital electron and being only partially absorbed in the process, so that both a photon and an electron is scattered out from the atom. The probability (the cross-section) for Compton scattering increases when the energy of the incoming photon is substantially higher than the involved electron's binding energy. The result of a Compton scattering process is that, in addition to the ionization of the atom, a scattered photon with lower energy than the incoming photons energy is emitted. The probability that this process take place is strongly dependent on the electron density of the irradiated material (15, p. 445).

2.1.1.3 Pair Production

In this process the incoming photon interacts with the field from an atomic nucleus and all its energy is absorbed as an electron and positron is produced. For Pair Production to take place the photon energy must be at least 1,022 MeV (two times the rest mass of the electron), in order to enable the creation of an electron-positron pair. In this process the incoming photon interacts with the field from an atomic nucleus and all its energy is absorbed when an electron and positron is produced. The probability that this interaction occurs is a function of increases with a higher atomic number and photon energy (15, p. 449).

2.1.1.4 Beam attenuation

The interaction processes described above will be the main contributors to an attenuation of the intensity of a photon beam traversing through a medium, as photons from the incoming beam interacts with matter and their energy is either totally or partially transferred to the medium. The beam attenuation is described by

$$I(x) = I_0^{-\mu x}$$
(Equation 2-1)

with I_0 being the incident beam intensity, x being the absorber thickness, μ being the linear attenuation coefficient of the irradiated material and $I(x)$ being the beam intensity at a certain depth x in the traversed matter. The attenuation of a photon beam is illustrated in Figure 2-1, which shows the depth dose curve for 6 MV and 18MV photon beams. As the photon beam enters a material there will be a dose build up region in which the dose increases until it reaches a dose maximum in a certain position in depth. The position in depth of the dose maximum is dependent on the beam energy. Beyond this dose maximum the dose will gradually decrease in depth as a function of the interactions between the incoming photons and the structure and composition of the traversed medium.
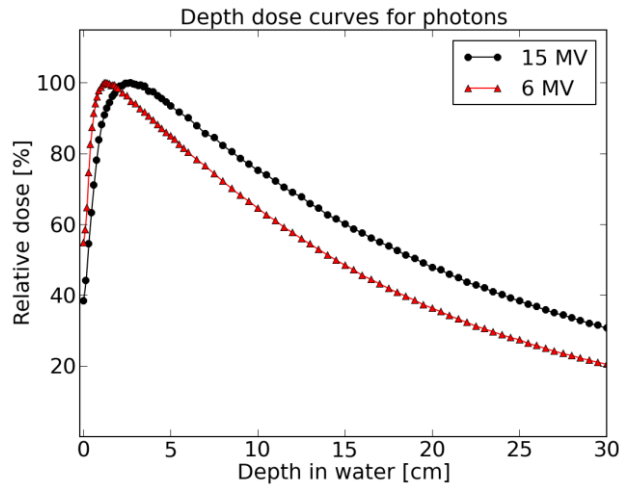
Figure 2-1: Measurements of photon beams at Haukeland University Hospital: The depth dose distribution for 6 MV and 15 MV photon beams (16).

2.1.2 The physical properties of proton beams

A proton is a subatomic particle with a positive elementary electrical charge (+ 1 e). When an electrically charged particle is traversing matter, two main effects occur in general; due to the numerous interactions with the atomic electrons and nucleons in the traversed matter the particle will a) lose energy and b) be scattered from its original path.

2.1.2.1 Energy loss and Stopping Power

The proton loses its energy primarily through inelastic collisions with the orbital electrons of atoms in the matter it traverses. These collisions result in either ionizations or excitations of the atoms, and in these processes, energy is transferred from the proton to the matter, which thus is the absorber of energy and dose. The averaged energy loss per unit path length that a proton beam experience when penetrating matter is described by the quantity Stopping Power: $\frac{dE}{dx}$ (MeV/cm) and this is given by the Bethe-Bloch formula:

$$-\frac{dE}{dx} = 2\pi N_a r^2 m_e c^2 \rho \frac{Z}{A} \frac{z^2}{\beta^2} \left[\ln\left(\frac{2m_e \gamma^2 v^2 W_{max}}{I^2}\right) - 2\beta^2 - \delta - 2\frac{C}{Z} \right] \qquad \text{(Equation 2-2)}$$

Symbol	Definition
r_e	Classical electron radius = 2.817 x 10^{-13} cm
m_e	Electron mass = 0.511MeV/c^2
N_a	Avogadro's number = 6.022 x 10^{23} mol^{-1}
I	Mean excitation energy (eV)
Z	Atomic number of absorber
A	Atomic weight of absorber (g/mol)
ρ	Density of absorber
z	Charge of incident particle in units of e
β	= v/c of incident particle (speed of particle relative to c)
γ	$1/\sqrt{(1-\beta^2)}$
W_{max}	Maximum energy transfer in a single collision
δ	Density correction
C	Shell correction

Table 2-I presents the definition of the parameters in the Bethe-Bloch equation. The energy loss is dependent on the properties of the traversing particle like the mass, the electrical charge, and its velocity, as well as the properties of the absorbing media like density, atomic weight and atomic number (17). Thus, for a proton beam traversing a material the energy loss can, as an approximation, be described as being proportional to the mass of the material and inversely proportional to the square of the velocity of the incoming proton:

$$-\frac{\Delta E}{\Delta x} \sim \frac{\rho}{v^2} \qquad\qquad\qquad \text{(Equation 2.3)}$$

In Figure 2-2 the proton Stopping Power is displayed as a function of particle energy. The figure shows the proton stopping power curves for protons traversing i) water, ii) compact

bone and iii) air. The region of the energies typically used in proton therapy, the range between 70 MeV- 275 MeV, is marked with grey.
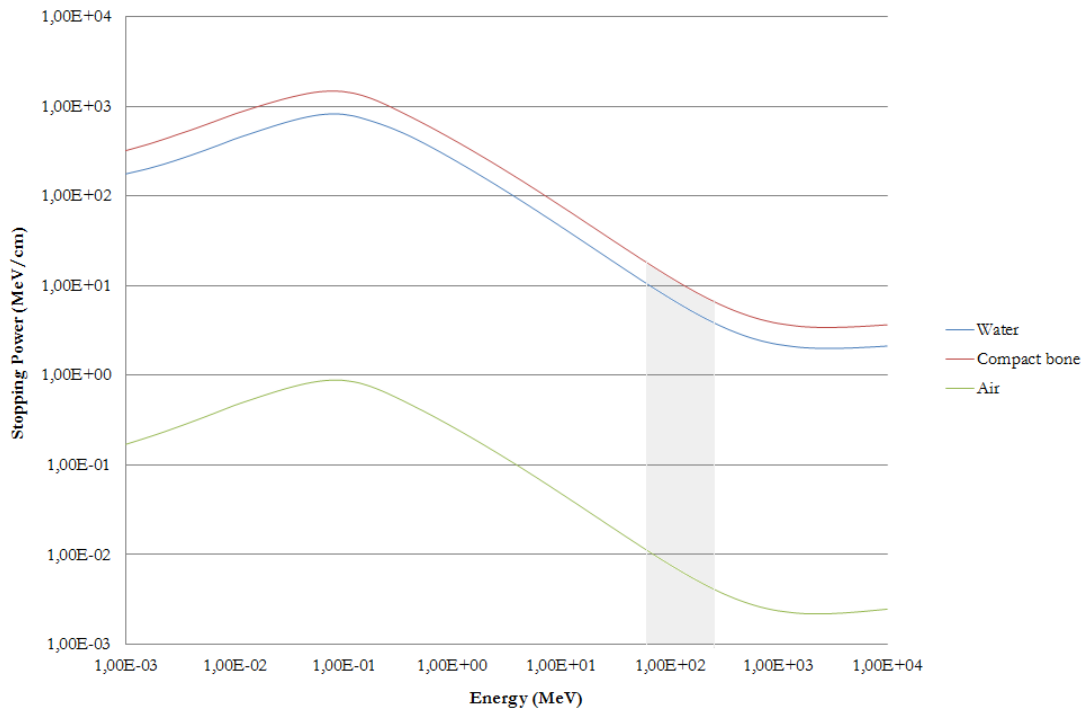
Figure 2-2: The Proton Stopping Power as a function of energy for i) water (blue line), ii) compact bone (red line) and iii) air (green line). The marked grey area is the energy levels used for patient treatment. The plot is based on PSTAR data from (18).

The energy loss experienced by a particle traversing through matter will be dependent on the density and composition of the traversed matter, as we have seen. By normalizing the energy loss with respect to the mass of the traversed medium, one obtains a mass independent measure of the Stopping Power; the so-called Mass Stopping Power. The Mass Stopping Power expresses the average energy loss corrected for mass in units of MeV/g cm^{-2} and is defined as:

$$-\frac{dE}{d\varepsilon} = \frac{1}{\rho}\frac{dE}{dx}$$

(Equation 2.4)

where ρdx is the mass thickness (g/cm^2). The dependence on the absorber density is largely removed when the energy loss is expressed by the Mass Stopping Power. Consequently, the energy loss expressed in terms of mass thickness will vary little for the majority of materials involved in radiation therapy (17).

2.1.2.2 Multiple Coulomb Scattering

When an elastic interaction between a traversing proton and one of the atomic nuclei in the traversed material occurs, the proton particle will experience a very small deflection and almost no energy loss. The deflections from numerous interactions as the proton traverses the material, entails that the protons is scattered from a straight path. The amount of scattering is dependent on the atomic weight of the scattering material; a high Z-material scatters more strongly than a low Z-material (19).

2.1.2.3 The range and range straggling

The distance a particle travels in a material before it loses all its energy is called the range. The range of a proton is strongly dependent on the particle energy and the absorber material. Specifically, the depth of penetration is proportional to the square of the proton energy and scales with $\frac{1}{\rho}$ of the traversed material. The energy and absorber dependency is illustrated in Figure 2-3, which shows the range particle as a function of energy for a proton traversing i) water, ii) compact bone and iii) air.

Assuming that the energy loss a particle experience is continuous, the penetration in depth for a monoenergetic proton beam must be well defined. However, protons of a given energy do not experience an exact identical set of interactions when traversing matter, and therefore do not experience the same amount of energy loss; there will be an energy straggling. Consequently there will be a distribution of ranges for protons in a proton beam around an averaged value, rather than one sharp finite range, a phenomenon known as

range straggling (17). The uncertainty in proton range associated with the range straggling scales with the depth traversed and is approximately 1,2 % of the projected range (20, p. 36).
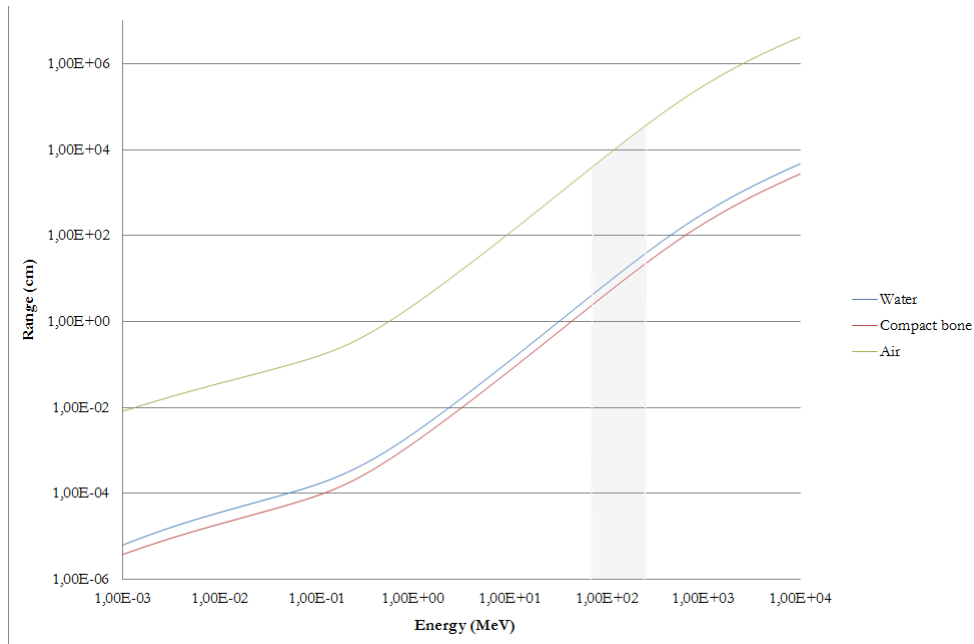
Figure 2-3: Proton particle range in i) water (blue line), ii) bone (red line) and iii) air (green line). Energy (MeV) is displayed on the x-axis and range (cm) on the y-axis. The plot is based on data (measurements) from (18).

2.1.2.4 The pristine Bragg peak

In Figure 2-4 the depth dose curve for 107 MeV protons is displayed. As the Bethe-Bloch equation shows, the rate of energy loss is approximately inversely proportional to the square of the velocity of the traversing particle. This means that in the entrance region of the beam path, where the particle energy and velocity is at its greatest, the energy deposition is small. As the particle traverses the matter and experiences numerous interactions, the velocity of the particle decreases, which in turn causes the probability of ionizations and excitations to increase. Consequently, towards the end of its range, the energy deposition for a charged particle increases rapidly and reaches a maximum, called the Bragg Peak, after which the dose is negligible as the particle comes to rest in the tissue.

16

The position in depth of the Bragg Peak in any material is directly proportional to the initial energy of the particle (19).
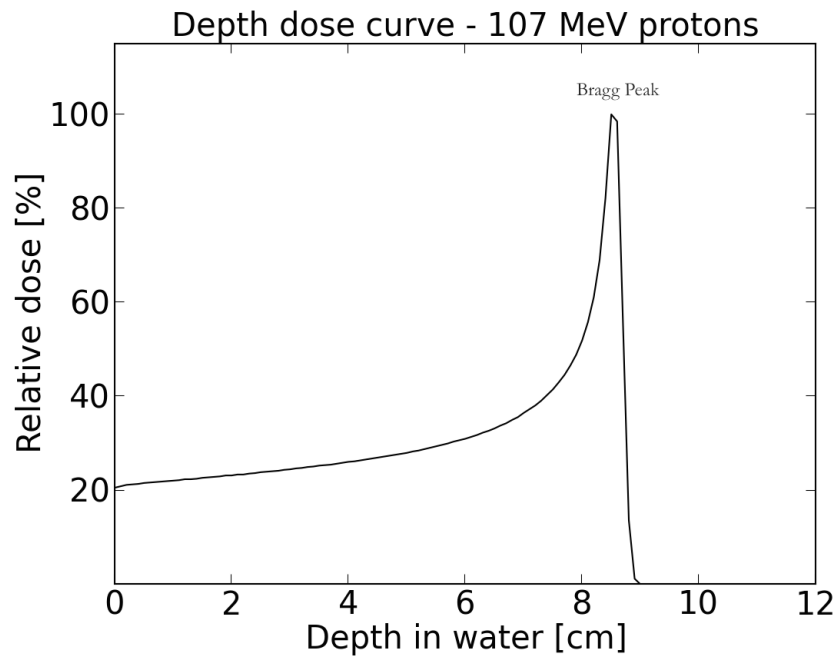
Figure 2-4: FLUKA Monte Carlo simulations: The depth dose curve in water for 107 MeV protons. The Figure shows that the dose deposition is low at the entrance region, and then increases rapidly towards the end of the particle range, and then a maximum dose deposition in the Bragg Peak before the protons come to rest. The image is from (16).

2.1.3   The Linear Energy Transfer

The ionization density, produced by ionization radiation in tissue is expressed in terms of the entity the Linear Energy Transfer (LET) of the ionizing beam. The LET expresses the linear rate of energy transferred from the beam to an absorbing media and is given by keV/μm;

$$LET\left(\frac{keV}{\mu m}\right) = \frac{dE}{dx}$$ (Equation 2.5)

where *dE* is the average energy locally imparted to the medium by a charged particle of a specified energy traversing a distance of *dx* in the material. The associated *LET* value of a certain beam particle will thus describe the quality of the beam in terms of its ionization capacity. Different types of beam particles will have different *LET* values, and the different particles are divided into two main categories; high *LET* particles (densely ionizing) and low *LET* particles (sparsely ionizing) (21). Protons are low-*LET* radiation with a relatively low ionization density at the beginning of their entrance, at the surface of the matter. The *LET* capacity is strongly coupled to the Stopping Power, thus it varies with and proportional to the velocity of the particles and varies consequently with the depth in matter. Along the particle path, the ionization density increases first slowly, then rapidly near the end of the beam range, thus forming a quite narrow region of high ionization density in the Bragg peak area (19, p. 21).

2.1.4   Absorbed dose and the RBE-weighted absorbed dose

Absorbed dose *(D)* is defined as the amount of energy absorbed per unit mass of the matter irradiated. It is expressed by the formula:

$$D = \frac{\Delta E}{\Delta m}$$
(Equation 2.6)

In this equation ΔE reflects the energy deposited by ionization radiation to a unit of mass Δm. The dose is expressed in Gy (Joule/kg) (22, p. 72). The same amount of physically deposited dose from different types of radiation does not necessarily produce an equal biologic effect in the irradiated tissue. The effect ionizing radiation have in a specific biological material is *LET* dependent, and also influenced by factors such as the dose and the individual energy of the irradiating beam particles amongst, other. The ratio between the biological effectiveness of two different types of ionization radiation is defined as the Relative Biological Effectiveness (*RBE*) and this is expressed by

$$RBE = \frac{D_x}{D_R}$$
(Equation 2.7)

Here the D_x is the dose from a radiation of a reference particle type (i.e. photons), and the D_R is the dose of the radiation with particle type *R* (e.g. protons) that causes the same

amount of biological damage as the reference radiation type (23, p. 261). Compared to photons, protons have a somewhat higher biologically effectiveness. This means that a lower dose with proton therapy is needed to cause an equal biological effect as that originating from photons. To define what dose from protons that will produce an identical biological effect as a certain dose from photons, given otherwise identical conditions, the *RBE*-weighted dose is defined as:

$$D_{RBE} = RBE {\times} D \hspace{4cm} \text{(Equation 2.8)}$$

In this equation the D_{RBE} is the RBE-weighted dose and the D is the physical proton dose in Gy. The unit of the RBE-weighted dose is Gy(RBE), which is applied in order is to distinguish between physical dose and RBE weighted dose (23, p. 261). The RBE-weighted dose is needed for comparisons of the effect of photon vs. proton irradiation, for the selection of appropriate proton doses and the prediction of therapeutic outcomes based on previous clinical experience with photons. It is well known that the RBE is not a fixed value, but varies over the physical depth dose curve, and also varies with tissue type and with the fraction size (23, p. 262). The use of a single (generic) RBE value of 1.1 for clinical use is, however, still recommended by ICRU, as expressed in ICRU report 78 (19, p. 28).

2.2   Photon beam production and delivery techniques

The two main elements of a linac are the beam producing component and the delivery unit: a rotating gantry (360°). In the beam producing part, electrons are injected and accelerated with an electric field. In photon mode, a metal target is inserted into the accelerated electrons' beam path, resulting in the production of bremsstrahlung x-rays in this target, the photon field further collimated from the target and onwards, towards the patient. In electron mode, the metal target is not applied and the electron field is collimated from the exit of the accelerating structure onwards, towards the patient. In the gantry, the beam is shaped on its way towards the patient by metal collimators, and shaped to the target volume by movable collimator jaws, so called Multi Leaf Collimators (MLC's) or metal blocks and extended electron collimators, to a distance only a few centimetres away from the surface of the patient. Other components of a linear accelerator treatment unit are the treatment coach and the image guidance devices. At modern linacs 2D and 3D image guidance equipment are integrated as a part of the treatment machine (24, p. 86).

In advanced radiotherapy the dose distribution is normally planned based on a definition of volumes of interest in a 3DCT image dataset, and delivered by 3-Dimensional Conformal Radiation Therapy (3DCRT), by Intensity Modulated Radiation Therapy (IMRT) or as Volumetric Modulated Arc Therapy (VMAT). The least sophisticated technique amongst these three, the 3DCRT, applies a highly conformal dose distribution delivered by a number of open fields of uniform intensity or by wedged fields applying a simple modification of the beam fluence across the field. The dose distribution is generated by so-called forward treatment planning, where the number of fields, the field angles, the field shaping by MLC or blocks and the field weighting are manually chosen by the user, and thereafter the dose distribution is calculated (25, p. 266). The IMRT and the VMAT techniques utilizes an invers treatment planning approach, where, the dose distribution is generated based on an initial optimization of several beam parameters in order to achieve a pre-determined goal for the plan through a set of predefined dose volume constraints and objectives. Both the VMAT and IMRT techniques have the capacity to deliver concave dose distributions and at the same time provide sparing of normal tissue through an optimization of the beam fluence given a set of fields to be applied. IMRT is delivered field by field with fixed gantry positions; either by multiple segments shaped by the MLCs (step-and –shoot or segmental MLC) or by pairs of opposing MLC leaves swiping across the fields (sliding window or dynamic MLC) (1). VMAT is the most complex and advanced technique in photon therapy. The dose distribution is delivered while the gantry is rotated around the patient, thus the name Arch Therapy is also applied for this technique. The dose rate, the gantry speed, the MLC shape; the opening and swiping –orientation, are parameters that are varied during the rotation of the gantry (26).

2.3 Proton beam production and delivery techniques

In Figure 2-5 the different parts of a proton treatment facility is shown. The production of the proton beam takes place in a particle accelerator, with a cyclotron or with a synchrotron [1] that can accelerates the beam particles to the energy level sufficient for treating deep-seated target volumes. Most common accelerators for proton therapy worldwide are cyclotrons, which produce high intensity beams with fixed energy. Synchrotrons that produce beams with pulsed energy are larger and not so widely applied in proton therapy facilities, however, at facilities offering carbon ion treatment, the

accelerators are synchrotrons. Magnets in the beam transport lines [2] are used to steer the beam into the treatment rooms. The treatment is delivered using rotating gantries [3] or by using horizontal or vertical fixed beam lines [4]. As for photon treatment rooms, at proton facilities, the treatment rooms also include a (robotic) treatment coach, as well as image guidance equipment.

Two main treatment techniques exist today for the deliverance of proton therapy: i) the passive scattering technique and ii) the active scanning technique, with the passive scattering technique being the most common technique as of 2014. Most emphasis is at present placed on the development of the active scanning technique, and it is expected that this technique will be the main delivery technique in the future.
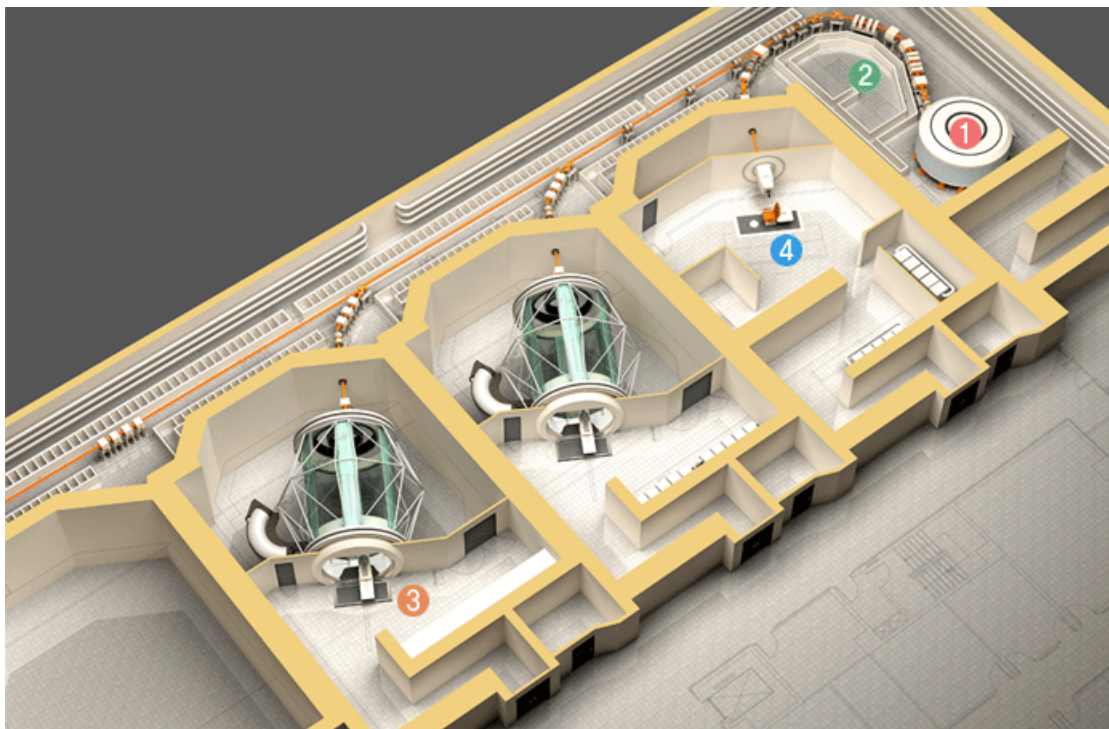
Figure 2-5: Schematic overview over a proton therapy facility which displays 1) the accelerator, here a cyclotron, 2) the transport beam lines, 3) the treatment rooms with rotating gantry and 4) the treatment room with fixed beam. Image from (27).

2.3.1 Range modulation: the Spread Out Bragg Peak

The output from the particle accelerator is a quite narrow near-monoenergetic beam of protons, a so-called pencil beam, which when penetrating matter forms a pristine Bragg Peak which is not wide enough in depth to cover most treatment volumes (see Figure 2-4). In order to deliver proton beams suitable for treating patients, the beam has to be shaped and modulated, and importantly, it has to be broadened in depth, in the beam direction through a patient. This is accomplished by combining several pristine Bragg Peaks of varying energy (range) and sum up their contributions to a treatment beam by applying a relative weight for each pristine Bragg Peak. The net result of this composition is a spread out dose plateau region referred to as the Spread Out Bragg Peak (SOBP). For the passive scattering technique the range modulation results in a flat SOBP, illustrated in Figure 2-6, providing a uniform high dose plateau across the field. The active scanning techniques can accomplish arbitrary shapes of the SOBP curve due to the individual optimizing of each pristine Bragg Peak, thus creating a non-uniform high dose plateau across the field, as illustrated in Figure 2-7 (28).
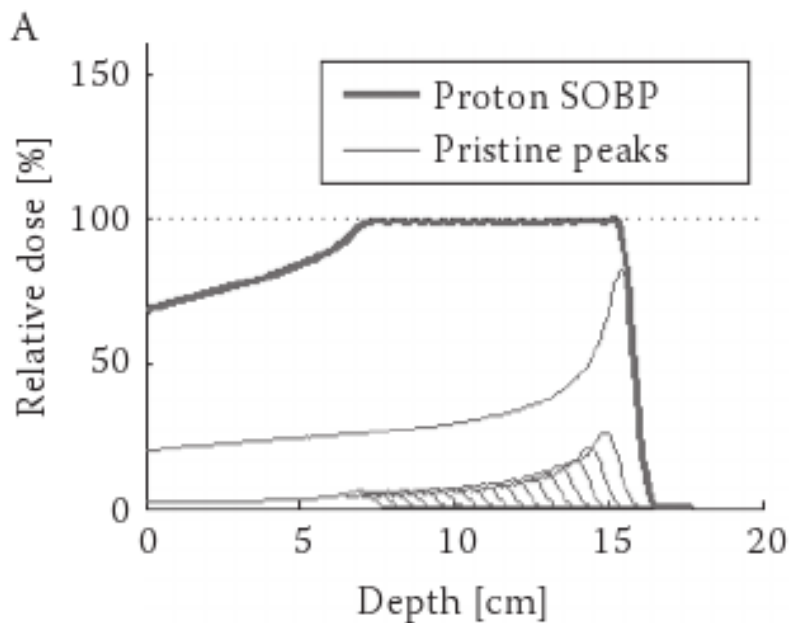
Figure 2-6: A flat Spread Out Bragg Peak (SOBP): Pristine Bragg Peaks of different weights are superimposed in order to form a flat SOBP with the highest weighted Bragg Peaks positioned deepest, providing in sum a uniform SOBP dose plateau (along the beam axis.) (28).
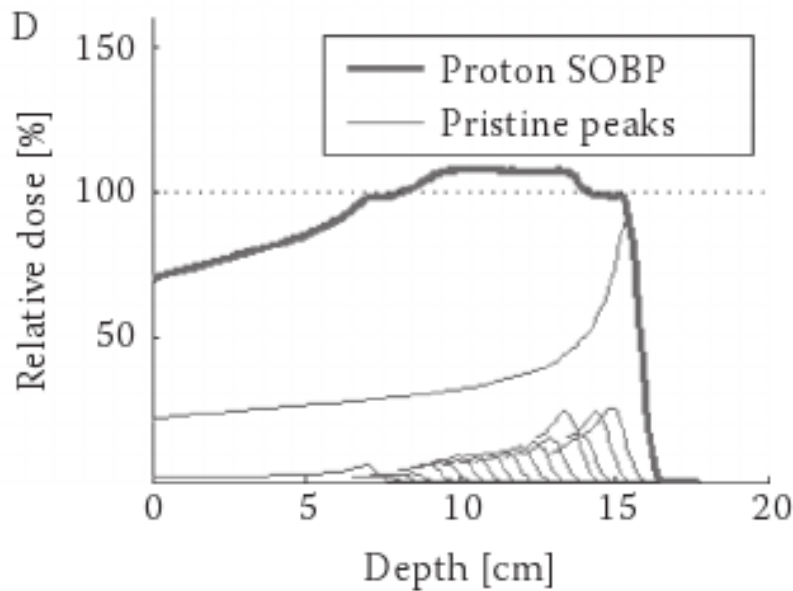
Figure 2-7: A non-uniform Spread Out Bragg Peak (SOPBP): Individually and optimally weighted pristine Bragg Peaks are superimposed in order to form a non-uniform SOBP dose plateau. Here the weighting of the Bragg Peak is increased at some depth due to the integrated boost in the middle of the SOBP (28).

2.3.2   The Passive Scattering technique

When applying the passive beam delivery technique, also called the scattered beam technique, range modulators, scattering foils, blocks, and compensators are used to modulate and shape the beam in order to tailor the dose to the shape of the target volume. The principle of the passive scattering technique is illustrated in Figure 2-8. The broadening of the beam laterally to cover the whole target homogeneously is most commonly achieved by a double-scattering system where the beam is broadened out to the required field size in two scattering steps. A uniform SOBP is formed by letting the incident proton beam sequentially penetrate absorbers of varying thickness (the passive range modulator technique) each absorber thickness applied in a dose plan calculated fraction of the total irradiation time. An additional range shifter is normally applied in order to shift the whole SOBP does plateau to the desired depth if required. This means

that the entire SOBP is positioned in a region where it covers the target volume from the most distal to the most proximal depth. For optimal beam shaping, patient- and field specific physical devices are necessary. Blocks are used to limit and adapt the lateral boundaries of each treatment field to fit the target volume, while beam absorbing compensators are designed to conform the dose the distal edge of the target volume (29).
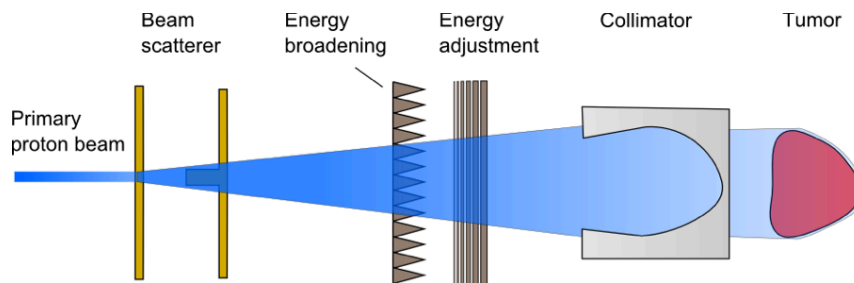
Figure 2-8: The principles of the passive scattering technique. The narrow proton beam is scattered out laterally by high Z material scatter foils, and range modulated by the use of low Z material in order to create the SOBP plateau. The compensator conforms the dose to the target distally, while patient specific blocks define the aperture. Image from (16).

2.3.3 The active scanning technique

The active scanning technique is the other main method for delivery of proton therapy. This method takes advantage of the fact that protons have an electrical charge, and therefore can be steered and deflected by magnets. By precision steering of a number of laterally deflected energy modulated proton pencil beams, a target volume can be scanned in 3 dimensions. In Figure 2-9 the principles of active scanning is illustrated. The target volume is divided into layers of equal energy (iso-energy layers), which, due to the different densities in the patient not necessarily are in the same plane. The deepest layer, which requires the highest beam energy, is scanned first, then the beam energy is reduced and the next layer is scanned and so on, until all layers have been delivered. The scanning of each layer can be done by e.g. so-called discrete spot scanning technique. In discrete spot scanning the dose is delivered to so-called spots, which are pristine Bragg peaks

characterized by its range, intensity and size (30). Compared to the passive scattering technique, the active scanning technique has several advantages. Firstly, because the dose distribution can be shaped and tailored to the target without any physical absorbers or patient specific compensators or blocks, the amount of nuclear interactions that occur in the physical devices are significantly reduced, and therefore the production of neutrons outside the patient is reduced accordingly. Moreover, the additional dose often seen proximal for the target volume when applying the passive technique, can with the active technique be avoided. Secondly, the scanning technique also facilitates great flexibility, which can be fully utilized in Intensity Modulated Proton Therapy (IMPT). The disadvantage with the active scanning technique is that the treatment plans and the active scanning treatment often are more sensitive to changes in the patients anatomy and to patient and target volume motion, compared to treatment plans with the passive scattering technique (31).
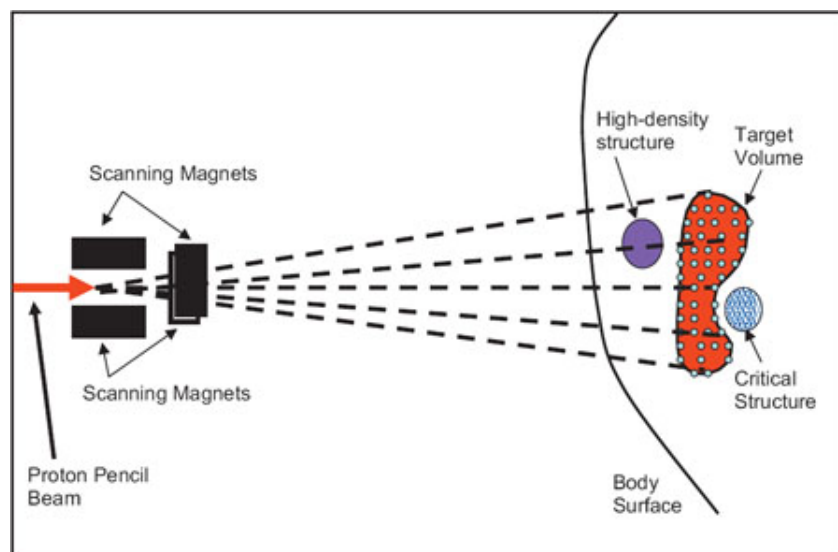
Figure 2-9: An active scanning technique: The principle of the spot scanning technique. Pencil beams applied in discrete steps deliver the dose. The proton source is interrupted after each pencil beam is delivered, the beam-steering elements are changed to deliver protons at a different position and/or energy, and the beam is turned back on until the desired number of protons has been delivered. Image from (32).

2.4   The treatment planning process for proton beams

The radiotherapy treatment planning process involves several stages, including the acquisition of the planning CT, the volume delineation in the CT images, the design of the treatment plan, and the calculation of the dose distribution and the evaluation of the treatment plan. The design of a proton treatment plan includes the choice of field arrangements, such as the number of field and the field angles, the assigning of the dose prescription and the dose fractionation, the choice of optimization methods, the use of beam modifying devices and the margin definitions. This section provides a description of these various steps, based upon the planning methodology in the Eclipse™ proton treatment planning system.

2.4.1   CT imaging, Hounsfield Units and the calibration curve

Computer Tomography (CT) is the standard imaging modality for treatment planning in proton therapy. A CT image dataset provides detailed 3D information of the patient's anatomy, as well as information about the tissue density in the scanned patient volume. In CT images the density of a specific volume of tissue is given by what is known as the Hounsfield Units (HU). The HU is a numeric representation of the mean measured x-ray attenuation in each voxel in the scanned volume. The relationship between the linear attenuation coefficient (μ) and the HU value is given by

$$HU = \frac{\mu_{tissue} - \mu_{water}}{\mu_{water}} \times 1000 \qquad\qquad \text{(Equation 2.9)}$$

Here the μ_{tissue} and μ_{water} represent the linear attenuation coefficients of the irradiated tissue and water respectively. The HU value of a tissue is however not absolute, it will be influenced by the applied x-ray energy, the reconstruction filter, the slice thickness and the presence of image artefacts like for instance the partial volume effect (9).

The planning CT images serves two purposes; firstly, it is used to define the anatomic and geometric structures that are of significance for the radiation treatment. Secondly, the CT image dataset is used to estimate the proton range in the patient used when calculating the

dose distribution. To do this, the HU values have to be converted in to relative proton stopping power using a calibration curve. The purpose of the calibration curve is to establish a correlation between the HU values of the human tissue, and the relative stopping power. To generate a calibration curve, the relative stopping power is calculated for a large number test materials of human tissue of known chemical composition, this using a simplified version of the Bethe-Bloch formula. The corresponding measured HU value from the test material is then plotted against the theoretically computed relative stopping power values. Several linear lines are fitted to the plotted data, each line extends over a limited number of HU values, as displayed in Figure 2-10. The final calibration curve is normally a combination of linear fitted curves from data containing information from attenuation in lungs, soft tissue and bone (19, 33).
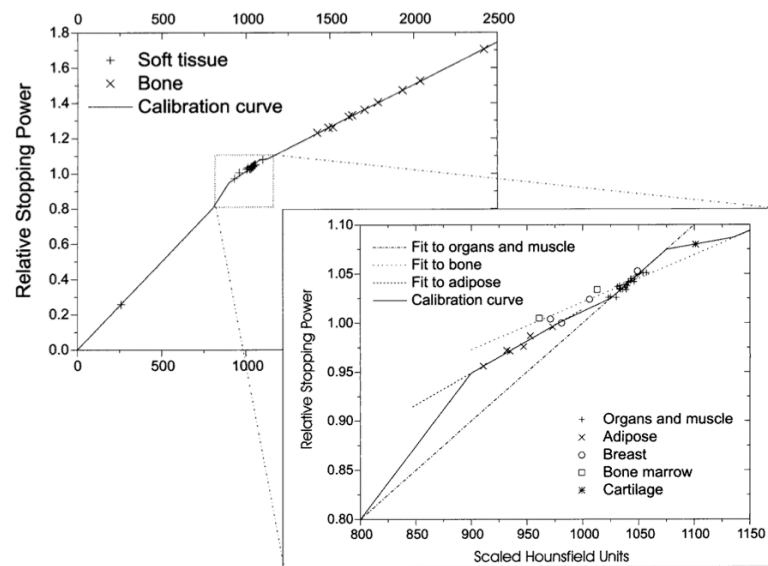
Figure 2-10: Calibration curve with the relation between Hounsfield Units and Relative Stopping Power: The calibration curves obtain by the stoichiometric method. The enlarge graph displays the soft tissue group split into five linear curves. The image behind shows the final calibration curve generated from a combination of the three linear fitted curves for lung tissue, soft tissue and bone tissue. Image from (34).

2.4.1.1 Range uncertainties associated with the CT calibration curve

The level of precision with which one can determine the stopping power in the patient is directly dependent on the accuracy of this calibration curve. The calibration curve used for the conversion of the HU values thus has to be generated for each CT scanner using the same acquisition parameters (like the x-ray energy, the reconstruction filter and field of view) as the setting applied for the planning CT image acquisition (35). Any errors in the Calibration Curve are purely systematic and will affect the proton range in each treatment fraction to the same extent and consequently have a consistent effect on the delivered dose distribution. The errors in the Calibration Curve caused by inaccuracies in the process of converting the HU value into relative stopping power associated with this methodology has been found in general to be less than ± 1% (34, 35). Calibration Curve Errors are also caused by the uncertainty in the HU values themselves. The determination of the HU values is influenced of several factors; CT image noise, the Field of View during acquisition, the presence of CT artefacts like beam hardening, metal and motion artefacts and partial volume artefact due to density heterogeneities. Noise has been found to caused an error in the HU value of ±1% while the error in the HU values for bone and soft tissue is in the order of ±1,8% and ±1,1% respectively (34). A realistic and common used value for the estimation of the total CT based from HU to Relative Stopping Power conversion uncertainty is 3,5% of water equivalent range (36).

2.4.2   Coordinate system and patient geometry.

The patient geometry in radiotherapy is described by the three basic anatomical planes and by the patient coordinate system. In the patient coordinate system the x-axis runs from shoulder to shoulder, the z-axis from feet to head and the y- axis runs from front–back. The transversal body plane, also known as the cross-section or the axial plane, divides the body into cranial and caudal regions. The coronal plane, also called the frontal plane, divides the body into dorsal and ventral regions, and sagittal plane divides the body in left and right regions.

Figure 2-11 displays the relations between the anatomical planes and the patient coordinate system on CT images. In Figure 2-11a) the CT image is displayed in the transversal view. The view is along the z-axis, the x-axis runs left -right and the y-axis dorsal - ventral. In Figure 2-11b) the CT image is displayed in the coronal view. The view is along the y-axis,

the x-axis runs left - right and the z-axis runs caudal-cranial. In Figure 2-11c) the CT image is displayed in the sagittal view. The view is along the x-axis, the y-axis runs dorsal - ventral and the z-axis runs caudal – cranial (37).
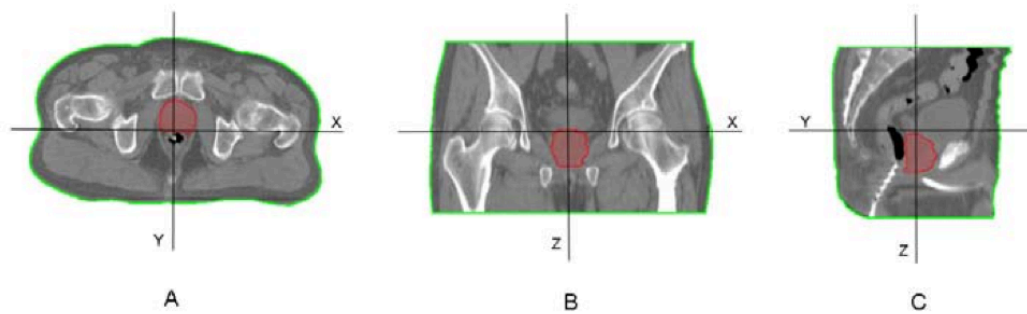
Figure 2-11: The viewing planes in the patient including coordinate axis. In A) the transversal viewing plane is displayed, in B) the coronal plane is displayed and in C) the sagittal plane is displayed. Image from (37).

2.4.3 Volume definitions

The International Commission on Radiation Units & Measurements (ICRU) has developed standards for defining anatomic and geometric volumes, as well as nomenclature for dose-volume specifications in radiation therapy (19).

Figure 2-12 provides an illustration of anatomic and geometric volumes as defined by the ICRU: The Gross Tumour Volume (GTV) is the palpable, the visible or clinical demonstrable location and extent of the tumour. The Clinical Target Volume (CTV) is the tissue volume that contains the GTV and/or subclinical disease. The CTV is the volume we want to provide the prescribed dose. The Planning Target Volume (PTV) is a geometrical volume that contains the CTV with an additional uncertainty margin. The purpose of the uncertainty margin is to ensure that the prescribed dose is delivered to the CTV despite the different treatment variations. The Target volume (TV) is a general term associated with the tumour; it can either be the GTV, CTV or the PTV. Organs at risk (OAR) are normal tissue are organs whose radiation sensitivity can influence treatment

planning and/or prescribed dose. The volume of interest (VOI) is a generic term that can be used to refer to any volume that needs to be identified. Figure 2-14 gives a schematic illustration of the volumes and margins related to the definition of the target volume.
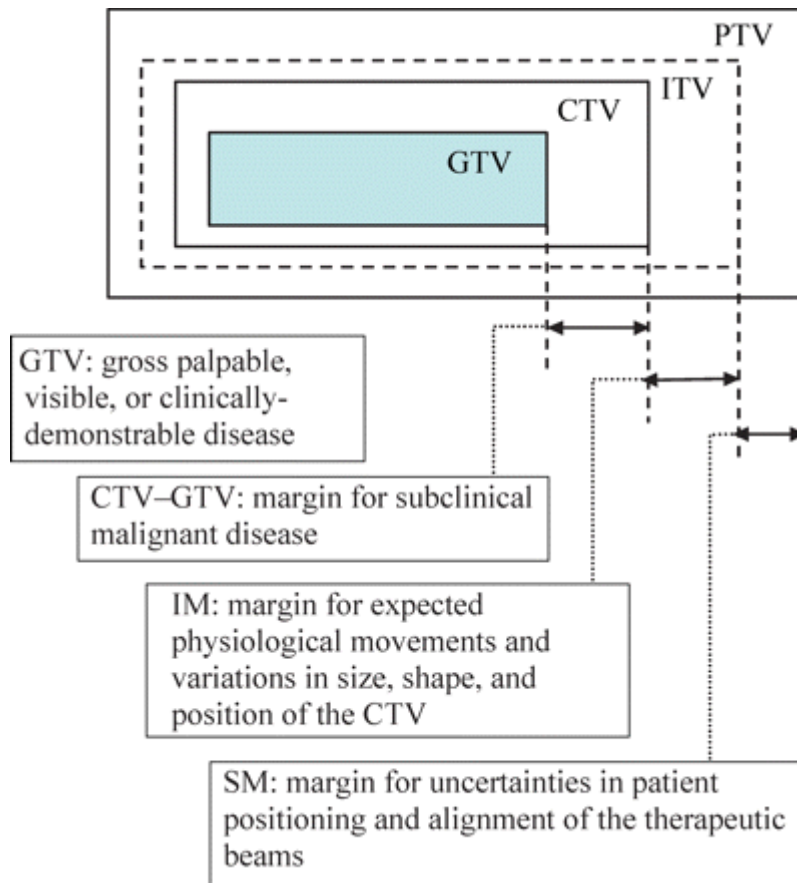
Figure 2-12: Schematic illustration of anatomic and geometric volumes, as defined by the ICRU (19).

In addition to the anatomic and geometric volumes described above, it is sometimes beneficial to define so-called Technical volumes that are needed in the planning process. These are for instance target volumes that are modified in the purpose of facilitating the optimization process. It can also be areas at the CT images that have to be assigned adjusted HU values. This could typically be in situations where CT artefacts influence the images and where the HU value would have to be changed to the average HU value of the

surrounding tissue, or in situations with the presence of external devices that are present during the CT image acquisition, but absent later, during the radiation treatment.

2.4.4 Plan-and field specific parameters applied in passive scattering technique.

In the passive scattering technique the concept of PTV is discarded and instead the field parameters are determined relative to the CTV. The managing of uncertainties is solved by building the uncertainty margins in the field- and patient specific blocks and compensators (38).

2.4.4.1 Apertures

The purpose of apertures is to shape the lateral extent of the proton beam to the target volume and shield the surrounding healthy tissue. A block is normally made of brass and it is defined in the Beams-Eye-View (BEV) for each beam direction. The aperture is defined relative to the CTV by a distance corresponding to the internal target motion and the setup uncertainty. In addition it also includes the 95-50% penumbra with, determined at the widest extent of the target (39) (s 309).

2.4.4.2 Distal and proximal uncertainty margin

The uncertainty in range due to potential errors in the calibration curve is handled by adding an extra distal and proximal margin to the CTV and thereby increases the SOBP. The distal and proximal margins are defined in order to account for a 3,5% uncertainty in the calibration curve and to account for beam range uncertainty due accelerator energy, variable scattering system thickness, compensator density amongst other (40). The distal margin, *DM,* is defined by the following equation:

$$DM_{CTV} = 0,035 \times (distal\ CTV\ depth) + 1 - 3\ mm \qquad \text{(Equation 2.10)}$$

The proximal margin, *PM*, on the CTV is calculated in the same way:

$$PM_{CTV} = 0,035 \times (proximal\ CTV\ depth) + 1 - 3\ mm \qquad \text{(Equation 2.11)}$$

2.4.4.3 The range compensator

The range compensator conforms the distal end of the dose distribution to the target volume by varying thickness of a range-shifting material of water equivalent density. The thickness of the compensator is calculated by first to determine the Water Equivalent Thickness (WeT) to the target border for each so-called beamlet, which is a single energy beam positioned at a certain part of the target volume. The thickness of the compensator is then computed in terms of WeT differences by calculating the difference between the maximum WeT and the WeT at the border of the target volume. The range compensator has to be assigned a smearing margin in order to account for possible misalignment of the tissue density due to setup errors or organ motion. This smearing is performed by assigning each pixel in the compensator matrix with the minimum value from the vicinity pixels within a region defined by a user defined smearing margin (41).

2.4.5 Plan- and field specific parameters applied in active scanning technique.

In the following some plan- and field specific key parameters required for the optimization process and the calculation of the dose distribution are described.

2.4.5.1 Lateral and axial margins

The lateral and axial margins are defined relative to the target volume in each individual field (field specific margins). These so-called field specific margins are used in the initial beam and field calculation in order to define all possible spot positions for each particular field.

The axial margin comprises a distal and a proximal margin. This means that for each field one adds a certain margin, for instance 2 mm, relative to the proximal and distal end of the target volume. During the calculation of the spot positions, the maximum and minimum energies for each field will be determined based on the depth of the proximal and distal end of the target volume in addition to the defined axial margins (37).

We have that similarly to the axial margins, a lateral margin is defined relative to the target volume for each field. Because of the discrete distance between the Bragg Peaks in the directions orthogonal to the beam direction (the spacing between the spots), there is a risk that the most superficial spots are positioned inside the target volume, which may result in problems achieving adequate dose coverage at the boundary of the target volume. By adding a lateral margin one ensures that spots also are positioned outside the target volume boundary when necessary (31, p. 341).

2.4.5.2 Beam modifying devices

The depth of the Bragg Peak in matter is energy dependent, thus superficial target volumes require low proton energies, and for a target volume near, or at the body surface, the required energy will be lower than the minimum energy the Energy Selection System can provide. Target volumes that range from a very shallow depth to a very deep depth would require both low- and high-energy protons in order to be covered by a homogeneous dose at all levels. It is however difficult to produce protons with such a low energy from accelerators, which are designed to produce stable proton beams of energies of typically 70-250 MeV. With synchrotrons there will be similar problems with producing protons with a requested energy below the energy range that the machine is designed for. Thus, the beam energy in some instances has to be degraded by introducing a pre-absorber in the beam, a so-called range shifter. The range shifter consists of a low Z material, normally water-equivalent material, this in order to minimize the beam divergence due to Multiple Scattering in the absorber material (31, p. 347).

2.4.6   Optimization and calculation of the dose distributions

2.4.6.1 Optimization methods

When applying the Single Field Optimization (SFO) technique each field is optimized independently to deliver a homogenous dose to the target volume. In a multifield treatment plan the dose distribution from each field are mutually weighted and combined by a simple addition. This technique is also referred to as Single Field Uniform Dose (SFUD) (42). No sparing of the OAR is possible with SFO beyond that achieved by a carefully selection of the field arrangements.

In the Multifield Optimization (MFO) technique all fields are optimized simultaneously and coupled together so that the target is coved with a homogenous dose when the contributions from each field are added together. Each field though, could have a heterogeneous dose distribution. The multifield optimization technique is also referred to as Intensity Modulated Proton Therapy (IMPT), and this technique allows for the sparing of the OAR during the optimization process. Several IMPT techniques exists, the most common and sophisticated is the 3D IMPT, in which all the Bragg peaks positioned throughout the target volume are individually weighted (43).

2.4.6.2 Planning objectives and objective functions

The active scanning technique uses an inverse treatment planning approach. As briefly mentioned in chapter 2.2: the inverse approach implies the use of so-called planning objectives, which defines a set of treatment goals. The planning objectives, and their priorities, are mathematically formulated as objective functions. Typically these aims at minimizing the dose difference between the calculated dose distribution, and the defined objectives for the target volumes, OARs and other VOIs (organs at interest, normal tissue, technical volumes). It is a stepwise iterative process, which involves the spot weights being iteratively modified in order to achieve an optimal set of beam intensity distributions, so-called fluence maps.

The commonly used objective functions aims at either minimizing the volume of a VOI receiving a dose higher than a specified dose value, so-called upper objectives, or minimizing the volume of a VOI receiving a dose less than a specified, so-called lower objective. The upper objectives is typically expressed as; no more than $V_{\%}$ can receive dose greater than D. Similarly the lower objective expresses that at least $V_{\%}$ of the volume should receive dose greater than D. Upper and lower objectives are typically defined for the target volumes, while only upper objectives are defined for the organs at risk. Planning objectives for target volumes and organs at risk may be in direct conflict in a clinical situation, thus a weighted priority between the objective functions relative to their importance is required (28, 41).

2.4.6.3 The dose calculation process

The dose calculation process is a step-by-step process and in general, in a situation where one is applying the active treatment technique with spot scanning, it implies the steps in a process as the following:

1. The first step includes the calculation of the initial spot list. This calculation is amongst other based on the defined target volume including the lateral and axial margins (see 2.4.4.1), the defined spacing between the energy layers, the defined spacing between the peaks and the size of the pencil beam.
2. The second step involves the optimizing of the spot weights by the use of the defined objective functions.
3. The final calculation includes firstly the calculation of the dose in each energy layer and secondly the summation of the dose contributions from all the pencil beams (beamlets) within each layer. In the final step of the calculation process doses from all layers are superimposed in order to calculate the overall 3D dose distribution (28, 41).

2.4.7 Plan evaluation

The evaluation of a treatment plan is based on analyzing and interpreting the calculated dose distribution both qualitatively and quantitatively. The qualitatively evaluation is done by displaying the dose distribution on the planning CT images and analyze this, slice by slice, and in each of the anatomical planes. The quantitatively evaluation is done by interpreting Dose Volume Histograms and by the calculation of quantitative indices which quantifies the homogeneity and conformity of the treatment plan.

2.4.7.1 Visualization of the dose distribution

Dose distributions are commonly displayed on the CT images by isodose curves or by so called colour wash as illustrated in Figure 2-13a) and Figure 2-13b). Isodose lines are a set of closed contours that are passing through voxels or points of equal dose. All voxels enclosed by the contour have doses equal to, or above the specific dose level defined by the contour. They can be expressed either as absolute dose levels, of as percentage of the prescribed dose. They are usually defined in regular intervals as shown in Figure 2-13a)).

Colourwash displays dose distribution in a continuous colour map (Figure 2-13b)). The dose levels are scaled by a colour bar. The range of dose levels is user defined; one can show all the dose values, or limit the visualization. Doses that exceed a range limit are showed in some chosen colour, dose below the range is not visualized. As for the isodose curves, the colourwash can be displayed in both absolute and relative units of the prescribed dose (37).
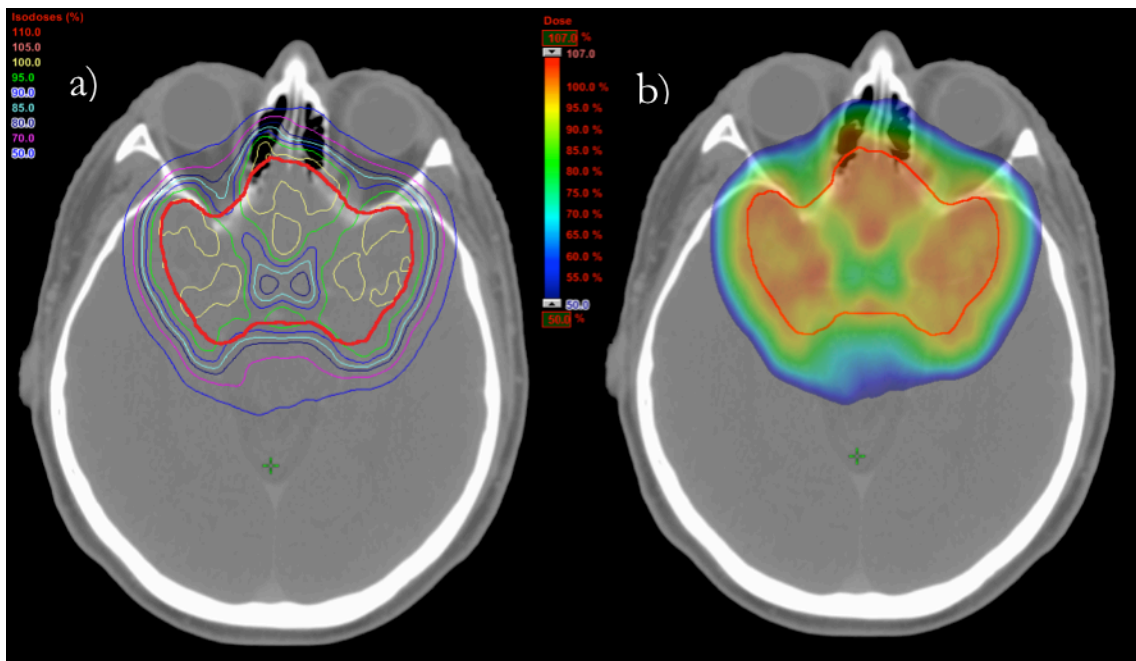
Figure 2-13: In image 2-13a) the dose distribution is displayed by isodose lines, ranging from the 50% level to the 110 % level. Each dose level is assigned a colour as displayed to the left in the image. In image 2-13b) the dose distribution is displayed by colour wash, from the 50% dose level to the 107% dose level. The dose levels are displayed by the colour bar scale to the left in the image. Doses below the defined colour range are not visualized.

2.4.7.2 Dose and Dose-Volume Histogram related definitions

A Dose Volume Histogram (DVH) graphically summarizes the dose distribution within a volume of interest. Dose-volume specifications can be directly read from the DVH and is, together with visualization of the dose distribution, an important tool in evaluating treatment plans. Figure 2-14 gives an overview over different dose-volume specifications that can be read out of the DHV.
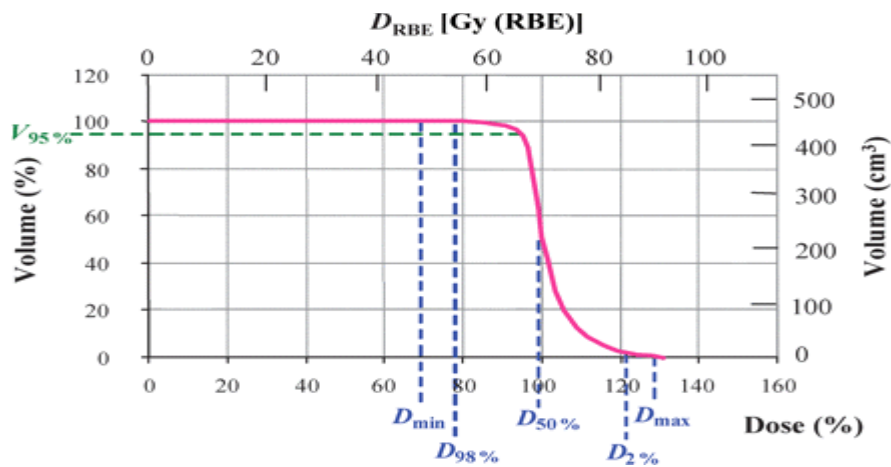
Figure 2-14: Dose Volume Histogram (DVH). Both dose and volumes can be in relative or absolute units. The structure volume is displayed on the y-axis and dose on the x-axis. The figure is illustrating typical dose-volume relations that are read out of the DVH (19).

The D_V is the least dose received by a volume **V**, of a specified VOI. To exemplify; $D_{80\%} = 70$ Gy(RBE) means that at least 70 Gy(RBE) is delivered to 80 % of the volume. For both cases the volume **V** and the dose **D** can be reported in absolute or relative units.

The quantity V_D is the largest volume of a specified VOI that receives at least a specified dose. To clarify; the expression $V_{34,3Gy} = 95\%$ would mean that 95% of the volume receives at least 34,2 Gy(RBE).

The $D_{min} = D_{100\%}$ and is the minimum dose delivered to a voxel within a VOI, usually the target volume. The $D_{max} = D_{0\%}$ and is the maximum dose delivered to a voxel within a VOI, usually the target volume.

The $D_{98\%}$ is also denoted as the $D_{near\text{-}minimum}$ and quantifies the dose level received by at least 98% of a VOI, usually the target volume. Consequently 2% of the volume receives doses below this level.

37

Similarly the $\mathbf{D}_{2\%}$ also denoted as the $\mathbf{D}_{\text{near-maximum}}$, quantifies the least dose received by 2% of target volume and accordingly it will be 2% of the VOI, which receives dose above this level. The $\mathbf{D}_{98\%}$ and $\mathbf{D}_{2\%}$ value is not as sensitive as the $\mathbf{D}_{\text{min}}$ and $\mathbf{D}_{\text{max}}$ with the respect to the dose calculation matrix resolution, and also with respect to variability in contouring, patient anatomy, which a very significant factor, and also to patient movement, and is therefore taken as a more applicable and clinical relevant parameter.

The $\mathbf{D}_{\text{mean}}$ is the mean or average dose delivered to a VOI. The $\mathbf{D}_{50\%}$ is termed the median dose delivered to a VOI. The value of $\mathbf{D}_{\text{mean}}$ will for a target volume normally be close to the median dose as opposed to the situation for the mean dose to an OAR (19) .

2.4.7.3 Indices used to describe and evaluate treatment plans

To further describe dose distribution and the quality of a treatment plan, a number of indices are often used.

The **Conformity Index (CI)** is used to quantify how well the prescribed dose is conformed to the CTV or PTV. The CI is defined as the ratio of the treated volume to the PTV or CTV:

$$CI = \frac{TV_{RI}}{TV} \qquad\qquad \text{(Equation 2.11)}$$

In this equation, TV_{RI} is the target volume covered by the reference isodose, and TV is the target volume (44). The reference isodose is 95% of prescribed dose. The index ranges from 0 (the entire target is situated outside the prescription dose or reference isodose) to 1 (all of the target volume is irradiated to the prescription dose or reference isodose). This index does not take into account the volume of adjacent healthy tissue.

The **Conformity Number (CN)** takes into account both the irradiated target volume and healthy tissue. The CN is defined as

$$CN = \frac{TV_{RI}}{TV} \times \frac{TV_{RI}}{V_{RI}} \qquad\qquad \text{(Equation 2.12)}$$

where TV_{RI} is the target volume covered by the reference isodose, TV is the target volume and V_{RI} is the total volume of the reference isodose (44). The reference isodose is 95% of prescribed dose. A CN of 1 is ideal.

The Homogeneity Index (HI) is used to quantify dosimetric homogeneity within the CTV or PTV. The HI is defined as

$$HI = \frac{(D_{2\%} - D_{98\%})}{D_{50\%}} \qquad \text{(Equation 2.13)}$$

where $D_{2\%}$ is the dose delivered to the 2% of the TV that receives the highest dose, and $D_{98\%}$ is minimum dose received by 98 % of the TV, $D_{50\%}$ is the median dose to the TV (45).

3 STUDY DESIGN

The treatment plans and dose calculations in this study were all generated in the Eclipse™ treatment planning system (Varian Medical Systems, Palo Alto, CA, USA) for proton therapy, including the dose calculations after the simulation of tissue density changes, geometric errors and range estimation errors. The Brilliance Big Bore CT scanner (Phillips Healthcare, Best, Netherlands) was used in acquisition of the CT images used for creating the craniospinal treatment plans.

3.1 The water phantom study

3.1.1 Design of the homogeneous and heterogeneous phantoms

The first part of this study included the construction of cubic water phantoms in the treatment planning system. Three different phantoms were manually designed in the treatment planning system, all with the outer dimensions of $30 \times 30 \times 30$ cm^3. The treatment planning software enables the user to assign a HU value in any defined volume inside of the dose calculating area; the HU value was thus set to 0 in order to set the density to water in all the phantoms. Figure 3-1 displays the phantoms.

Phantom A$_{water}$ consisted of the outer $30 \times 30 \times 30$ cm^3 water volume surrounding a cube shaped target volume with the dimension $10 \times 10 \times 10$ cm^3. The target volume was placed at the centre of the phantom and consisted of water (assigned a HU value of 0). Thus phantom A$_{water}$ was a completely homogenous water phantom.

Phantom B$_{bone}$ consisted of the outer $30 \times 30 \times 30$ cm^3 water volume surrounding a cube shaped target volume with the dimension $10 \times 10 \times 10$ cm^3 and with an additional cubic inner structure of $5 \times 5 \times 5$ cm^3. The inner structure of the target volume consisted of bone (assigned a HU value 1000), the rest of the target volume consisted of water (assigned a HU value of 0). Thus the target volume in Phantom B$_{bone}$ was heterogeneous consisting of a composition of bone and water.

Phantom C$_{air}$ consisted of the outer $30 \times 30 \times 30$ cm^3 water volume with a cube shaped target volume with the dimension $10 \times 10 \times 10$ cm^3 and with an additional cubic inner structure of $5 \times 5 \times 5$ cm^3. The inner structure of the target volume consisted of air (assigned a HU value -1000), the rest of the target volume consisted of water (assigned a

HU value of 0). Thus the target volume in Phantom C$_{air}$ was heterogeneous consisting of a composition of air and water.
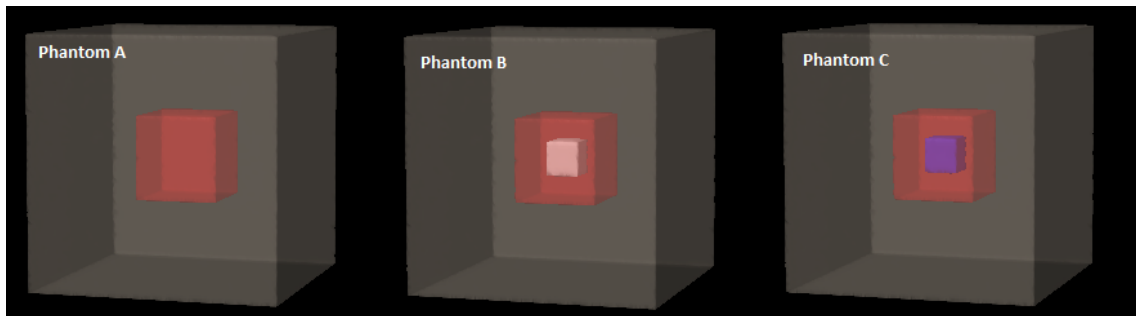
Figure 3-1: The phantoms: The red cubes at the centre of the water phantoms illustrate the target volumes. Phantom A$_{water}$: The target volume is completely homogeneous consisting of water. Phantom B$_{bone}$: the target volume is heterogeneous consisting of bone (white inner structure) and water. Phantom C$_{air}$: the target volume is heterogeneous consisting of air (blue inner structure) and water. All target volumes are placed at the centre of the water phantoms.

3.1.2   The water phantom reference plans

The water phantom reference plans were created in order to represent the "ideal" situation with no errors applied. The proton dose distributions in the water phantoms were generated applying a one-field plan on each of the phantoms; A$_{water}$, B$_{bone}$ and C$_{air}$. A lateral field specific margin of 1 cm relative to the target volume was applied. The proximal and distal field specific margins were set to 0. The isocenter was positioned at the centre of the target volume. The dose distributions were generated using the active scanning technique, with a single field optimization (SFO) option. The total dose of 10 Gy was prescribed.

The dose-volume objectives used for optimization were:

1. Lower objective: 100% of the target volume should receive at least 9,8 Gy.
2. Upper objective: 0 % of the target volume should receive more than 10,2 Gy.
3. The maximum number of iteration was set to 1000.

For all the plans, the optimizing process completed prior to reaching the maximum number of iterations. After optimizing the plans according to the dose-volume objectives

described above, the plans were calculated and normalized so that the 95% dose covered 100% of the target volume. The total dose distributions for the reference plans, which were used as reference for the error simulations, are displayed with isodose lines in the top panel of Figure 3-2, and with the 95% -107% dose distribution displayed in colour wash in the bottom panels of Figure 3-2. The corresponding dose statistics are listed in Table 3-I.
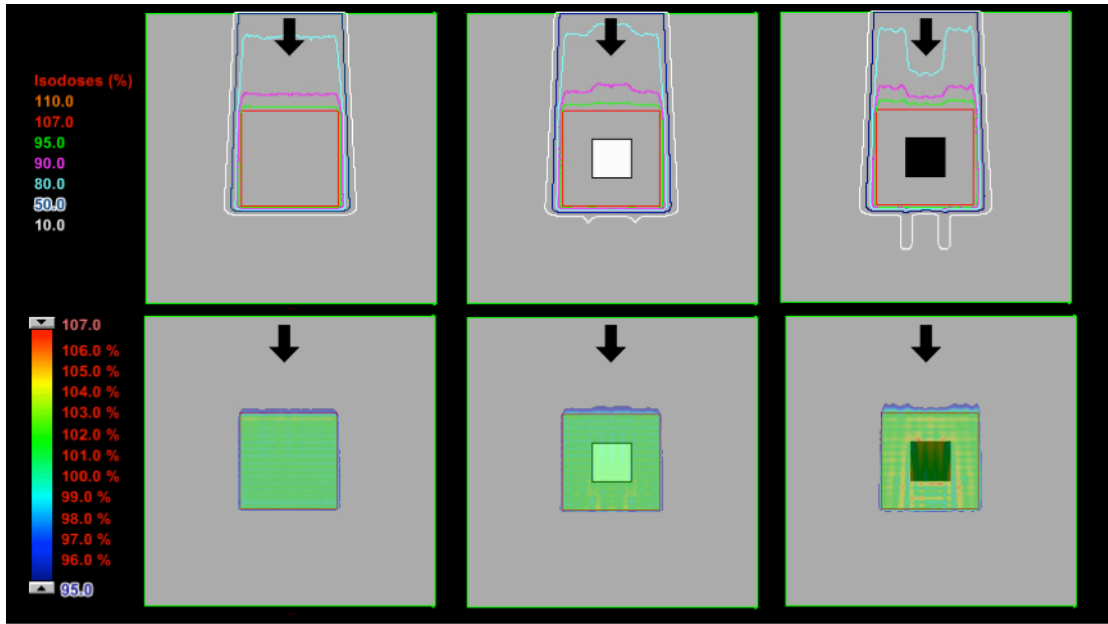
Figure 3-2: The total dose distributions are displayed by isodose lines in the top panel for phantom A_{water}, B_{bone} and C_{air}. The corresponding 95%-107% dose distribution is displayed in colour wash in the bottom panels. Phantom A_{water} is showed on the left, phantom B_{bone} in the middle and phantom C_{air} on the right. The black arrow in the images indicates the beam direction.

Table 3-I: Dose statistics, displayed in relative values (%), for the reference plans on phantom A_{water}, B_{bone} and C_{air}.

Parameter	D_{min}	D_{max}	$V_{95\%}$	D_{mean}	$D_{98\%}$	$D_{2\%}$
A_{water}	95,0	103,5	100,0	101,1	102,6	98,9
B_{bone}	95,0	104,4	100,0	101,3	102,4	99,7
C_{air}	95,0	108,6	100,0	102,3	104,5	100,2

Abbreviations: $D_{min} = D_{100\%}$: minimum dose delivered to the target volume. $D_{max}=D_{0\%}$: maximum dose delivered to the target volume. $V_{95\%}$: Volume receiving at least 95% of prescribed dose. D_{mean}: mean/average dose delivered to the target volume. $D_{98\%} = D_{near-minimum}$: least dose received by 98% of the target volume. $D_{2\%}= D_{near-maximum}$: least dose received by 2% of the target volume.

3.1.3 Simulation of changes in tissue composition in the beam path

The simulation of a change in the tissue density in the beam path was performed in the treatment planning system in the following way:

- Rectangular volumes with varying thicknesses of 0,5 cm, 1,0 cm, 1,5 cm, 2,0 cm and 2,5 cm were designed.
- The rectangular volumes were assigned a HU value of 1000, representing bone, and a HU value of -1000, representing air.
- The air and bone volumes were sequentially inserted in the beam path 1 cm and 5 cm in front of the target volume, covering the entire target volume area in the beam's eye view (Figure 3-3).
- So-called verification plans based on the reference plan designed in phantom A_{water} were then recalculated with water being sequentially replaced by the air and bone volumes.

By using verification plans for this purpose, the recalculation of the dose distribution could be performed using the initial spot distribution from the reference plan (the spot distribution with no air or bone volumes). By using this procedure instead of performing a new recalculation of the dose distribution, the effects of the density changes could be obtained and their consequences manifested in the recalculated so-called error dose distributions.

The effect of the density changes on the proton range (ΔR), the distal dose fall-off, as well as the D_{min} and $V_{95\%}$ to the target volume was investigated by analysing and comparing the depth dose profiles and the cumulative DVHs from the reference plans and the recalculated verification plans. To represent the proton range, the position in depth of the distal 90% dose level on the central beam axis dose profile (d90%), was chosen. The distal dose fall-off was defined as the distance between the distal positions in depth of the 80% and 20% dose levels (d80%-d20%) as illustrated in Figure 3-4. The definitions of the parameters are based on the definitions given by Gall et al and cited in (19).
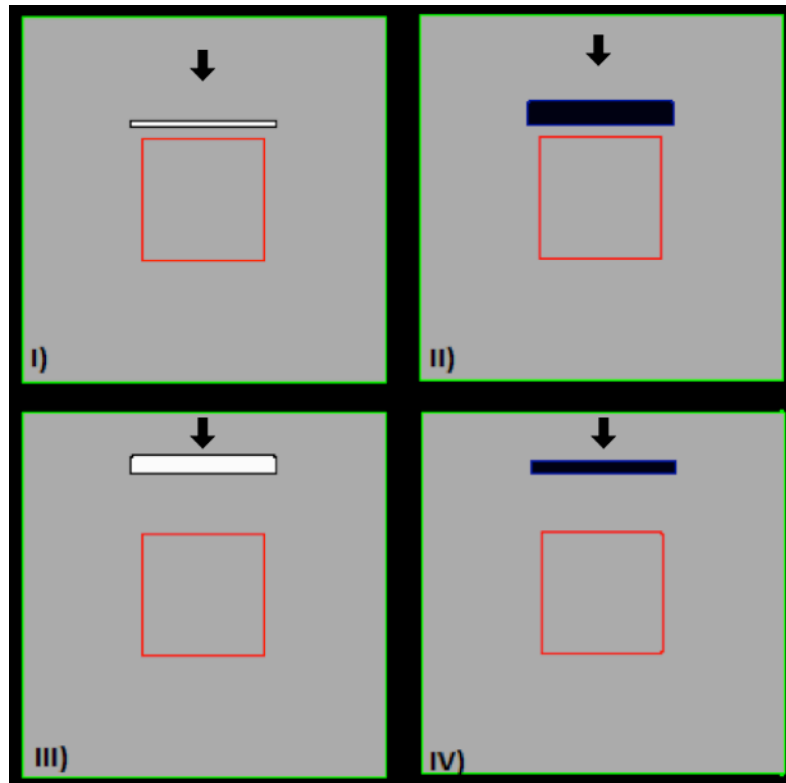
Figure 3-3: Examples showing the air and bone volumes with different thicknesses and their positions relative to the target volume (drawn in solid red line). The figure is in transversal view and shows the 0,5 cm thick bone volume (I) and the 2,0 cm thick air volume (II) placed 1 cm in front of the target volume, further the 1,5 cm thick bone volume (III) and the 1,0 cm air thick volume (IV) positioned 5 cm in front of the target volume. The black arrow indicates the beam direction.
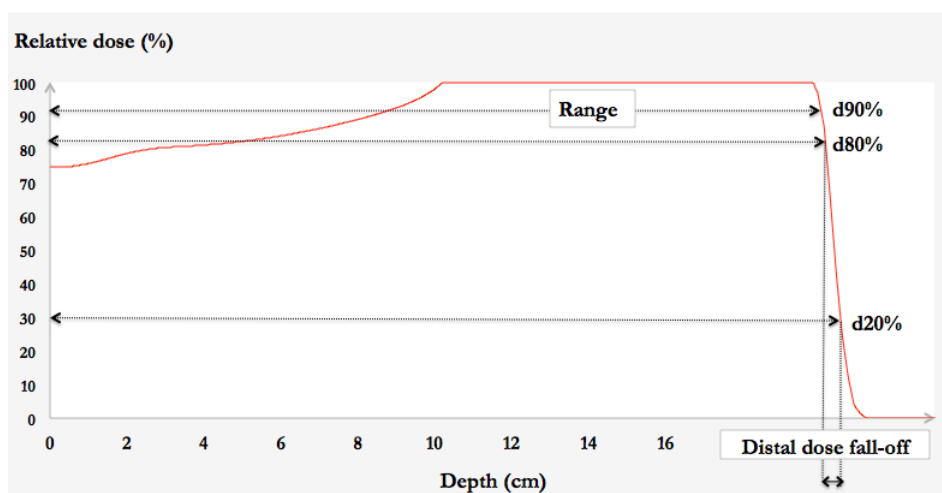
Figure 3-4: The definitions of the range (d90%) and the distal dose fall-off (d80%-d20%). The range is defined as the depth of the distal 90% dose level on the central axis dose profile. The distal dose fall-off as the distance between the distal depths of the 80% and 20% dose levels (d80%-d20%).

3.1.4   Simulation of geometric errors

The simulation of geometric errors was performed in the treatment planning system in the following way:

- Verification plans, based on the reference plans in phantom A_{water}, B_{bone} and C_{air}, were created and used for systematically shifting of the isocenter in one direction at the time.
- The magnitude of the isocenter shifts were of ±5 mm and the shifts were performed along the x-, y- and z –axis, as illustrated in Figure 3-5.
- The verification plans from phantom A_{water}, B_{bone} and C_{air} were then recalculated, now with the target volume misaligned relative to the beam due to the isocenter shifts. The recalculation was performed using the initial spot distribution (the spot distribution with no isocenter shifts) from the reference plans.

Figure 3-5 illustrates the shift directions relative to the direction of the proton beam. As the figure illustrates; shifts in the lateral direction are along the x-axis, shifts in the longitudinal direction are along the z-axis and shifts in the vertical direction are along the y-axis, this is in the beam direction. The lateral and longitudinal isocenter shifts were perpendicular to the beam axis (marked with the yellow arrow in the figure), while the vertical isocenter shifts were parallel to the beam axis.

The procedure described above resulted in 6 recalculated dose distributions. The variables investigated were the D_{min}, D_{max}, $V_{95\%}$ and the HI. The resulting dose distributions and dose profiles were also evaluated.
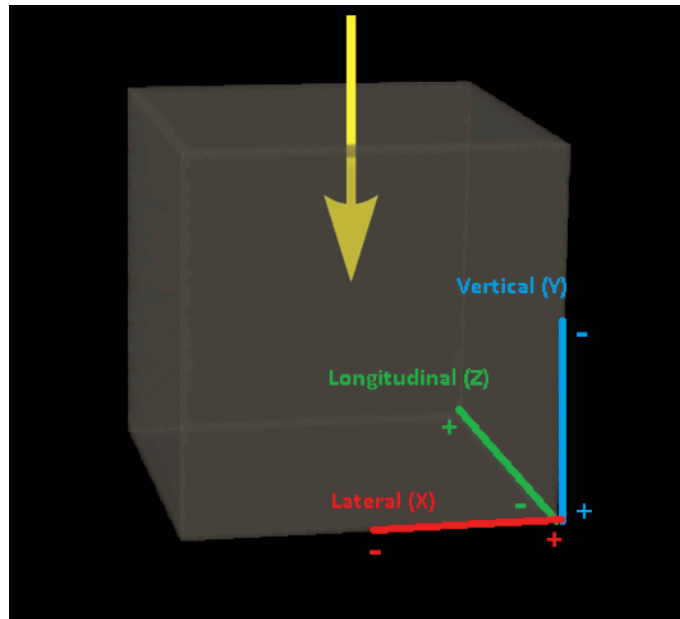
Figure 3-5: The coordinate system and the axis definitions: The figure displays the relations between the 3 axes in the coordinate system used in this study and the proton beam direction. The beam direction, which entered the phantom from above as indicated by the yellow arrow in the figure, was similar in all plans.

3.2   Robustness analysis of craniospinal treatment plans

The treatment planning method used in creating the craniospinal treatment plans, was based on the guidelines for conventional CS planning at Haukeland University Hospital (HUH) (46), the reference manual from the treatment planning system (37, 41) and published papers by (7, 47-49).

3.2.1   The CT image datasets for treatment planning

Anonymous CT image dataset from 6 paediatric patients who earlier had been treated at HUH were included in this study. The image datasets consisted of a set of predefined structures, as well as the dose distributions belonging to the treatment plans that were delivered in the already executed radiation treatment of the patients. The patients had all been immobilized in prone position in a vacuumed cushion filled with tiny polystyrene beads fix (Vac-Lock™ from Civco Medical Solutions, Orange City, USA) and a thermoplastic mask (Posicast® from Civco Medical Solutions, Orange City, USA) The patient positioning and fixation was according to HUH procedures for conventional

craniospinal treatments. The patient volume from top of the head to lower sacrum was included in the CT scans, which were performed with a slice thickness of 3 mm.

3.2.2 The definition of target volumes and organs at risk

In the radiotherapy treatment of CNS tumours where there is risk of seeding into to the cerebrospinal fluid with subsequent metastasizing, the primary target volume consists of the whole brain and the spinalcanal, through the cauda equina to the junction area between the second and third sacral vertebrae (S2/S3). In the predefined structure sets, no CTV had been delineated. However, the brain and the spinal canal were defined, these volumes were reviewed, and modified, if necessary, according to the criteria mentioned above, after which the CTV was created by a Boolean summation operation of the two volumes. The CTV was then extended to also include the entire corpus vertebrae. This is a common approach in proton craniospinal treatments for paediatric patients in order to avoid that the steep dose gradients result in non-uniform irradiation of the corpus vertebra, with the possibility of asymmetric growth of the skeleton as a consequence (50).

An asymmetric uncertainty margin was added to the CTV in order to create the PTV. The CTV was expanded with 4 mm in all directions in the brain area as displayed in Figure 3-6a) and 5 mm in the lateral and proximal direction in the area of the spinal canal. No margin was added distally, thus the CTV and the PTV coincide along the edge of the corpus vertebrae as displayed in Figure 3-6b) and Figure 3-6c). The choice of using no margins around the vertebral area is based on the fact the primary target volumes in the treatment regimen are the brain and the spinal canal. The inclusion of the corpus vertebra in the CTV volume only serves the purpose of avoiding radiation-induced growth disorders, but this with the consequence of an increased irradiated volume. It was therefore desirable to keep the volume of CTV as small as possible. The idea being, that a target miss in this area could only, in the worst-case, lead to asymmetric growth, and not affect the clinical outcome (i.e. the prognosis for survival).

For optimization purposes the PTV was divided into a cranial PTV (PTV_{cran}), which included the brain and most of the cervical spine, and a spinal PTV (PTV_{spin}), which included the whole spinal canal. The PTV_{cran} and the PTV_{spin} were overlapping to avoid an edge-to-edge junction between the volumes (Figure 3-6d)). The choice of dividing the PTV

into two separate volumes was due to the different sizes of the PTV in the brain and spinal area. The idea was that it would ease the optimization process when the PTV was divided into two different volumes, volumes that in turn were allocated similar dose-volume objectives (47).

A Normal Tissue volume was also defined. The intention of this volume was, by assigning it with upper dose-volume objectives during the optimization process, to reduce the dose to the surrounding healthy tissue. The Normal Tissue enclosed the PTV by 3 cm and it was outwardly constrained by the body surface. An inner margin between the Normal Tissue and the PTV of 3 mm was applied; this to avoid a conflict between the dose volume objectives assigned the PTV and the Normal Tissue during the optimization process.

The organs at risk delineated in this study were the lenses, the eyes, the thyroid, the heart, the lungs and the kidneys. Table 3-II gives an overview over the individual volume sizes (in units of cm^3) of treatment planning volumes for all the 6 patients. Descriptive statistics is included in the table with the values for the mean, standard deviations, median, maximum and minimum.
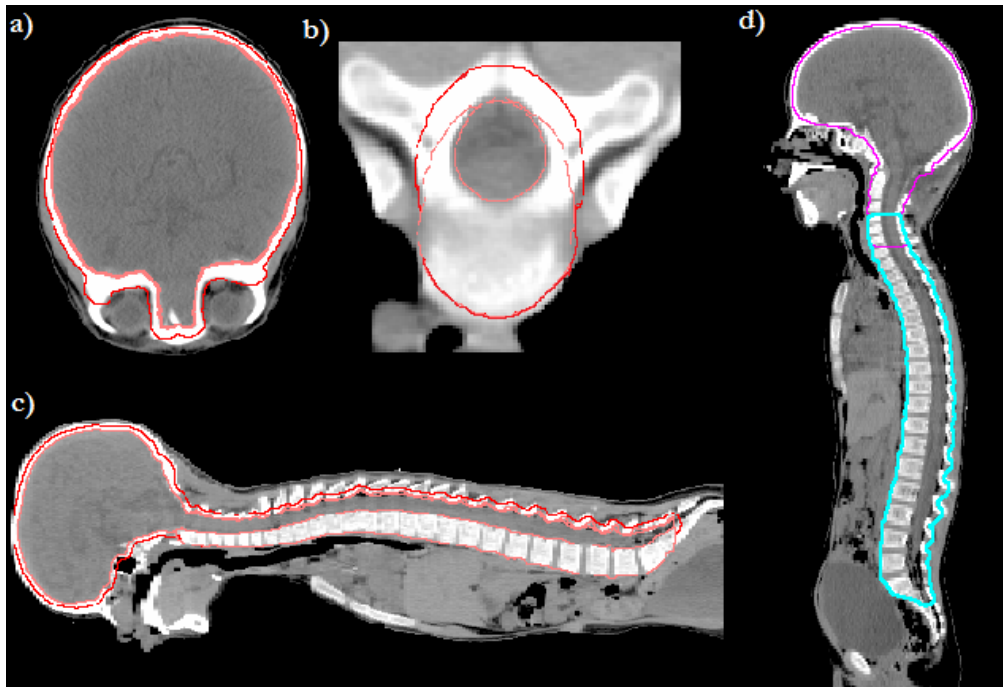
Figure 3-6: The defined target volumes in the craniospinal treatment plans. The CTV and PTV are shown in a) in the cranial area and in b) in the spinal area in in transversal plane, with the similar volumes showed in c) in the sagittal plane. In d) the PTV_{cran} is showed in magenta, while the PTV_{spin} is showed in cyan.

Table 3-II: The treatment planning volumes defined in craniospinal treatment plans (in units of cm³) for patient I-VI. The descriptive dose statistics is also displayed including the mean, the standard deviation, the median, the minimum and the maximum values.

Treatment planning volumes (cm³)											
Patient	PTV	CTV	Heart	Left lung	Right lung	Left kidney	Right kidney	Left eye	Right eye	Brain	Spinal canal	Thyriod
I	2308,0	1912	246,4	550,5	653,8	99,0	101,3	10,6	10,8	1440,1	114,1	3,3
II	2387,0	1975	204,1	417,2	500,5	81,3	91,0	7,0	11,2	1587,2	96,4	5,3
III	2102,0	1756	180,2	433,7	523,5	71,6	60,1	8,4	6,9	1379,7	71,3	2,7
IV	1996,0	1672	222,8	537,0	626,5	70,4	63,1	7,7	7,6	1344,8	76,0	3,8
V	2114,0	1849	167,4	235,7	253,1	47,6	49,0	7,6	8,4	1590,0	64,5	2,5
VI	2015,0	1670	180,1	224,9	333,0	68,5	64,5	7,8	7,8	1326,9	105,1	1,6
Mean	2153,7	1805,7	200,2	399,8	481,7	73,1	71,5	8,2	8,8	1444,8	87,9	3,2
SD	159,1	127,0	30,1	141,8	159,4	16,8	20,1	1,3	1,8	117,9	20,1	1,3
Median	2108,0	1802,5	192,2	425,5	512,0	71,0	63,8	7,8	8,1	1409,9	86,2	3,0
Min	1996,0	1670,0	167,4	224,9	253,1	47,6	49,0	7,0	6,9	1326,9	64,5	1,6
Max	2387,0	1975,0	246,4	550,5	653,8	99,0	101,3	10,6	11,2	1590,0	114,1	5,3

Abbreviations: SD= standard deviation, Min= minimum, Max=maximum.

3.2.3 The design of the treatment fields in the craniospinal treatment plans

The treatment plans were made under the assumption that the treatment could be performed with a rotating gantry and hence with the possibility to design treatment plans with multiple beam angles. All the plans had similar beam arrangement. Most of the spinal canal was covered by 2 posterior fields, both with beam angles of 0° (upper and lower spinal fields). The brain and the cranial part of the spinal canal were covered by 2 lateral oblique fields, which were angled 15° from the horizontal axis, i.e. with the beam angles of 75° and 285° (cranial fields). The choice of using angular cranial fields was based on the result from the study of Cochran et al, which showed considerable sparing of the doses to the lens by angling the fields 15°-20° to the posterior (48). The isocenter in each field were placed at the same lateral and vertical level, requiring only longitudinal shifts between the fields. The distance between each isocenter was 15- 20 cm causing an overlap between each field in order to achieve treatment plans less sensitive to setup errors in the junction area (47).

Field specific margins were added in all fields. The lateral margin was 1 cm for all fields. For the cranial fields, no proximal margin was added. The distal margin was set to 0,3 cm relative to the PTV_{cran}. For the spinal fields, the proximal margin was set to 0,1 cm and the distal margin to 0,2 cm, both relative to the PTV_{spin}. The margin sizes were determined based on the proximal and distal water equivalent distance (WED), as measured on the CT images at the isocenter level. The distal margin were calculated by:

$$DM = D_{WED} \times 3,5\% \qquad \text{(Equation 3.1)}$$

Here the *DM* is the distal margin and the D_{WED} is the water equivalent range to the distal part of the PTV. Similarly the proximal margin were calculated by:

$$PM = P_{WED} \times 3,5\% \qquad \text{(Equation 3.2)}$$

Here the *PM* is the proximal margin and the P_{WED} is the water equivalent range to the proximal part of the PTV.

The available beam energies in the treatment planning system ranged from 70 MeV to 250 MeV. Because the target volumes here were close to the body surface, energies less than 70 MeV was required for spots to be delivered at a shallow enough depth to obtain proximal

target coverage. A range shifter of 57 mm thickness and consisting of water equivalent material was applied in order to adjust the overall proton range and by this to ensure the proximal target coverage. Table 3-III lists the beam specific parameters.

Table 3-III: The beam specific properties defined by the user during the planning process of the craniospinal treatment plans.

Field number	Gantry angle	Lateral margin	Proximal margin	Distal margin	Target	Range shifter
1	75°	1,0 cm	0,0 cm	0,3 cm	PTV_{cran}	Yes
2	285°	1,0 cm	0,0 cm	0,3 cm	PTV_{cran}	Yes
3	180°	1,0 cm	0,1 cm	0,2 cm	PTV_{spin}	Yes
4	180°	1,0 cm	0,1 cm	0,2 cm	PTV_{spin}	Yes

3.2.4 Optimizing and calculating the treatment plans

The prescribed dose was 1.8 Gy (RBE) in 20 fractions adding up to a total dose of 36 Gy (RBE). The plans were optimized using the Multifield Optimization technique. The plans were designed using upper and lower dose-volume objectives for the PTV_{cran} and PTV_{spin}, as well as upper objectives for the OAR. In Table 3-IV the dose-volume objectives for all volumes are listed, the listed objectives were used as a starting point for the optimization process, thus during the optimizing process the objectives were modified more ambitious when possible and less ambitious if necessary. The modifications were performed by changing the priority or the dose volume objectives for the OAR without compromising the PTV objectives, or by changing the priority for the upper or lower dose-volume objectives for the PTVs in order to meet the dose constraints.

The scanning spot spacing and the spacing between the energy layers were defined to be 0,5 cm respectively, and the number of iterations was set to 2000. The optimizing process

continued until the maximum number of iterations was reached. The treatment plans were calculated with a proton pencil beam algorithm and the dose in each plan was normalized to the median: a 100% of the prescribed dose to be given to 50% of the PTV.

Table 3-IV: The dose volume objectives used as starting point in the optimizing process. The PTV is divided into two separate volumes (PTV$_{spin}$ and PTV$_{cran}$), each assigned identical dose volume objectives.

Organ	Limit	Volume [%]	Total Dose [Gy]	Priority
PTV$_{spin}$	Upper	0,0	36,5	120
	Lower	100,0	35,5	120
PTV$_{cran}$	Upper	0,0	36,5	120
	Lower	100,0	35,5	120
Eyes	Upper	2,0	35,5	50
Heart	Upper	0,0	12,5	50
	Upper	5,0	5,0	50
Kidney	Upper	2,0	20,0	50
	Upper	8,0	10,0	50
Lens	Upper	0,0	5,0	50
Lung	Upper	3,5	20,0	50
	Upper	12,0	10,0	50
Normal Tissue	Upper	0,0	36,0	50
	Upper	15,0	30,0	50
	Upper	40,00	20,0	50
	Upper	60,00	6,0	50

3.2.5   Evaluation of the craniospinal treatment plans

The treatment plans were evaluated both qualitatively and in terms of quantitative criteria based on common recommendations for radiation therapy (45, 51). In a clinical situation, the evaluation of a treatment plans is sometimes a trade-off between the goal of adequate

target coverage and the OAR dose constraints. In this study the main goal was to achieve sufficient target coverage, no compromises was made with respect to the target coverage.

The plans were evaluated qualitatively by visually analysing the dose distribution. The plans were evaluated slice by slice, with respect to both the total dose distribution and the 95%-107% dose distribution. The 95% dose should cover the PTV with no large hotspots (doses >107% of prescribed dose) in normal organs or large cold spots in the target volume (doses < 95% of prescribed dose). Quantitatively the plans were evaluated in terms of:

- PTV $D_{98\%} \geq$ 95% of prescribed dose,
- PTV $D_{2\%} \leq$ 107% of prescribed dose,
- PTV $V_{95\%} =$ 100%. The 95% corresponds to 34,2 Gy (RBE).

The HI, the CI and the CN were also calculated for the PTV. In addition the PTV D_{max} and the PTV D_{min} were too evaluated.

3.2.6 Simulation of range- and geometric errors in craniospinal treatment plans

Two different scenarios were studied. The first situation to be investigated was the effect of errors in the estimated proton range in the patient, due to uncertainties in the patient's density map, as this was calculated based on the planning CT. These errors are denoted as the Calibration Curve Errors (CCEs). Secondly, the effects of geometric errors due to deviations between patient position at planning and during the patient position during treatment delivery – these errors are denoted setup errors. The simulations of both the range- and geometric errors are based on the methods described by Lomax (13, 14).

3.2.6.1 Calibration Curve Errors (CCE)

The CT calibration curve converts the HU values into relative proton stopping power as discussed in chapter *2.4.1*. To simulate a range error due to uncertainties in the calibration curve, the reference dose distribution were recalculated with a systematically change in the calibration curve of -1% to -5 %, causing a so-called overshoot, or with a systematically change in the calibration curve of +1% to +5 %, causing a so-called undershoot. By imposing an error into the calibration curve with a positive specified value, the relative

stopping power increases by that specified amount and consequently the proton range decreases relative to the reference plan (undershoot), thus moving the Bragg Peak closer to the source. Similarly, if the applied error had a negative value, the stopping power value decreased and the proton range was prolonged (overshoot), thus moving the Bragg Peak further away from the source.

In the treatment planning system this procedure is implemented in the Range Uncertainty tool. The purpose of the Range Uncertainty tool is to estimate the sensitivity of the treatment plans with respect to range- and geometric uncertainties. This is done by generating a set of recalculated dose distributions - so-called error distributions-based on the reference plans. The user manually defines the magnitude of the calibration curve errors and the dose distributions are recalculated with the initial spot distribution, resulting in a new dose distribution for each uncertainty parameter defined, where the effects of the errors are manifested (37).

3.2.6.2 The simulation of setup errors

The simulation of a set up errors can be obtained by shifting the patients CT dataset relative to the isocenter, this followed by a recalculation of the dose distribution on the shifted versions of the patients 3D CT datasets. Typically this is done in the treatment planning system by shifting the isocenter of the treatment plan along the x-, y- and z-axis. The Range Uncertainty tool in the treatment planning system was also used for the simulation of the setup errors. The isocenter was shifted along the x-, y- and z-axis in the range from 1-5 mm in 1 mm steps. In Figure 3-7, the directions of the shifts relative to the patient are illustrated. Patients were positioned in the prone position, thus a negative lateral shift moved the isocenter in the left direction, while a positive shift moved the isocenter in the right direction. A negative shift in vertical direction moved the isocenter dorsally, and a positive shift moved the isocenter ventrally. Finally, a negative longitudinal shift moved the isocenter in the caudal direction, while a positive longitudinal shift moved the isocenter in the cranial direction. The following recalculation resulted in 30 spatially shifted dose distributions, one for each shift.
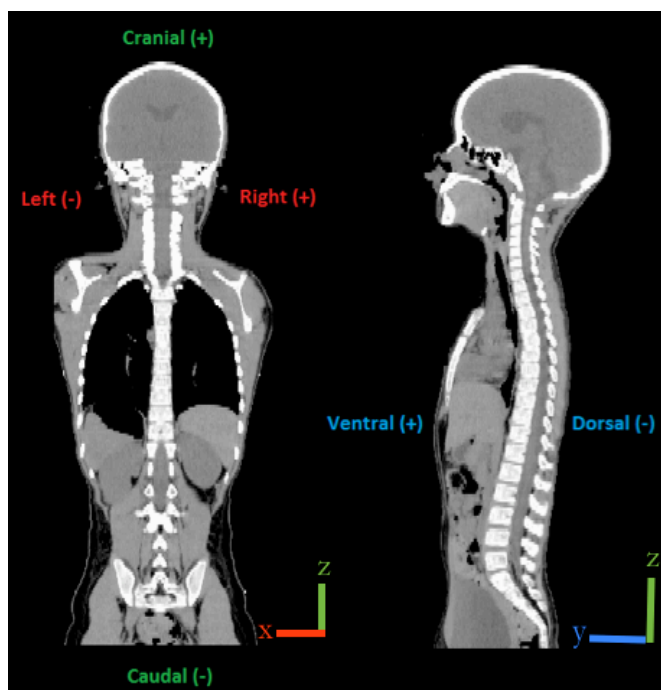
Figure 3-7: The figure shows the directions of the isocenter shift in a patient in a "head first –prone" position. The shifts in the left (-) and the right (+) directions are along the x-axis, the shifts in dorsal (-) and ventral (+) are along the y-axis, and the shifts in caudal (-) and cranial directions are along the z-axis.

3.2.7   Analysis of the results

The error dose distributions were compared to the reference dose distributions by means of an evaluation of the DVHs, by studying and analysing the 2D visualization of the individual error doses dose distributions and by evaluating the Max-Min dose distribution. The DVHs resulting from the use of the Range Uncertainty tool (the reference DVH including the uncertainty curves) could not be exported. Thus, the DVHs were manually analysed in the treatment planning system by observing the dose-volume statistics from each DVH. The individual error doses could be displayed both in colour wash and by isodose curves in the transversal, sagittal and coronal plan with the dose statistics, such as the 3D dose maximum, the 3D dose minimum, the 3D dose maximum and the 3D mean dose for the target volume also displayed. The Max-Min function is implemented as a part of the Range Uncertainty tool. The Max-Min dose distribution tool visualised in what areas in the patient the largest difference in dose occurred. The Max-Min dose is a point-wise calculated dose difference, this based on the initial dose and all the uncertainty doses, and it

shows how robust a plan is with respect to the user defined range- and setup errors. The Max-Min dose distribution is calculated by:

$$D_{Max-Min}(x) = D_{Max}(x) - D_{Min}(x)$$ (Equation 3.3)

The $D_{Max}(x)$ is the maximum dose of all calculated doses, including the initial dose, at a point x. Similarly, the $D_{Min}(x)$ is the minimum dose of all the calculated doses at the same point x (37). The result is displayed in colour wash mode ranged from blue to red, with blue representing small or no difference between the maximum and minimum doses, and with red showing the biggest difference between the maximum and minimum doses.

Several quantitative variables were studied when comparing the reference dose distribution and the error dose distributions. As the endpoint for quantifying what impact the induced range- and geometric errors had on the doses to the target volume, the V $_{34,2Gy (RBE)}$ for the CTV was chosen (this representing the volume receiving the 95% of the prescribed dose). The brain and spinal canal were also evaluated with respect to the V $_{34,2Gy (RBE)}$.

As the primary endpoint for quantifying what impact range- and geometric errors had on the doses to OAR, the D$_{mean}$ and V$_{5Gy}$ was chosen.

Results will be presented both for the individual patients and at the patient group level. Descriptive statistics in terms of the median, the mean with standard deviations (SD), range, maximum and minimum values will be presented both in tables and in figures. The data will also be presented graphically, by DVHs, by dose profiles and with screenshots from the treatment planning system.

3.2.8 Ethical considerations

No patients were involved in this study. Anonymous 3D CT image datasets, from the database in the treatment planning system, were used for the treatment planning of the craniospinal treatment plans.

4 RESULTS

4.1 Water phantom study

In this section the results from the water phantom study are presented. The results from the simulations of changes in the tissue composition in the beam path are given in 4.1.1 and the results from the simulations of geometric misalignments are presented in 4.1.2.

4.1.1 Effects of changes in tissue composition in the beam path

Figure 4-1 and Figure 4-2 displays the depth dose profiles along the central beam axis for the reference proton plan, and the corresponding depth dose profiles from the proton plans that have been recalculated after inserting volumes of bone (Figure 4-1) and volumes of air (Figure 4-2) in the beam path at two different depths. The 2,5 cm thick bone- and air volumes are positioned at a 6,5 cm depth, which is 1 cm prior to the target volume, and at 2,5 cm depth, which is 5 cm prior to the target volume.

These results demonstrate how a shift in the depth dose distribution occurs when changing the material density relative to the calculated reference distribution. At the distal end of the dose profile, the starting point of the rapid dose fall-off is shifted to a shallower depth after traversing the bone volume. The opposite effect is observed by introducing the air volume in the beam path. This will shift the starting point of the dose fall-off to a greater depth compared to the situation in homogenous water. The depth in which the volumes were inserted had little influence on the observed effect at the end of the SOBP, demonstrated by the curves that coincide very well both distally and over the whole SOBP plateau.

In the entrance region however, the dose profiles are different depending on depth of the inserted volumes. In the situation where the bone volume was introduced at the depth of 2,5 cm, a more rapid increase in depth dose occurred, compared to the situation were the bone volume were inserted at 6,5 cm depth. The opposite effect was seen following the introduction of the air volumes at the same positions in depth; the air volume positioned at 2,5 cm resulted in a slower increase in depth dose compared to the air volume located at 6,5 cm depth.
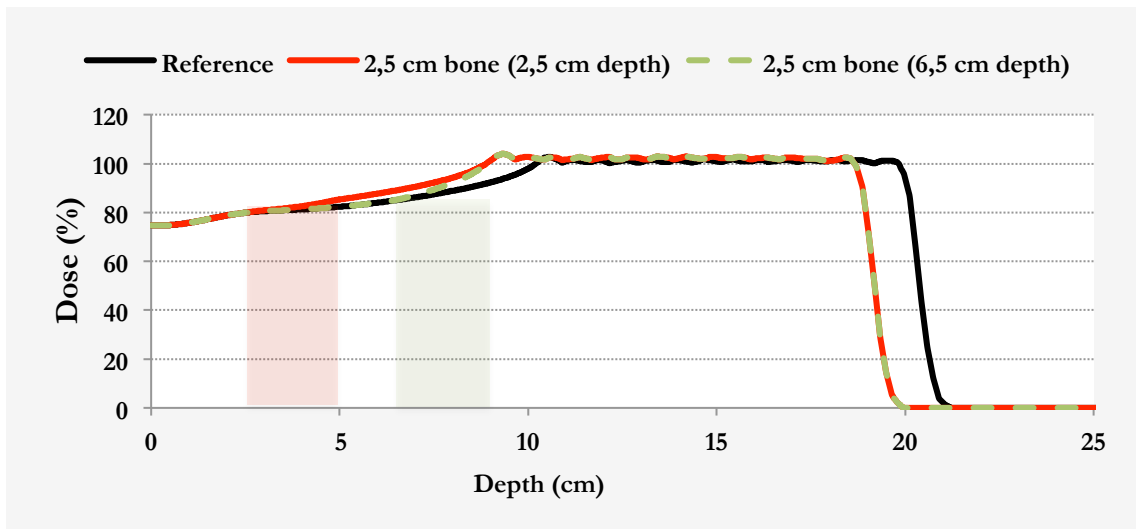
Figure 4-1: The depth dose profiles at the central axis of the phantom after inserting a 2,5 cm thick structure volume of bone at 2,5 cm (solid red line) and 6,5 cm (dashed green line) depth. The solid black line represents the reference depth dose profile. The red shaded and green shaded areas indicate where the beam reach the inserted volume at 2,5 cm and 6,5 cm depth, respectively.
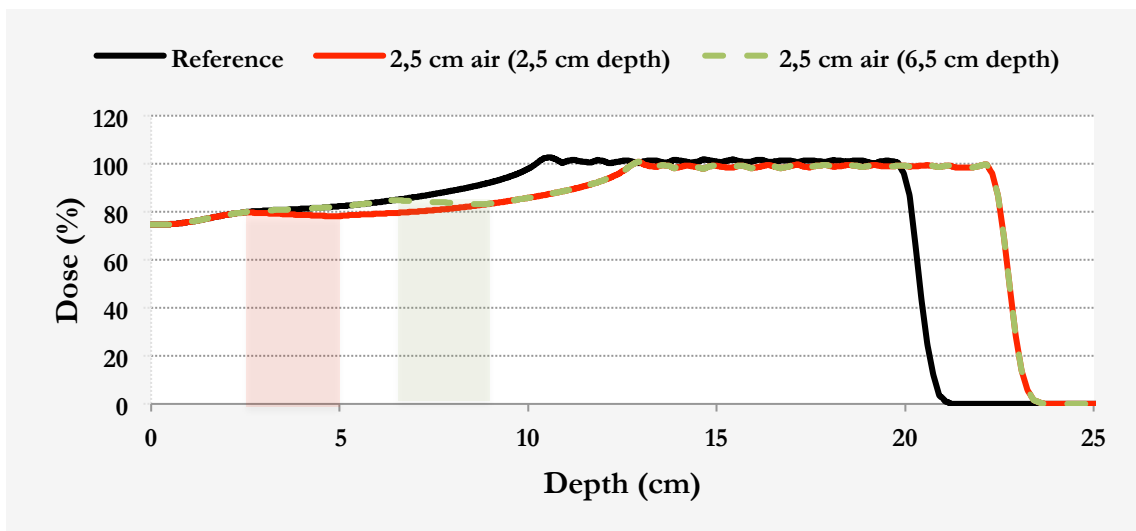

Figure 4-2: The depth dose profiles at the central axis of the phantom after inserting a 2,5 cm thick structure volume of air at 2,5 cm (solid red line) and 6,5 cm (dashed green line) depth. The solid black line represents the reference depth dose profile. The red shaded and green shaded areas indicate where the beam reach the inserted volume at 2,5 cm and 6,5 cm depth, respectively.

The Table 4-I lists the resulting proton range (d90%) and the distal dose fall-off (d80%-d20%) after the insertion of bone and air volumes of different thickness. The table lists the results for the bone and air volumes inserted 1 cm prior to the target volume, but equal results were found when the volumes were inserted 5 cm prior to the target volume.

The range changed as a function of the varying thickness of the inserted bone and air volumes. In the reference dose distribution, with no air or bone volumes inserted, the range was 20,3 cm. The consequence of introducing bone in the proton beam was a continuous reduction in range from 20,0 cm to 19,2 cm, dependent on the thickness of the bone-volumes (from 0,5 cm to 2,5 cm). The opposite effect was seen following the insertion of the air-volumes of the same thickness, a gradual increase in beam penetration that ranged from 20,7 cm with 0,5 cm air to 22,6 cm with 2,5 cm air introduced respectively. The width of the distal dose fall-off, the d80%-d20%, was unperturbed.

Table 4-I: Variation in proton range (d90%) and distal dose falloff (d80%-d20%) in a water phantom following the introduction of volumes of bones and air of various thicknesses in the beam path. The depths where the beam reached the volumes are also listed.

Inserted material		Bone (HU 1000)		Air (HU -1000)	
Volume thickness (cm)	Depth (cm)	Range (cm)	Distal dose fall-off (cm)	Range (cm)	Distal dose fall-off (cm)
0,0	9,0	20,3	-0,5	20,3	-0,5
0,5	8,5	20,0	-0,5	20,7	-0,5
1,0	8,0	19,8	-0,5	21,3	-0,5
1,5	7,5	19,5	-0,5	21,7	-0,5
2,0	7,0	19,3	-0,5	22,2	-0,5
2,5	6,5	19,1	-0,5	22,6	-0,5

Based on the data listed in Table 4-I, the change in range as a function of volume thickness is displayed in Figure 4-3. The trend lines, the polynomial equations obtained based on a fit to the data and the respective R^2-values are also displayed. With respect to changes in the proton range, the results show that inserting a volume of air has a larger impact compared to inserting a bone volume. The slope of the range deviation as function of the inserted structure thickness was nearly twice as steep with the inserted air volumes compared to inserting bone volumes. For both scenarios the change of range as a function of thickness of the inserted volume was approximately linear. The air volume gave an increase of the range with a factor of $\frac{dR}{dx} = 0,94$, and the bone volume gave a reduction of range with a factor of $\frac{dR}{dx} = -0,48$.
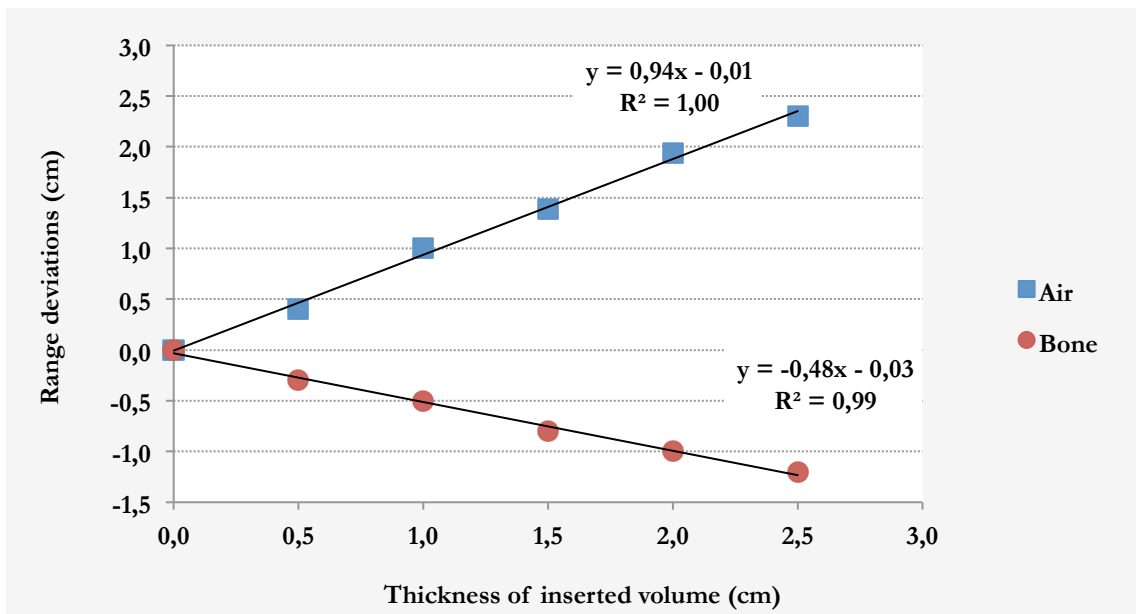

Figure 4-3: The change in range (d90%) as a function of volume thickness. The plot shows the result for volumes of air (blue squares) and bone (red circle). The fit-based polynomial trend line with and the associated R-squared value are displayed for both data sets.

The DVH for the target volume is showed in Figure 4-4. The DVH displays the results for the situations with the 2,5 cm thick volumes of bone and volume of air inserted in the beam path.

Two main features are observable from the dose distribution for the target volume: Firstly, the target DVHs resulting from inserting bone compared to air followed (quite) different patterns. The main effect of the introduction of the bone structure was a lowering of the minimum dose delivered to the target, an effect that was of considerable smaller in magnitude in the DVHs after inserting air volumes. The reference D_{min} = 96,5% was reduced to D_{min} = 1,1% and D_{min} = 85,3% due to inserted bone volumes and air volumes, respectively. The decrease in the 95% target dose coverage was larger from inserting air compared to bone. The $V_{95\%}$ was reduced from the reference $V_{95\%}$ = 100% to $V_{95\%}$ = 89,2% for the situation with the bone volumes, and to $V_{95\%}$ = 76,5% in the situation with air volumes. The results were similar for the bone and air volumes at both 2,5 cm and 6,5 cm depth. Secondly, the target volume DVHs for both inserted materials/density structures located at different depths coincided showing that the position in depth of the bone-volume and air volume had no significant impact on the dose to the target volume. Similar, but less pronounced effects were seen after inserting volumes of smaller thickness.
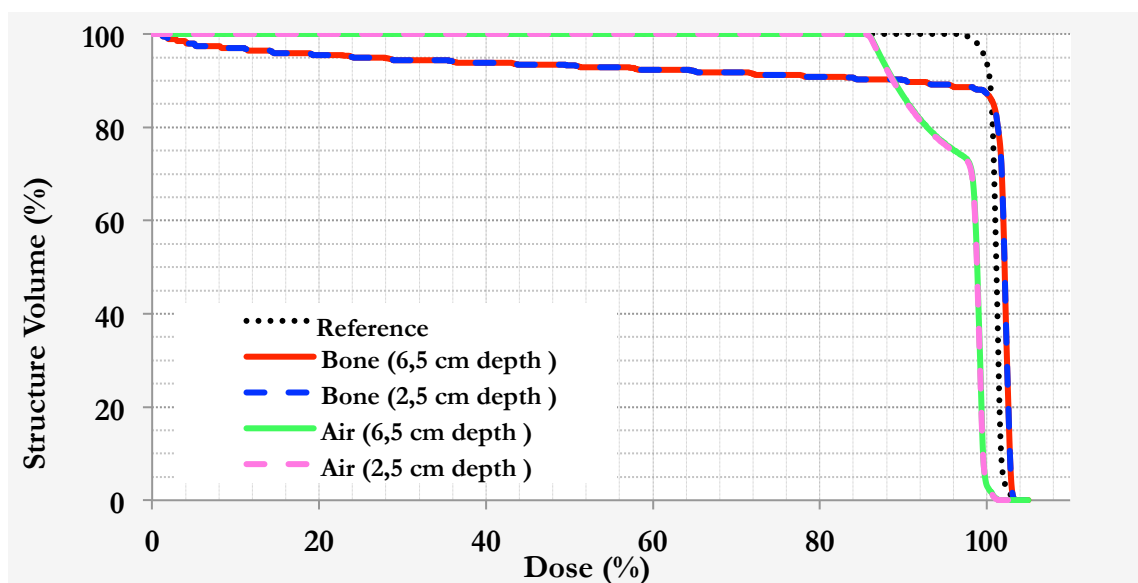

Figure 4-4: Dose Volume Histograms (DVH´s) for the target volume after the insertion of 2,5 cm volumes of air and bone at two different depths. DVH for the reference plan is also showed.

4.1.2 Effects of geometric errors

Table 4-II lists the resulting D_{min}, D_{max} and $V_{95\%}$ for the phantoms A_{water}, B_{bone} and C_{air} after 5 mm isocenter shifts were introduced along the x-, z- and y-axis. The D_{min}, D_{max} and $V_{95\%}$ for the reference plans with no isocenter shifts are also displayed. The shifts along the x- and z- axis were shifts orthogonal to the beam axis, while shifts along the y- axis were parallel to the central beam axis. Since all the water phantoms were symmetric, the shifts in the x-and z-direction were expected to have a similar effect on the dose distribution.

Shifts along the y-axis had no noticeable impact on the minimum dose, maximum dose or the 95% target coverage in any of the phantoms, regardless of whether the shifts were towards the source (negative shifts) or away from the source (positive shifts). Shifts along the x-and z-axis caused a reduction in the D_{min} relative to the calculated reference dose distribution in all the phantoms. Shifts along the x-axis caused the largest reduction in D_{min} in phantom A_{water}. In phantom B_{bone}, the shift in the x-direction had a slightly larger impact on the D_{min} compared to the shifts in the z-direction, while in phantom C_{air} the effect of shifts in the x- and z directions were comparable. Shifts in x- and z-direction caused an increase in D_{max} in phantom B_{bone} and C_{air}, while D_{max} was almost unaffected in phantom A_{water}. The 95% target coverage ($V_{95\%}$) was also degraded in all dose distributions with the largest reduction found in phantom C_{air}.

Table 4-II: The effect of isocenter shifts on the D_{min}, D_{max} and $V_{95\%}$ for the homogeneous phantom (A_{water}) and the heterogeneous phantoms (B_{bone} and C_{air}). Results are presented for the target volume with no shifts and after 5 mm shifts along the x-, z- and y-axis.

Parameter	D_{min} (%)			D_{max} (%)			$V_{95\%}$ (%)		
Plan/shifts	A_{water}	B_{bone}	C_{air}	A_{water}	B_{bone}	C_{air}	A_{water}	B_{bone}	C_{air}
Reference	95.0	95.0	95.0	103.5	104.4	108.6	100.0	100.0	100.0
x+5 mm	72.3	65.6	70.4	103.5	111.5	112.9	97.6	96.6	96.0
z+5 mm	79.4	70.9	69.6	103.5	108.1	114.4	97.8	97.0	96.4
y+5 mm	95.0	94.9	95.1	104.0	104.9	109.9	100.0	100.0	100.0
y-5 mm	95.1	95.0	95.1	103.1	104.0	108.1	100.0	100.0	100.0

Abbreviations: D_{min}: minimum dose delivered to target volume, D_{max}: maximum dose delivered to target volume, $V_{95\%}$: Volume receiving at least 95% of prescribed dose.

The effects on the target dose homogeneity resulting from the geometric misalignments depended not only on the shift direction, but also differed between the various phantoms, as illustrated in Figure 4-5. The variation in the calculated HI is displayed for the reference plan with no shifts, and after the isocenter shifts for all the phantoms. The shifts of isocenter along the beam direction had hardly any impact on the HI as opposed to the shifts in x-and z- direction. In phantom A_{water} the HI was increased from 0,04 to 0,08 and 0,09 for z and x shifts respectively. The similar result from phantom B_{bone} was an increase from 0,03 to 0,11 and 0,13. The largest effect of isocenter shifts was seen in phantom C_{air} with an increase in HI from 0,04 to 0,14 and 0,15 for isocenter shifts in z and x directions.
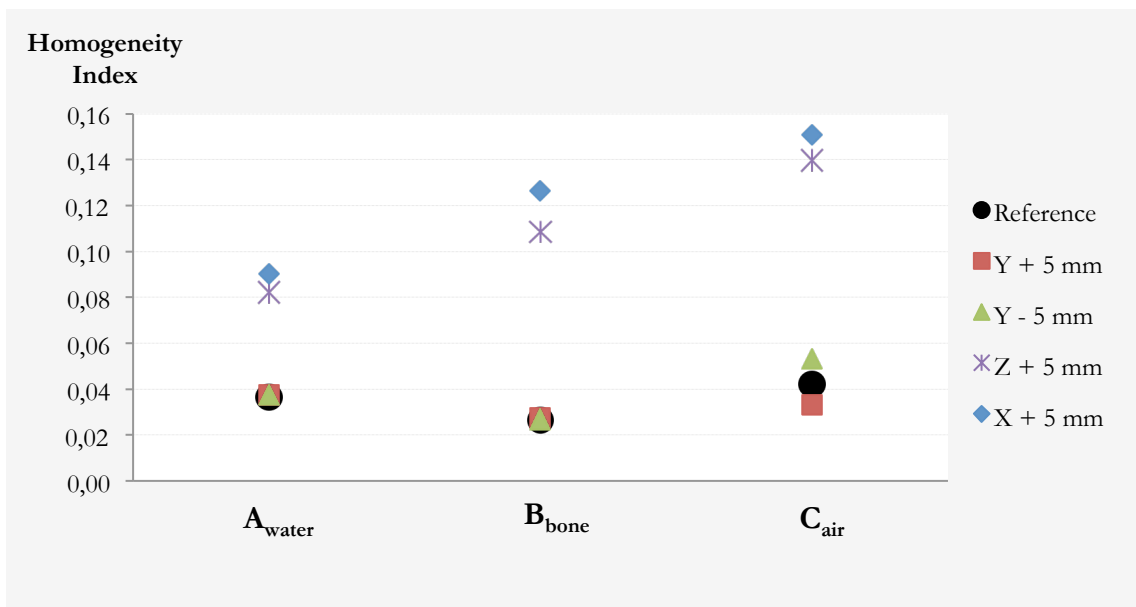
Figure 4-5: Dose homogeneity in the target volume, expressed by the Homogeneity index (HI) for all three phantoms. The impact of isocenter shifts on the Homogeneity Index (HI) is displayed. The reference HI (no shifts) is also showed. A HI of 0 is ideal. The $D_{98\%}$, $D_{2\%}$ and the $D_{50\%}$ are used for the calculation of the HI.

Figure 4-6 shows the total dose distribution (top panel) and the 95%-107% dose distribution (bottom panel) after lateral isocenter shifts of +5 mm. The dose distribution is displayed in colour wash for plans on water phantom A_{water}, B_{bone} and C_{air}. The isocenter

shift caused a loss in the 95% target coverage along the lateral border in all the phantoms. Two additional effects could also be seen distal to the target volume in the heterogeneous phantoms. In phantom B$_{bone}$, hotspots are apparent inside the target: Especially in line with the inner bony structure on the left hand side in the figure, as evident from the 95%-107% dose distribution. In the extension of this line indicating the bone, a small area of 50% dose level extended outside the target volume, as observed in the image with the total dose distribution in the upper middle panel. Moreover, an area of reduction in the 95% dose coverage was seen distally in the target volume on the contralateral side, this also in line with the lateral edge of the bone volume. A similar effect, now more pronounced, was seen for the phantom C$_{air}$, with the hotspot appearing on the distal left side of the air volume, and with decay in dose coverage at the distal right side.
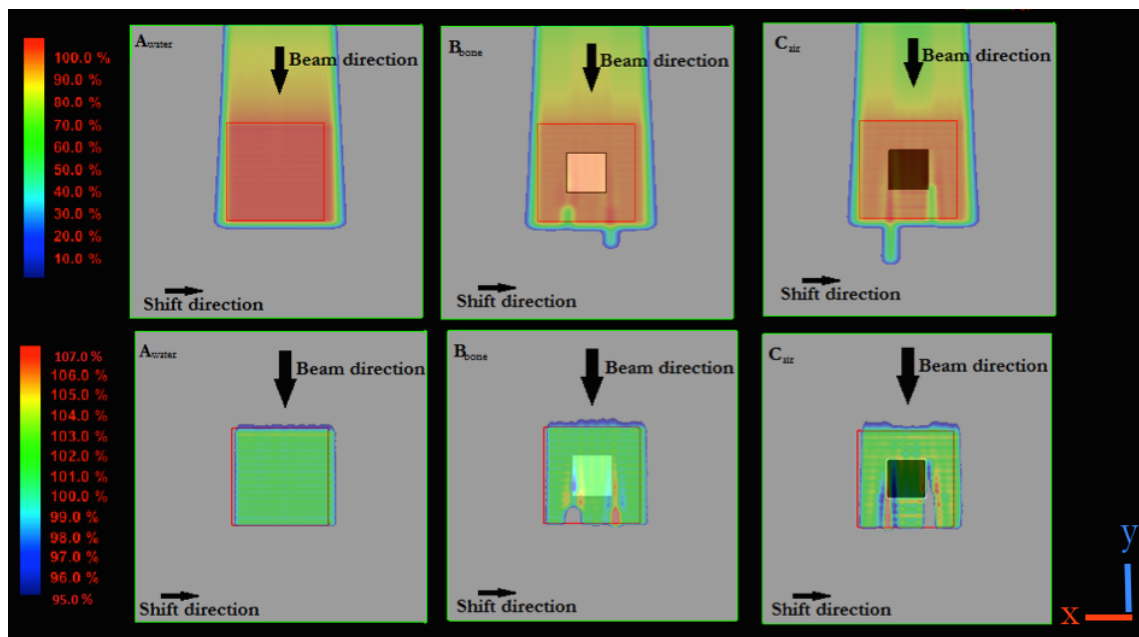

Figure 4-6: The effect on the dose distribution of a 5 mm lateral isocenter shift in homogeneous (A) and heterogeneous (B and C) water phantoms. The figure displays the total dose distribution in the top panels and the 95%-107% dose distribution in the panels below. The target volume is indicated by the red solid line.

Figures 4-7a-c) give a further illustration of the different effects presented in Figure 4-6, and show the lateral dose profiles in 20 cm depth, a depth that corresponds with the distal border of the target volume. Thus, the dose profiles coincide with the distal target boundary, as illustrated at the right top corner in the figures. The non-shifted dose profiles from the reference plans (solid lines) and the dose profiles after a 5 mm lateral shift are displayed for phantom A_{water} (Figure 4-7a)), phantom B_{bone} (Figure 4-7b)) and phantom C_{air} (Figure 4-7c)). The arrows in the figures indicate the direction of the isocenter shift. The dose profiles in phantom B_{bone} and C_{air} are distributed with a different pattern than the corresponding dose profile in phantom A_{water}. In all the phantoms all dose profiles were shifted in the same direction as the isocenter shift, with the magnitude of 5 mm at the 50% dose level. However, in addition to the spatial position shift of the dose profile for all phantoms, a substantial dose decrease and increase were observed along the dose profiles in both phantom B_{bone} and C_{air}. The alteration in dose appeared in line with the lateral edges of the inner structure in both phantoms. In phantom B_{bone} the dose reduction occurred at the left edge of the inner structure, with the dose dropping to 65,6% of prescribed dose, corresponding to the D_{min} in the dose plan. The increase in dose appeared at the contralateral side, at the right edge. A similar pattern was seen in phantom C_{air}, but in this case, the situation was the inverse compared to the situation in phantom B_{bone}, with a dose increase and a dose decrease at the opposite sides of the inner structure.
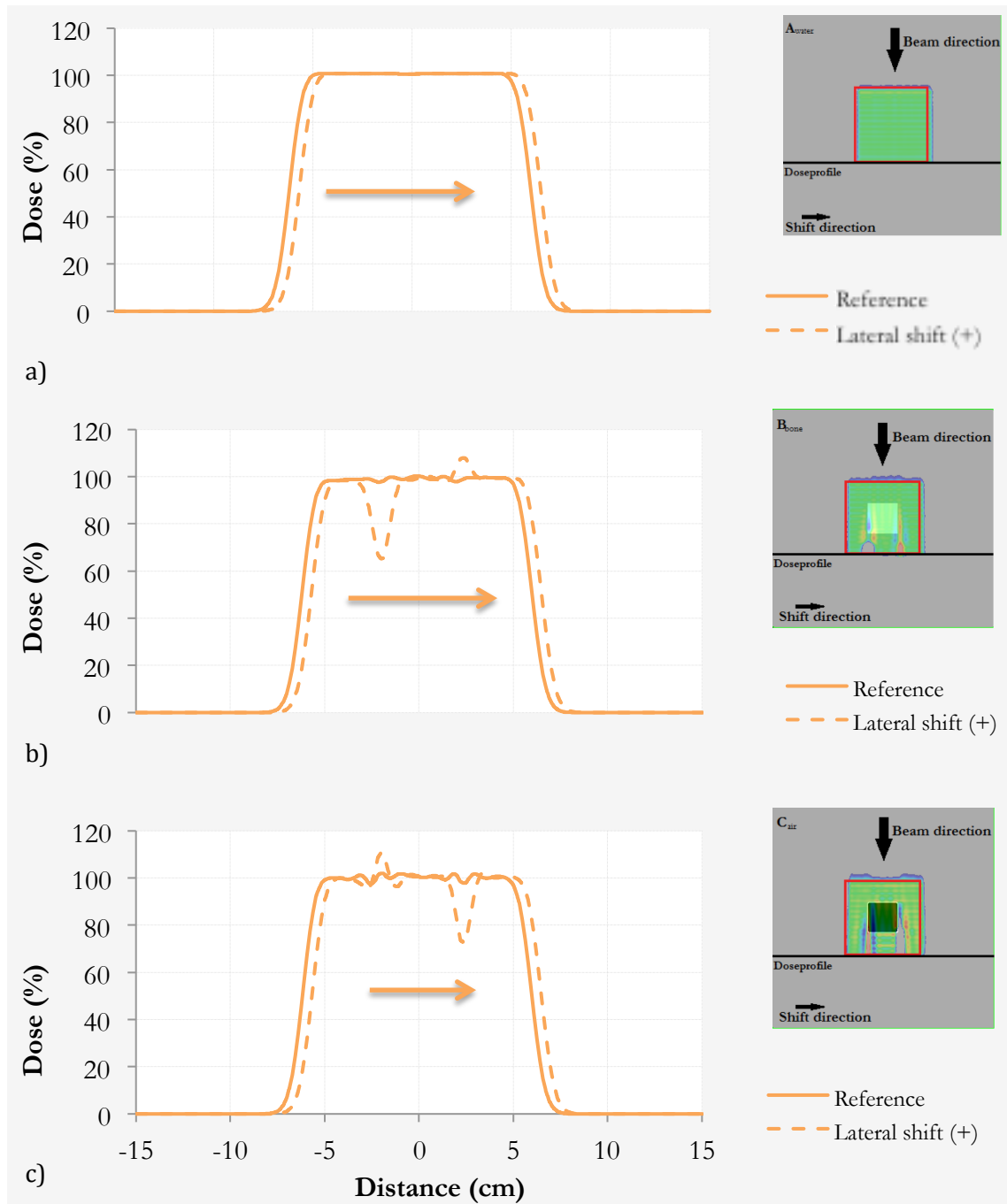
Figure 4-7: The lateral dose profiles at 20 cm depth, which corresponds to the distal border of the target as showed in figure on left top in the figures, are displayed in a) for phantom A_water, in b) for phantom B_bone and in c) for phantom C_air. The dose profiles from the reference plan (solid lines) and the +5 mm lateral shifted plan (dashed lines) are presented. The direction of the shift is indicated with the arrows. Distance = 0 equals the centre of the phantom.

4.2   The craniospinal treatment plans

In this section the results for the robustness analysis of the craniospinal treatment plans are presented. An evaluation of the reference treatment plans, which were used as basis for the simulations of the various errors, are given in 4.2.1, the results from the simulations of the calibration curve errors (CCE) are presented in 4.2.2 and the results from the simulation of the setup errors are presented in 4.2.3.

4.2.1   Evaluation of the dose distribution in the reference treatment plans

4.2.1.1 Dosimetric data for the target volumes

In Table 4-III the dose statistics for the PTV, the CTV, the brain and the spinal canal are summarized for the 6 study patients. The mean values with standard deviations are presented for 5 different parameters: the D_{min}, D_{max}, $D_{98\%}$, $D_{2\%}$ and $V_{95\%}$. The $V_{95\%}$ equals $V_{34,2Gy (RBE)}$ and corresponds to the target volume dose coverage. Generally the plans had satisfactory target volume dose coverage. For the CTV, the brain and the spinal canal, the $V_{95\%}$ was a 100%, and for the PTV it was 99,9%. For all the target volumes the near minimum dose, $D_{98\%}$, was better than 95% of the prescribed dose, ranging from 97.8 % of the prescribed dose for the PTV (lowest) to 98% of the prescribed dose for the CTV (highest). The near-maximum dose, $D_{2\%}$, was less than 103% in all target volumes. The results were consistent across the patient group, as also demonstrated by the low standard deviations.

Table 4-III: The table lists the descriptive statistics for 5 different parameters for the PTV, the CTV, the brain and the spinal canal volume. Mean values and standard deviations are presented for $D_{98\%}$, $D_{2\%}$, $V_{95\%}$, D_{min} and D_{max}.

Parameter	PTV Mean (%)	SD	CTV Mean (%)	SD	Brain Mean (%)	SD	Spinal canal Mean (%)	SD
$D_{98\%}$	97,8	0,3	98,0	0,2	97,9	0,3	98,0	0,2
$D_{2\%}$	102,8	0,6	102,3	0,7	102,4	0,7	101,8	0,2
$V_{95\%}$	99,9	0,1	100,0	0,0	100,0	0,0	100,0	0,0
D_{min}	84,4	4,7	93,4	1,1	94,7	0,7	96,3	0,5
D_{max}	111,9	2,0	111,1	2,5	111,1	2,5	105,6	1,5

Abbreviations: D_{min} = minimum dose delivered to target, D_{max}= maximum dose delivered to target, $V_{95\%}$: Volume receiving at least 95% of prescribed dose, $D_{98\%}$ = least dose received by 98% of target volume, $D_{2\%}$= least dose received by 2% of target volume.

Figure 4-8a-d) shows the dose distribution for patient II. The total dose distribution is displayed in sagittal plane in a) and in transversal plane in c), while the 95% -107 % dose distribution is displayed in the sagittal plane in b) and the transversal plane in d). The 95% isodose covers the brain, the spinalcanal and the entire corpus vertebra with a homogenous dose as displayed in Figure 4-8b). A few hotspots can be observed towards the surface of the cranium (Fig. 4-8d)). There is a rapid dose falloff providing sparing of the tissue ventral to the vertebrae (Fig 4-8a) and c)).
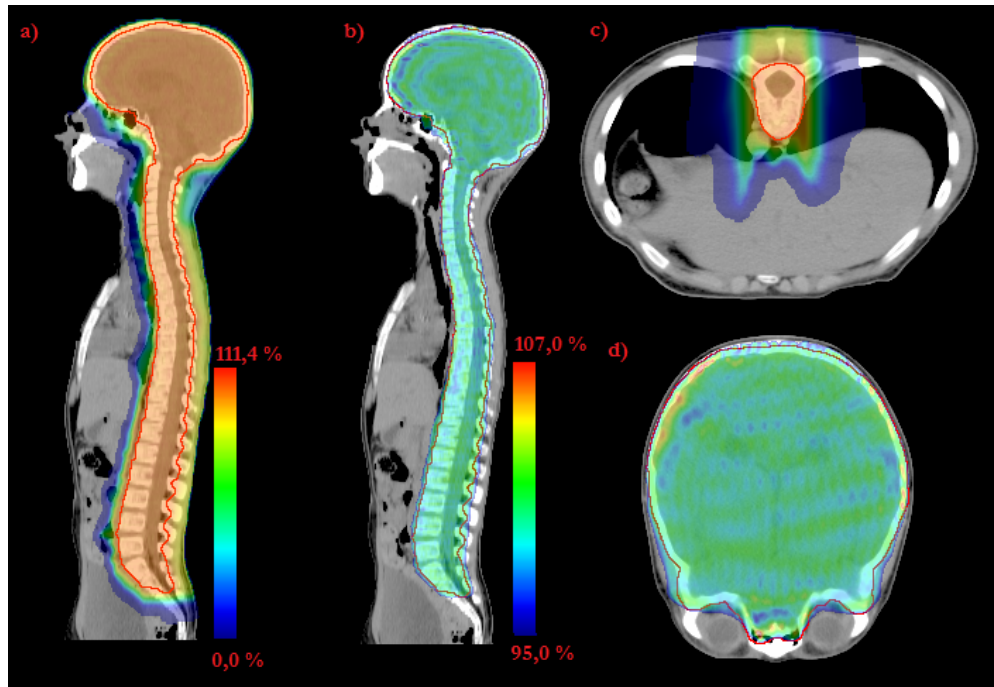
Figure 4-8: The dose distribution for patient II: The total dose distribution is displayed in the sagittal plane in a) and the transversal plane in c). The 95%-107% dose distribution is displayed in the sagittal plane in b) and the transversal plane in d). The dose levels are scaled as displayed by the colour bar in a) and b).

The dose conformity and homogeneity for the PTV was evaluated by means of the CI, the CN and the HI. The result is presented in Table IV, which lists the mean values and the standard deviation for the CI, CN and HI. For the calculation of the indices the $D_{2\%}$, $D_{98\%}$ and $D_{50\%}$ were used for the computation of the HI, and the $V_{95\%}$ was used for the calculation of the CI and CN. The CI for the PTV was 1,0 for all the patients (SD =0). Similarly, the CN was 0,87 with a standard deviation of 0,02. The HI was 0,05 for the PTV with a standard deviation of 0,01.

	PTV		
Index	HI	CI	CN
Mean	0,05	1,00	0,87
SD	0,01	0,00	0,02

4.2.1.2 Dosimetric data for the OAR

Descriptive statistics for the doses to the OAR are summarized in Table 4-V.

The D_{mean} to the heart was 0,6 Gy (RBE) with a SD of 0,3. The D_{mean} for the left kidney was 1,8 Gy (RBE) with a SD of 0,4. For the right kidney, the D_{mean} was 2,0 Gy (RBE) with a SD of 0,4.

The highest doses could be seen in the eyes with e.g. a D_{mean} of 11,7 Gy (RBE) with a SD of 2,1, and a D_{mean} of 12,4 Gy (RBE) with a SD of 1,8 for the left and right eye, respectively. This corresponds to 32,5% and 34,4% of the prescribed dose.

The mean doses to the thyroid ranged between 2,9 Gy (RBE), corresponding to 8% of prescribed dose, and 11,5 Gy (RBE), corresponding to 31,9% of prescribed dose, with an average of 7,2 Gy (RBE), corresponding to 20% of prescribed dose. The large spread in the data for the thyroid could also be seen in the $V_{5Gy\ (RBE)}$ and $V_{10Gy\ (RBE)}$.

Table 4-V: Descriptive dose statistics for the lenses, lungs, heart, kidneys, thyroid and eyes. The results for $V_{5Gy (RBE)}$, $V_{10Gy (RBE)}$ and $V_{20Gy (RBE)}$ are displayed in relative values (%). Results for D_{mean} and D_{max} are displayed in absolute values [Gy (RBE)].

Structure, dose statistics	Mean	SD	Min	Max	Structure, dose statistics	Mean	SD	Min	Max
Left lens					**Right lens**				
D_{mean}	3,7	0,9	2,5	4,7	D_{mean}	3,8	0,9	2,7	4,9
D_{max}	7,0	1,5	4,8	9,1	D_{max}	7,0	1,5	5,2	9,0
Heart					**Thyroid**				
D_{mean}	0,6	0,3	0,3	1,2	D_{mean}	7,2	3,3	2,9	11,5
D_{max}	25,4	6,1	19,5	37,0	D_{max}	29,9	1,8	27,0	31,9
$V_{5Gy (RBE)}$	4,2	2,1	1,9	7,7	$V_{5Gy (RBE)}$	51,0	27,3	16,4	82,4
$V_{10Gy (RBE)}$	1,7	1,3	0,6	4,2	$V_{10Gy (RBE)}$	28,7	15,1	10,2	51,1
$V_{20Gy (RBE)}$	0,2	0,4	0,0	1,1	$V_{20Gy (RBE)}$	7,4	4,8	3,6	16,6
Left lung					**Right lung**				
D_{mean}	2,3	0,5	1,5	3,2	D_{mean}	3,2	0,6	2,0	3,6
D_{max}	35,5	0,6	34,5	36,2	D_{max}	35,9	0,4	35,4	36,4
$V_{5Gy (RBE)}$	13,4	2,8	8,9	17,6	$V_{5Gy (RBE)}$	16,9	3,3	10,4	19,2
$V_{10Gy (RBE)}$	8,8	2,1	5,9	12,3	$V_{10Gy (RBE)}$	12,1	2,3	7,6	13,7
$V_{20Gy (RBE)}$	3,6	1,2	2,3	5,9	$V_{20Gy (RBE)}$	6,5	1,3	4,1	7,8
Left kidney					**Right kidney**				
D_{mean}	1,8	0,4	1,4	2,5	D_{mean}	2,0	0,4	1,4	2,6
D_{max}	31,0	3,4	24,7	34,1	D_{max}	30,2	1,9	27,7	33,2
$V_{5Gy (RBE)}$	11,9	2,4	8,8	16,2	$V_{5Gy (RBE)}$	13,0	2,7	9,1	16,7
$V_{10Gy (RBE)}$	5,7	1,3	4,9	8,1	$V_{10Gy (RBE)}$	6,2	1,4	4,5	8,2
$V_{20Gy (RBE)}$	1,3	0,6	0,5	2,3	$V_{20Gy (RBE)}$	1,4	0,5	0,9	2,0
Left eye					**Right eye**				
D_{mean}	11,7	2,1	9,8	15,5	D_{mean}	12,4	1,8	10,1	14,3
D_{max}	34,3	1,1	32,9	36,0	D_{max}	34,5	1,0	32,7	35,6
$V_{5Gy (RBE)}$	67,7	8,5	58,4	79,9	$V_{5Gy (RBE)}$	70,0	6,9	62,8	77,7
$V_{10Gy (RBE)}$	48,6	8,5	40,3	62,1	$V_{10Gy (RBE)}$	51,7	7,5	42,4	60,0
$V_{20Gy (RBE)}$	21,7	7,1	16,1	35,3	$V_{20Gy (RBE)}$	24,8	6,5	15,8	31,3

4.2.2   Effects of calibration curve errors

4.2.2.1 The Max-Min dose distribution

Figure 4-9 shows the calculated Max-Min dose distribution for patient IV resulting from imposed calibration curve errors (CCE) from +1% to 5% (representing undershoot) and from -1% to 5% (representing undershoot). Hence, 10 different error distributions, as well as the reference dose distribution, are included in the calculation of the Max-Min dose distribution. Note that the images do not show the change in the dose relative to the reference plan, but the calculated differences between the maximum and minimum dose at each point. The dose differences are scaled as displayed by the colour bar to the right in Figure 4-9. Clearly the dose differences were small within the target volumes. Distal to the PTV the differences were more apparent, exposing a band along the spine of which the dose differences were of more than 40%.
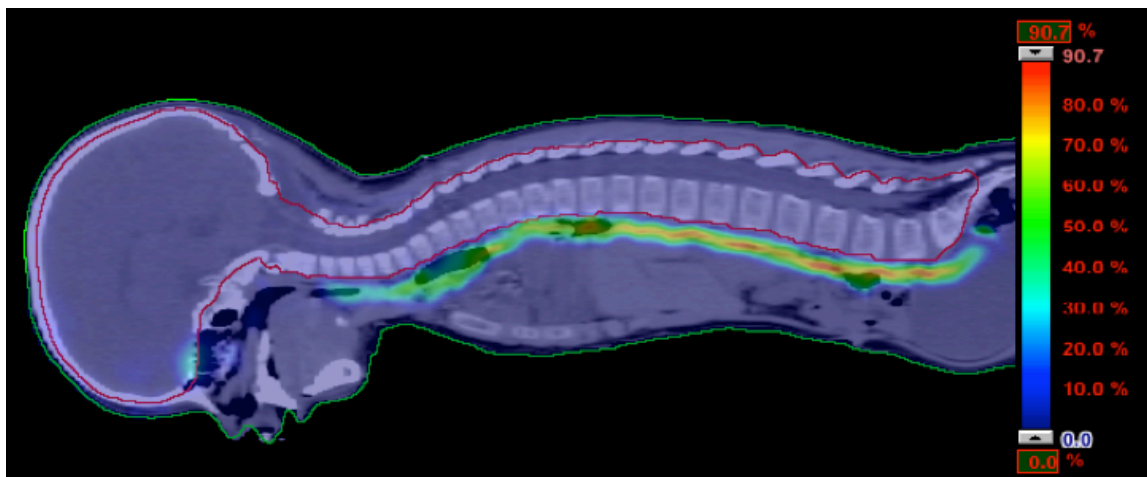

Figure 4-9: The Max- Min dose distribution after CCEs of ±1% to ±5%. The dose difference is displayed by the colour bar to the right in the image.

4.2.2.2 Dose coverage for the target volumes

The overall dosimetric effect of the 1% to 5% overshoot and the 1% to 5% undershoot is presented for one representative patient in Figure 4-10a-d). The figure displays both the DVH for reference plan (the solid lines) and the recalculated error DVHs (the dotted lines) for the spinal canal and the brain. The resulting DVHs following a 1% to 5 % overshoot is showed in Figure 4-10a) for the spinal canal and in Figure 4-10c) for the brain. The resulting DVHs following 1% to 5 % undershoot is presented in Figure 4-10b) for the spinal canal and in Figure 4-10d) for the brain.

The ±1% to ±5% CCEs had no large impact on the overall doses to the spinal canal or the brain. The analysis of the DVHs for the brain, and to some extent for the spinal canal, revealed a very small, but systematic reduction in the doses following the 1% to 5% overshoot, this demonstrated by the systematically shifted error curves toward the lower dose levels.

A comparable, but opposite effect could be observed for the spinal canal after the 1% to 5% undershoot; the error DVHs were systematically shifted in very small steps towards the higher doses. The error DVHs for the brain showed a slightly different pattern. Undershoot reduced the steepness of the DVH curve and resulted in an increased D_{max}, a reduced D_{min} and consequently a less homogenous dose distribution.
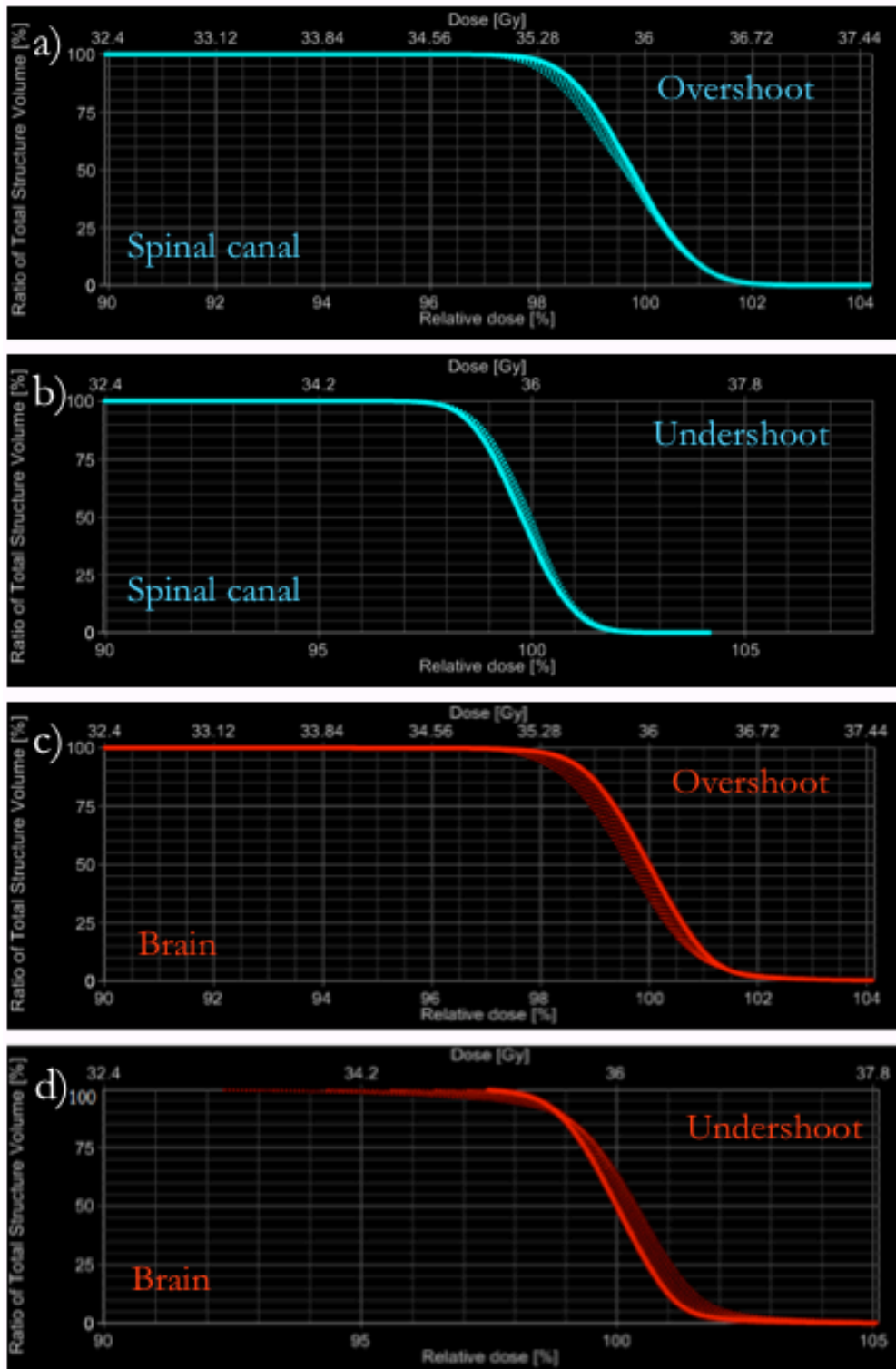
Figure 4-10: DVH from patient III showing the effect on the CTV after introducing a CCE of -1% to -5% on the top panel (the overshoot situation), and +1% to +5% on the bottom panel (the undershoot situation). The solid lines represent the reference plan, and the dotted lines the error curves. The dose is displayed on the x-axis from the 90% level.

The plot in Figure 4-11 shows the $V_{34,2\,Gy\,(RBE)}$ ($V_{95\%}$) as a function of the CCE magnitude. Group-averaged results are presented for the brain, the spinalcanal and the CTV. The $V_{34,2\,Gy\,(RBE)}$ for the reference plan, which had 0% CCE, is also displayed. The scale on the y-axis starts at 96%.

Figure 4-11 shows that the spinalcanal sustained the 95% dose coverage regardless of any CCE. The overshoot of 1-5% did not affect the $V_{34,2\,Gy\,(RBE)}$ for the brain and the CTV, nor did a 1% undershoot. With a further undershot of 2-5 % an increasingly reduction in the $V_{34,2\,Gy\,(RBE)}$ for the brain and CTV was seen. The situation with a 4% and 5 % undershoot resulted in a reduction of the $V_{34,2\,Gy\,(RBE)}$ for the brain from 100% to 98,4 % and 97,1% respectively. Similarly, with a 4% and 5 % undershoot the $V_{34,2\,Gy\,(RBE)}$ for the CTV was reduced to 98,5 % and 97,4%, respectively. For the 2% and 3% undershoot the 95% dose coverage was slightly reduced, but still > 99% for both the brain and the CTV.
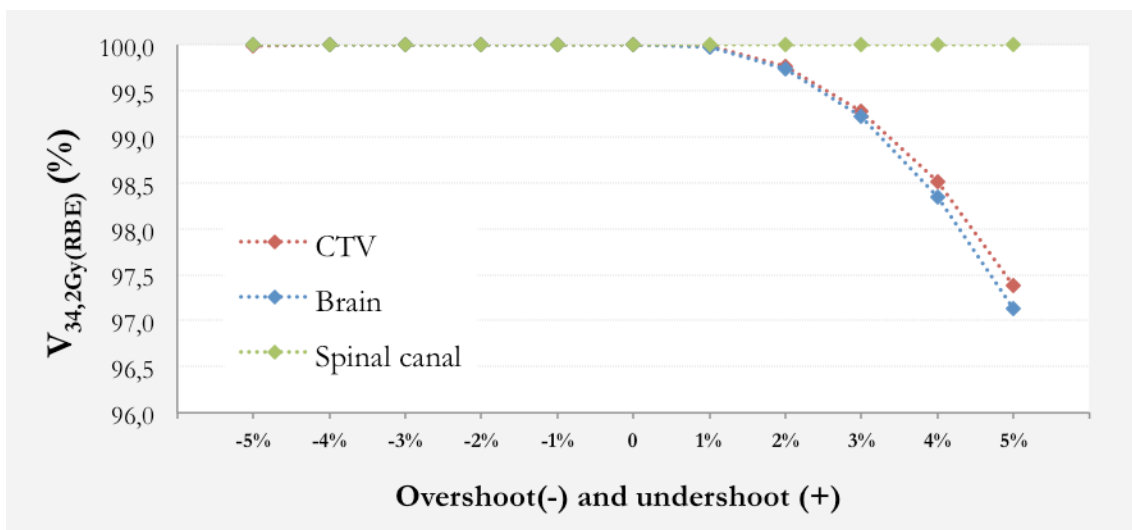

Figure 4-11: The plot presents the mean result for $V_{34,2\,(Gy\,(RBE))}$ across the patients as a result of 1% to 5% overshoot and 1% to 5% undershoot. The effects on the CTV, the brain and the spinal canal are presented. The magnitude of the CCEs is displayed on the x-axis and the $V_{34,2\,Gy\,(RBE)}$ is displayed on the y-axis.

Figure 4-12a-c) shows the 95%-107% dose distribution for the brain for patient VI in the transversal view. The dose distribution is displayed for the plan with no CCE in image a),

the dose distribution after a 5% overshoot is presented in image b) and after a 5% undershoot in image c). The yellow arrows indicate the beam direction of the cranial treatment fields.

Compared to the reference plan displayed in Figure 4-12a), both overshoot and undershoot resulted in increased dose inhomogeneity throughout the brain, this displayed by the increased amount of hot spots (indicated by the red arrows in image b) and c)) and cold spots (indicated by the blue arrows in the images). A loss in the 95% dose coverage, caused by the 5% undershoot is clearly visible in Figure 4-12c). The cold spots appeared for the large part laterally in the brain, towards the cranium, but could also be observed well inside the brain. A band of hot spots could also be seen at the right side of the brain. In Figure 4-12b), which displays the consequence of the overshoot, increased amount of hotspots could be observed. These hotspots appeared for a large part in, or in relation with, the bony structures of the skull.
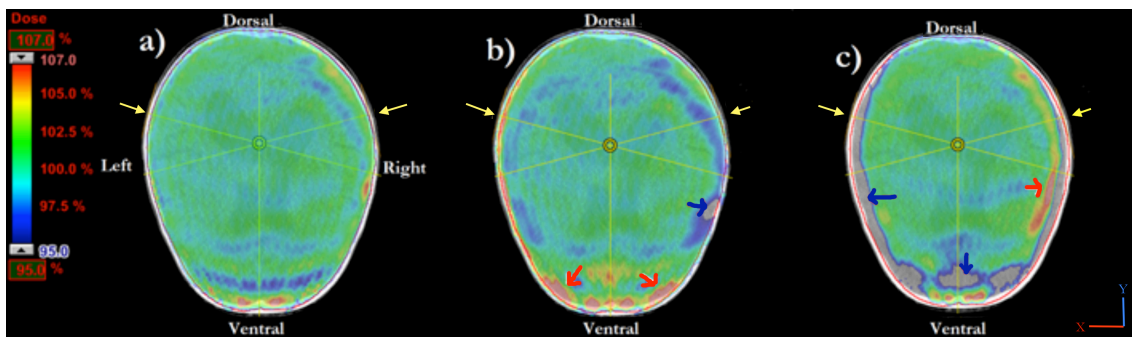

Figure 4-12: The 95% -107% dose distribution displayed for the reference treatment plan for patient VI in a). The corresponding dose distribution after a 5% overshoot displayed in b) and after a 5% undershoot in c). The yellow arrow indicates the beam direction of the cranial treatment fields, the red and blue arrows indicates the hot spots and cold spots, respectively.

4.2.2.3 Doses to the organs risk

In Figure 4-13a-b) the DVHs from one representative patient are presented, demonstrating how the ± 1 to ±5% CCEs influenced the overall doses to the OAR. The figure displays the DVH from the reference plan (the solid lines), and the recalculated error-DVHs, each of which contains a single value of the CCE (dotted lines). DVHs for the right eye, the thyroid, the heart and the right kidney are displayed. The resulting DVHs following a 1% to 5 % overshoot is showed on the top panel, while the resulting DVHs following 1% to 5% undershoot is presented on the bottom panel.

Generally, an increasing overshoot caused a continuous increase in doses to the OARs, this demonstrated by the systematically shifted DVHs. A similar, but opposite effect were seen following an increasing undershoot, which resulted in a continual dose-reduction. The dose-increase induced by the overshoot appeared to be more pronounced than the dose-decrease induced by undershoot. This is demonstrated by the greater dispersion between the reference DVHs and the error DVHs in the figure on top panel of the figure. Further, the thyroid suffered the largest changes in dose. The eyes and the heart were only slightly affected, while the impact on the dose to the kidneys and lungs were insignificant.
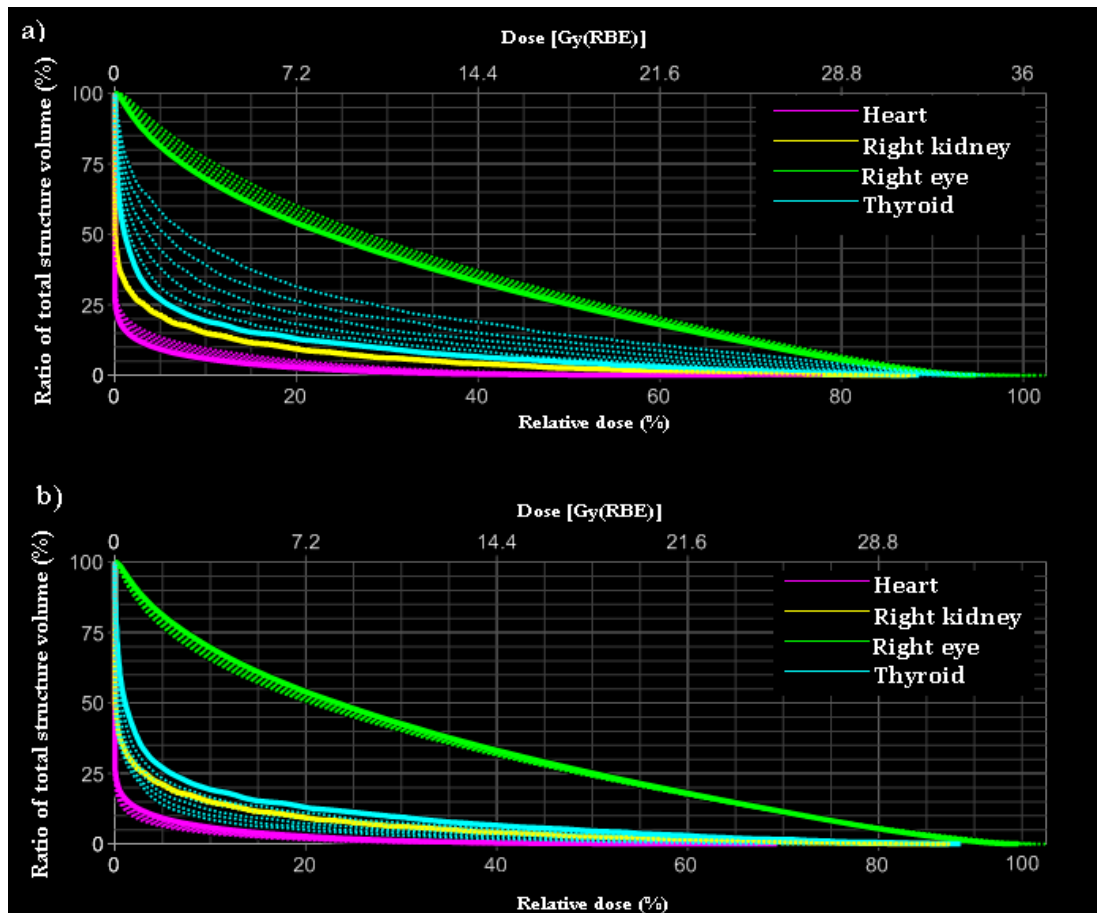
Figure 4-13: DVHs with error curves from patient IV after overshoot and undershoot of 1% to 5%. The result for heart, right kidney, right eye and thyroid is presented in a) after overshoot and in b) after undershoot. The solid lines represent the reference curves from the plan with no errors, and the dashed lines represent the error curves.

Figure 4-14 presents the resulting D_{mean}, including the group-averaged value, for the heart for patient I-VI after CCEs from ±1% to ±5%. The 0% represents the D_{mean} from the reference plan. Compared to the reference plans, the overshoot caused a gradually increase of the D_{mean}, while the opposite effect could be observed for the undershoot. Although the individual D_{mean} differed between the patients, the changes revealed for the most part a similar tendency, with an approximately equal increase or decrease in dose, except for patient V, which seemed to be affected, especially by the overshoot, to a greater extent than the other patients. However, for all patients, the changes in D_{mean} were in general small and the results displayed moderate changes.
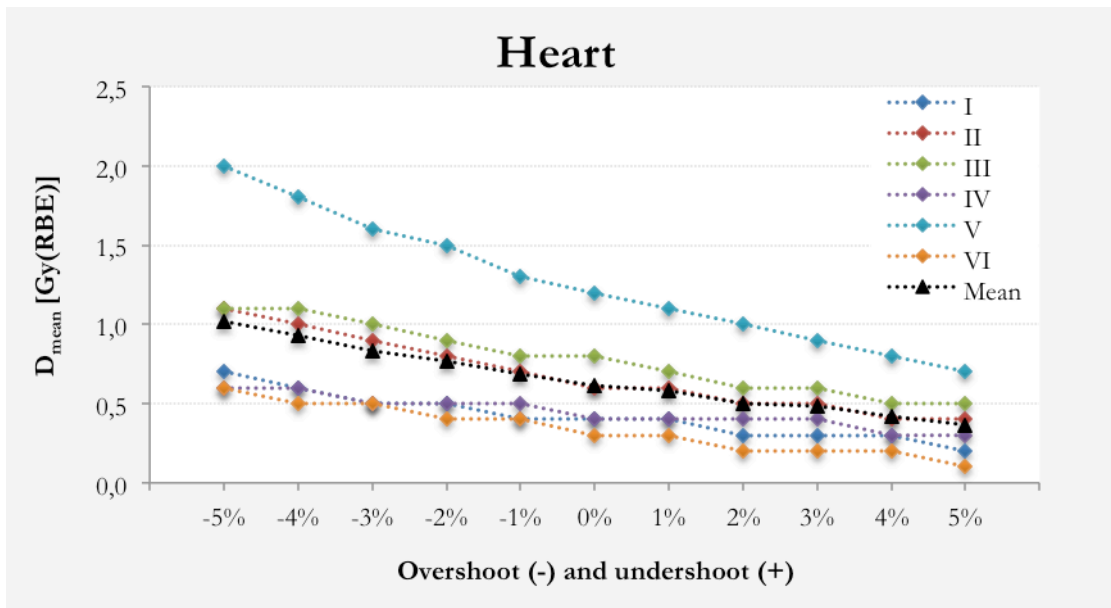
Figure 4-14: The individual results for the D_{mean} following CCEs of ±1% to ±5%. The results for patient I-VI, including the mean values across the patient group, are displayed. Zero % CCE corresponds to the reference plans.

In Figure 4-15 the resulting D_{mean} for the thyroid stemming from the over-and undershoot from 1% to 5% is displayed for patient I-VI. The 0% represents the D_{mean} from the reference plan and the group-averaged D_{mean} is also displayed.

Approximately equal trends could be observed for all the patients. The D_{mean} experienced a systematic and gradually increases as a result of the imposed overshoot of 1% to 5%, while a continuous decrease in D_{mean} followed the increasing undershoot.

A 3% overshoot resulted in an increase of the group-averaged D_{mean} in the order of almost 3 Gy (RBE), from 7,2 Gy (RBE) in the reference plan, to 10,1 Gy (RBR), which corresponds to a dose difference of 47%. The D_{mean} after the 4% and 5% overshoot were 11,3Gy (RBE) and 12,5Gy (RBE), corresponding to a dose change of the order of 66% and 87%, respectively.
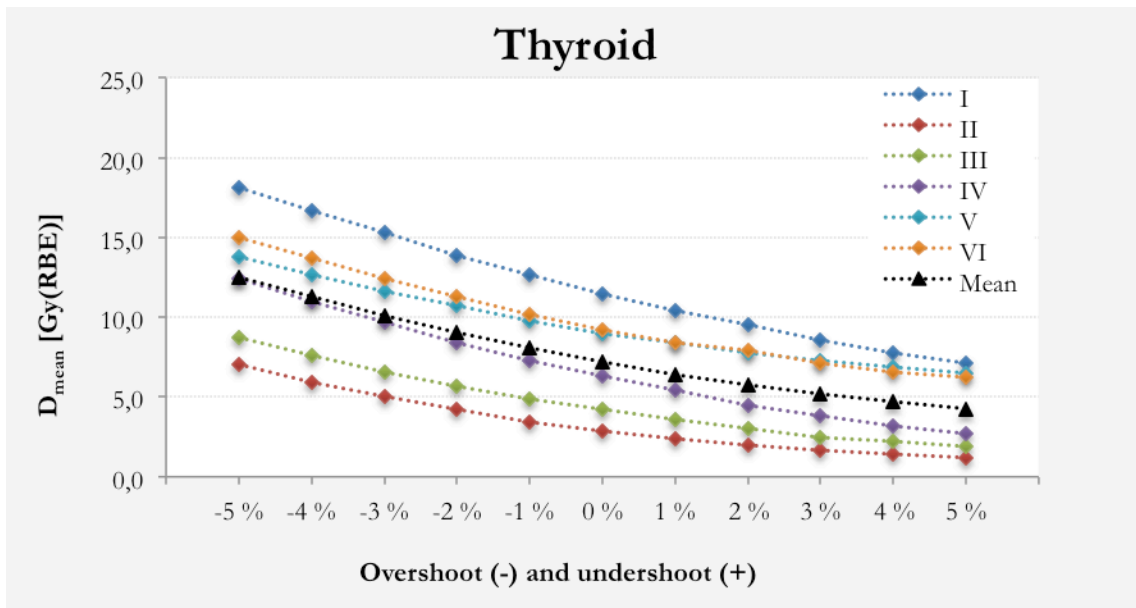
Figure 4-15: The individual results for the D_{mean} following CCEs of ±1% to ±5%. The results for patient I-VI, including the mean values across the patient group are displayed. Zero % CCE corresponds to the reference plans.

4.2.3 Effects of setup errors

In Figure 4-16a-c) the Max-Min dose distribution after the simulation of the setup errors is displayed for patient II. The result from the present calculation is representative for the rest of the patient group. Following setup errors of ±1 to ±5 mm in 1 mm steps in the left and right direction the Max-Min dose differences were calculated, the result of this calculation is displayed in Figure 4-16a) in coronal view. Corresponding calculations were also performed for the setup errors in the ventral and dorsal directions, and for the setup errors in caudal and cranial the directions. The results from these calculations are shown in Figure 4-16b) and Figure 4-16c), both in sagittal view. The dose differences are displayed by the colour bar scale to the right in each image.

The largest Max-Min dose differences following the left and right setup errors, emerged bilaterally along the spine, with dose differences well above the 60% level. Following vertical setup errors, the Max-Min dose differences of more than 40% were mainly seen in the cranium and in the cranial part of the cervical spine. Following cranial and caudal setup errors Max-Min dose differences of more than 40% appeared in the cranial and the caudal part of the patient. The Max-Min dose differences were largest outside the PTV for all setup errors in any directions.
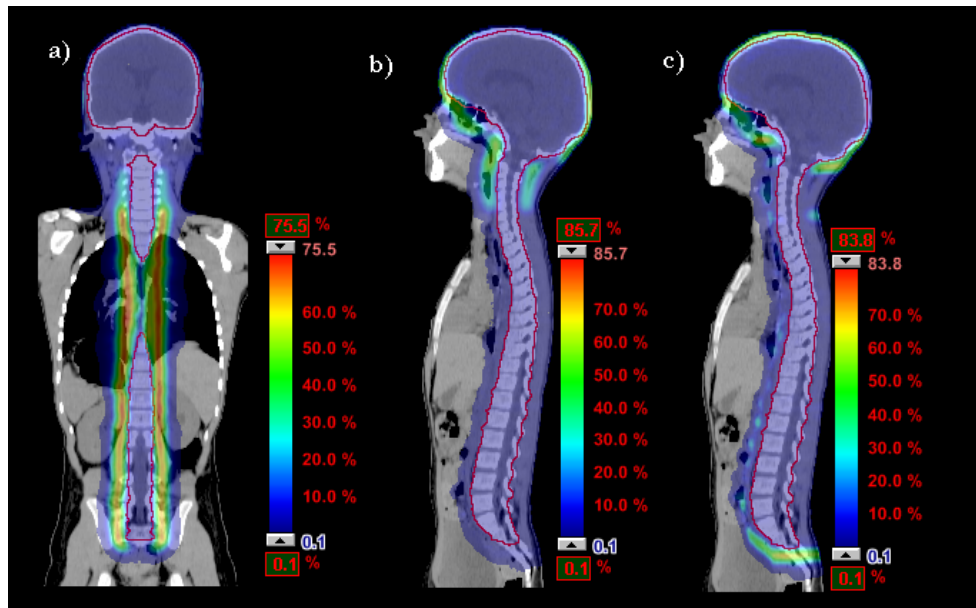
Figure 4-16: The calculated Max-Min dose distribution after setup errors of ± 1 to ± 5 mm in the longitudinal, lateral and vertical direction is presented. Image a) displays the result in the coronal plane after lateral setup errors, image b) and c) displays the result in the sagittal plane after vertical and longitudinal setup errors, respectively.

4.2.3.1 Target volume dose coverage

Figure 4-17a-c) shows the impact of setup errors of 1-5 mm on the 95% dose coverage ($V_{34,2 \text{ Gy (RBE)}}$) for the CTV, the brain volume and the spinal canal. The figure displays the group-averaged results for the $V_{34,2 \text{ Gy (RBE)}}$ (%) after the introduction of setup errors in the caudal and cranial directions (Figure 4-17a)), in the dorsal and ventral directions (Figure 4-17b)) and in the left and right directions (Figure 4-17c)). The magnitude of the shifts are displayed on the x-axis, and the $V_{34,2 \text{ Gy (RBE)}}$ on the y-axis, in relative units. Note that the scale on the y-axis starts at 96%.

In general, setup errors had only minor influence on the $V_{34,2 \text{ Gy (RBE)}}$. Regardless of the magnitude of the errors, the resulting $V_{34,2 \text{ Gy (RBE)}}$ remained > 97% for all the volumes. Some differences between the target volumes could be observed, though. The spinal canal sustained the 95% dose coverage irrespective of any setup error, with the exception of the

5 mm setup error in the cranial and ventral direction. The resulting loss in the 95% dose coverage was nonetheless diminutive with $V_{34,2\ Gy\ (RBE)}= 99,7\%$ and $V_{34,2\ Gy\ (RBE)}= 99,9\%$ due to the cranial and ventral setup errors, respectively.

The $V_{34,2\ Gy\ (RBE)}$ for the brain volume and the CTV exhibited similar tendencies following the caudal and cranial setup errors, and the dorsal and ventral set up errors , while some differences between the two volumes could be observed after the setup errors in the left and right directions. For both volumes the caudal setup errors were of most importance, however with minor reductions in the resulting $V_{34,2\ Gy\ (RBE)}$. The largest consequence was seen in the brain volume, with the 2 mm and 5 mm error reducing the $V_{34,2\ Gy\ (RBE)}$ to 99,6% and 97,2%, respectively.

The setup errors in the left and right directions had an insignificant effect on the $V_{34,2\ Gy\ (RBE)}$ for the brain volume and only a small effect for the CTV. All reductions in $V_{34,2Gy\ (RBE)}$ for the CTV were less than 2 %.
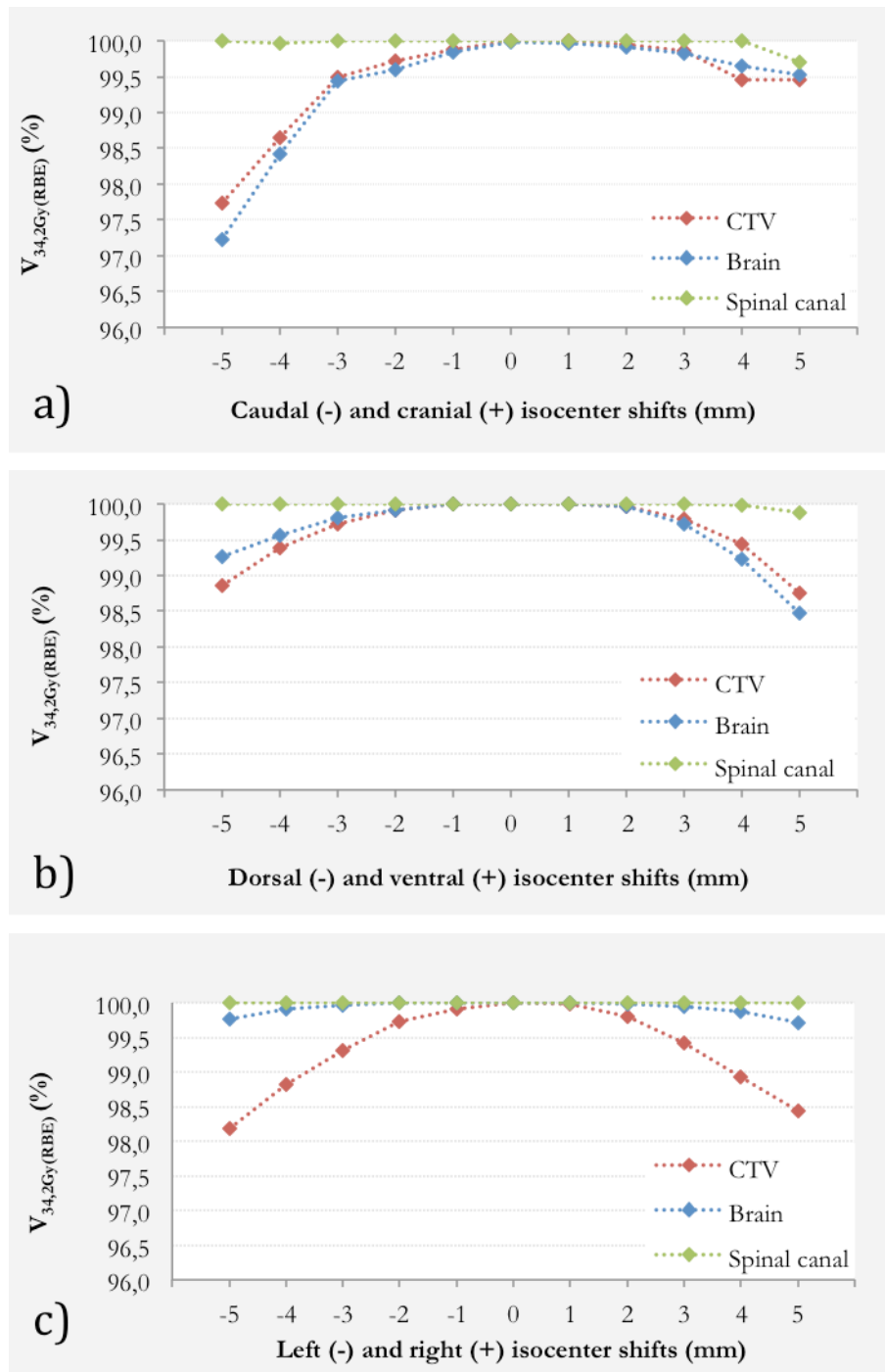
Figure 4-17: The impact of setup errors on the $V_{34,2Gy\ (RBE)}$ for the CTV, the brain and the spinal canal. The group-averaged results are displayed for caudal and cranial setup errors in a), for dorsal and ventral setup errors in b) and for left and right setup errors in c). The magnitude of shifts are displayed on the x-axis and the $V_{34,2Gy\ (RBE)}$ on the y-axis in relative units. The zero shifts represent the values from the reference plans. Note that the scale on the y-axis starts at 96%.

In Figure 4-18a) the dose distribution is displayed for the reference plan. Figure 4-18b) displays the dose distribution after a 5 mm lateral setup error is introduced. The images show the CTV (marked with the red line) and the spinal canal (marked with the cyan line) in the mediastinum level in the transversal view. The yellow arrows in the figures indicate the beam direction.

Two main effects could be observed as a result of the setup error. Firstly, the 5 mm lateral setup error resulted in a shift of the dose distribution in the same direction as the setup error was applied. The consequence was a loss in the CTV dose coverage as indicated by the red arrow in imaged 4-18b). The 95% dose coverage to the spinal canal was however sustained. Secondly, a significant disturbance of the dose distribution could be observed. The setup error clearly caused an overall increase of the lung doses, as displayed by the 80%-105% isodose lines. The 80%-105% isodose became significantly extended distally, as indicated by the pink arrow in the figure.
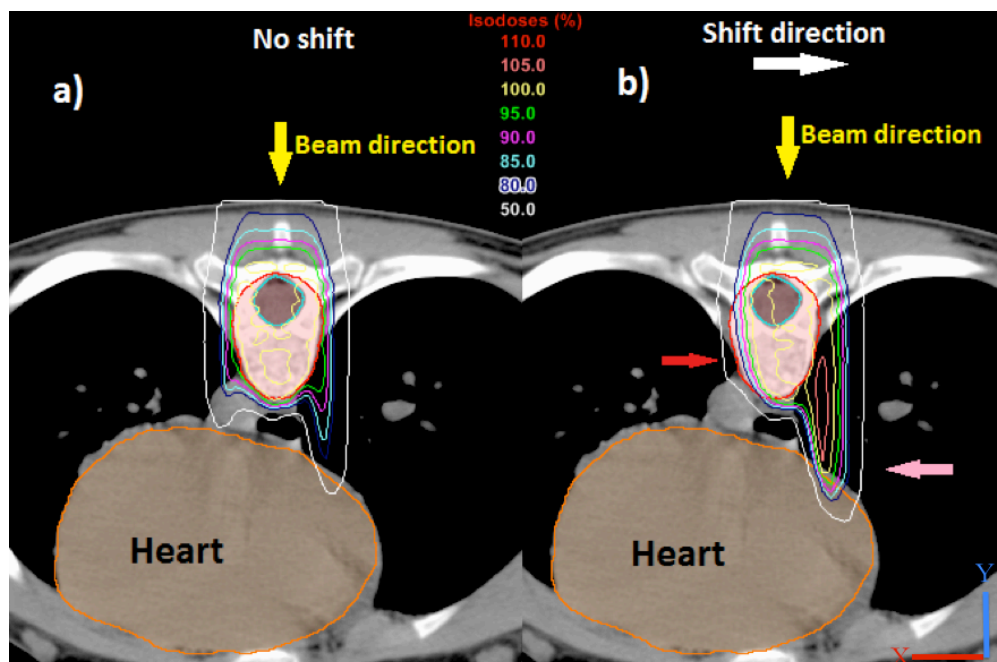
Figure 4-18: The dose distribution is displayed by isodose lines for the plan without an applied setup error in image a). The dose distribution after a 5 mm lateral setup error (indicated by the white arrow) is displayed in image b). The beam direction is indicated by the yellow arrow. The red arrow indicates the loss in the target volume dose coverage. The pink arrow indicates the error influenced high dose area.

The Figure 4-19 shows the 95% -107% dose distribution in transversal view for the reference plan in image 4-19a), the 95%-107% dose distribution after a setup error of 5 mm in the dorsal direction in image 4-19b), and after a setup error of 5 mm in the ventral direction in image 4-19c).

An almost contradictory effect could be observed when comparing the resulting dose distribution of the ventral and the dorsal setup errors. Following the dorsal setup error, hot spots emerged in the cranium at the dorsal part of the skull, as indicated by the red arrow. In the same area the setup error in the ventral direction resulted a loss in the 95% dose coverage, this indicated by the blue arrow. In the ventral part of the brain, between the eyes, the similar tendency could be seen, but now instead with the hot spots and the cold spots stemming from the ventral and dorsal setup errors, respectively. In the image with the applied ventral shift, a band of hot spots is visible at the left side of the brain. The same can also be observed at the right side of the brain, here to a lesser extent. The dose perturbations triggered by the setup errors appeared for the most part in the areas where the dose distribution in the reference plan was most inhomogeneous.
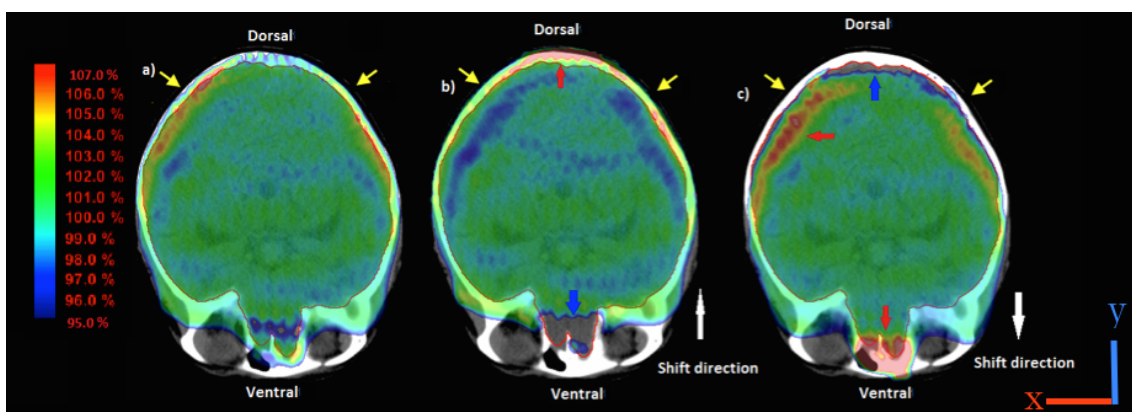
Figure 4-19: The 95%-107% dose distribution displayed in transversal view. The dose distribution from the reference treatment plan is displayed in image a). The dose distribution from the plan with the imposed setup error of 5 mm in the dorsal and the ventral directions are displayed in image b) and in image c) respectively. The blue and red arrows indicate areas with cold spots and hot spots, respectively.

The 95% -107% dose distribution following the introduction of a 5 mm setup error in the caudal and cranial directions is displayed in sagittal view in Figure 4-20b) and 4-20c), respectively. The corresponding dose distribution for the reference plan is displayed in Figure 4-20a). The perturbations of the dose distribution stemming from the setup errors in the caudal and cranial directions emerged for the most part in the cranial portion of the brain, and in the area related to the skull base. As also demonstrated for the dorsal and the ventral setup error, virtually opposite trends could be observed. The cranial setup error induced a formation of hot spots in the cranium, indicated by the red arrow in image 4-20c). The cranial setup error also reduced the 95% dose coverage in the skull base area. The resulting cold spot is indicated by the blue arrow in the image. The caudal setup error, however, resulted in the appearance of cold spots in the cranial part of the brain, this indicated by the blue arrow in image 4-20b), and of hot spots in the skull base area, this indicated by the blue arrow in the image.
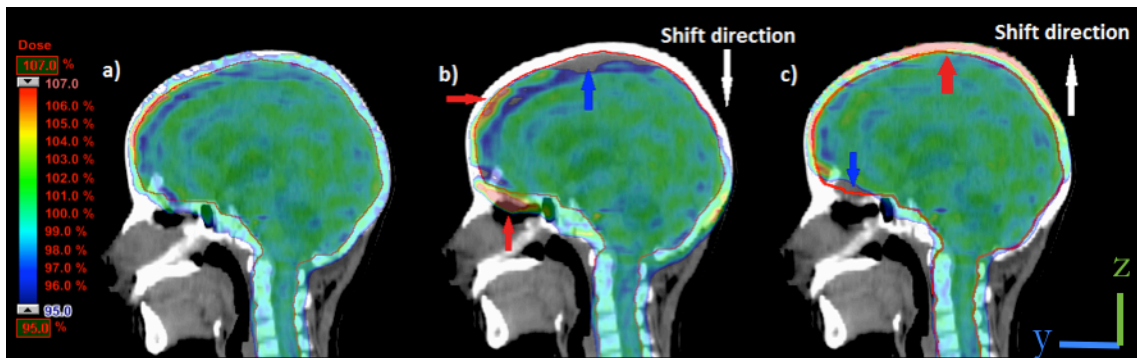

Figure 4-20: The 95%-107% dose distribution is displayed in sagittal view. The dose distribution from the reference treatment plan is displayed in image a). The dose distribution from the plan with the imposed setup error of 5 mm in the caudal and the cranial directions are displayed in image b) and in image c), respectively. The blue and red arrows indicate areas with cold spots and hot spots, respectively.

4.2.3.2 Doses to organs at risk

In the following, the resulting D_{mean} and $V_{5Gy\,(RBE)}$ from the simulations of the 1 mm to 5 mm setup errors are presented. Individual results and mean results across the patient group (so-called group-averaged results) are presented for the heart, the thyroid, the kidneys and the eyes in Figures 4-21 to 4-29.

The doses to the heart

The Figure 4-21 displays the group-averaged results for the $V_{5Gy\,(RBE)}$ for the heart following setup errors of 1-5 mm. The heart doses were mainly affected by the setup errors in the lateral directions, with a continuous increase or decrease in $V_{5Gy\,(RBE)}$. The $V_{5Gy\,(RBE)}$ increased from 4,2% in the reference plan to 5,0% and 6,8% after 2 mm and 5 mm setup errors in the left direction, respectively. In contrast, the corresponding setup errors in the right direction caused a slight reduction of the $V_{5Gy\,(RBE)}$ to 3,5% and 3%, respectively. Furthermore, the effects of the setup errors in the other directions were insignificant, no noticeable increase or decrease in $V_{5Gy\,(RBE)}$ could be observed.
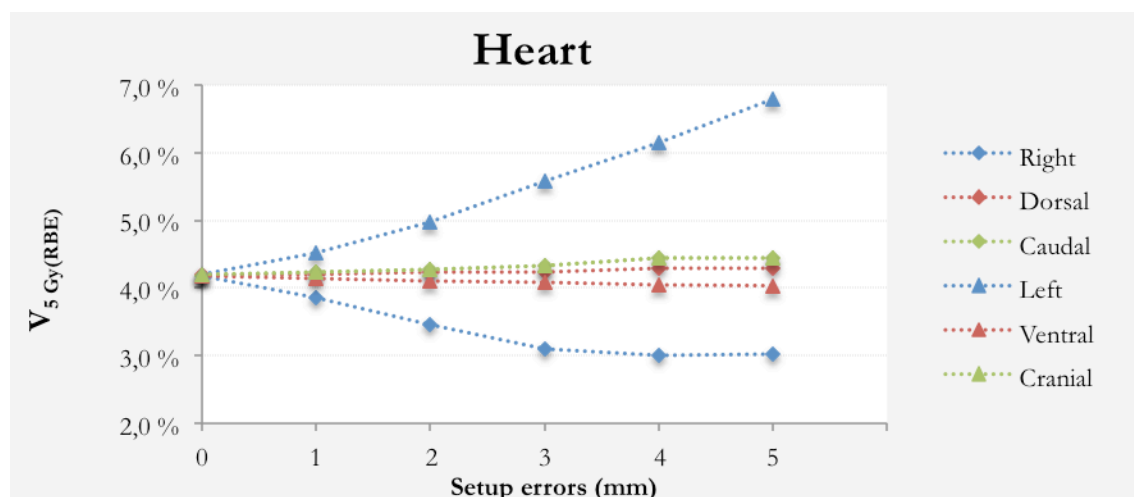

Figure 4-21: The resulting group-averaged $V_{5Gy\,(RBE)}$ for the heart following setup errors of 1 mm to 5 mm are displayed. The setup errors are displayed on the x-axis. The D_{mean} is displayed on the y-axis. The zero setup error represents the value from the reference plan.

Figure 4-22 displays the individual results for the D_{mean} for the heart following setup errors of 1-5 mm. The figure displays the result for patients I-VI, including the mean values for the patient group. Considerable variations in the D_{mean} could be observed between the individual patients, however, the effect of the setup errors where consistent with a small increase in D_{mean} stemming from the setup errors in the left direction. For the patient with the overall highest doses, patient V, the D_{mean} increased from 1,2 Gy (RBE) in the reference plant to 1,3 Gy (RBE) and 1,9 Gy (RBE) after the introduction of 2 mm and 5 mm setup errors in the left direction, respectively. Similar, for the patient with the lowest doses, patient VI, the D_{mean} increased from 0,3 Gy (RBE) in the reference plan to 0,4 Gy (RBE) and 0,6 Gy (RBE), respectively.
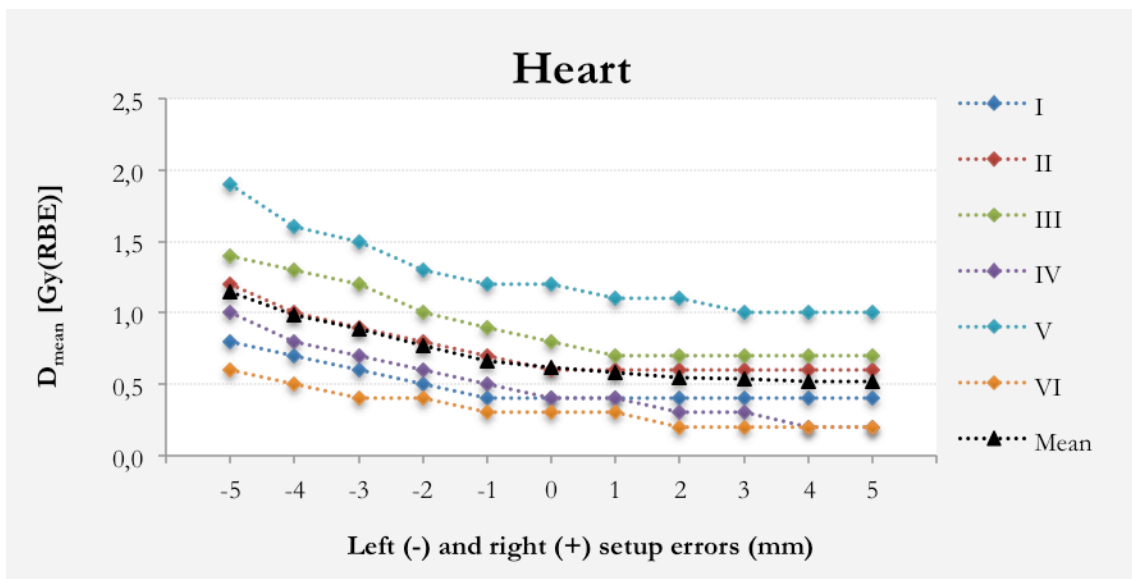
Figure 4-22: The individual results for the D_{mean} for the heart following setup errors of 1-5 mm are displayed. The figure displays the result for patient I-VI including the mean values across the patient group. The setup errors are displayed on the x-axis and the D_{mean} on the y-axis. The zero shifts correspond to the reference plan.

The doses to the kidneys

The Figure 4-23 displays the group-averaged results for the $V_{5Gy (RBE)}$ for the right kidney following introduction of setup errors of 1-5 mm. As can be seen from this figure, only lateral setup errors influenced the doses to the kidneys. A rapid expansion in $V_{5Gy (RBE)}$ could be observed as a consequence of increasing setup errors in the right direction, from 13% in

the reference plan to 19% and 29% after the introduction of 2 mm and 5 mm setup errors, respectively. The opposite could be observed following the setup errors in the left direction. Here the corresponding results were 8% and 3%. The plot also illustrates that the doses to the kidneys are virtually unaffected by shifts in the longitudinal and vertical directions.
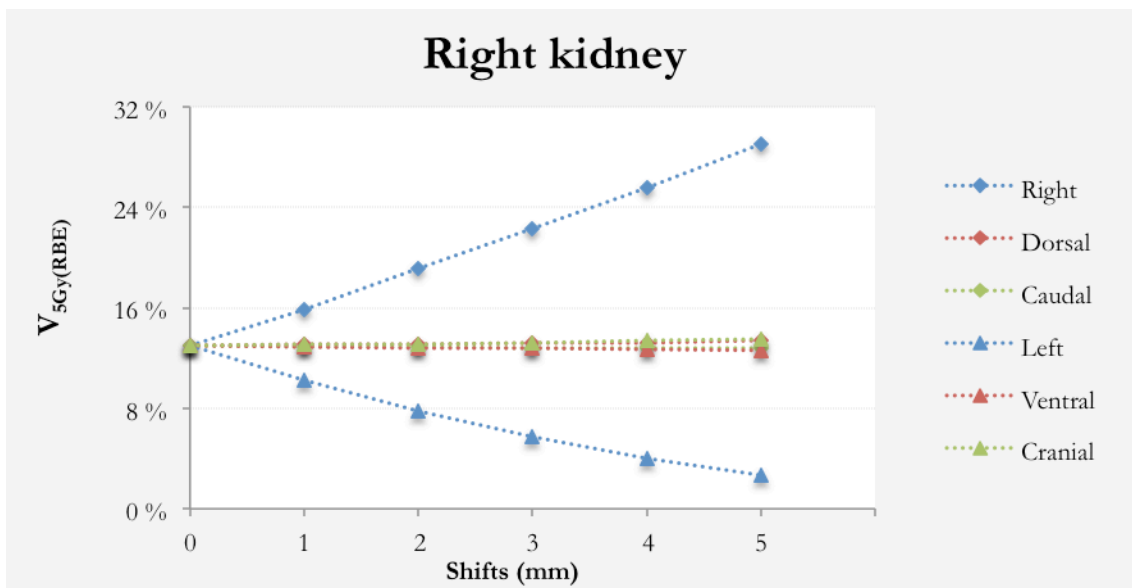
Figure 4-23: The resulting group-averaged $V_{5Gy\,(RBE)}$ for the right kidney following setup errors of 1 mm to 5 mm are displayed. The setup errors are displayed on the x-axis. The $V_{5Gy\,(RBE)}$ is displayed on the y-axis. The zero setup error represents the value from the reference plan.

The Figure 4-24 displays the individual results for the D_{mean} for the left kidney following the introduction of setup errors of 1-5 mm. The figure displays the result for patient I-VI, including the mean values across the patient group. Setup errors in the direction towards the left kidney had a dose-increasing effect. The opposite effect was seen when applying setup errors directed away from the left kidney, to a lesser extent though. The results for 4 of the 6 patients showed similar behaviour with an approximately equal increase or reduction in the D_{mean}. As for the heart, the result for patient V displayed a more rapid increase in D_{mean} than the rest. The D_{mean} changed from 2,5 Gy (RBE) in the reference plant

to 3,9 Gy (RBE) and 6,5 Gy (RBE) after 2 mm and 5 mm setup errors toward the left, respectively. For the patient displaying the overall lowest doses, patient II, the D_{mean} changed from 1,4 Gy (RBE) to 2,0 Gy (RBE) and 3,3 Gy (RBE), respectively.
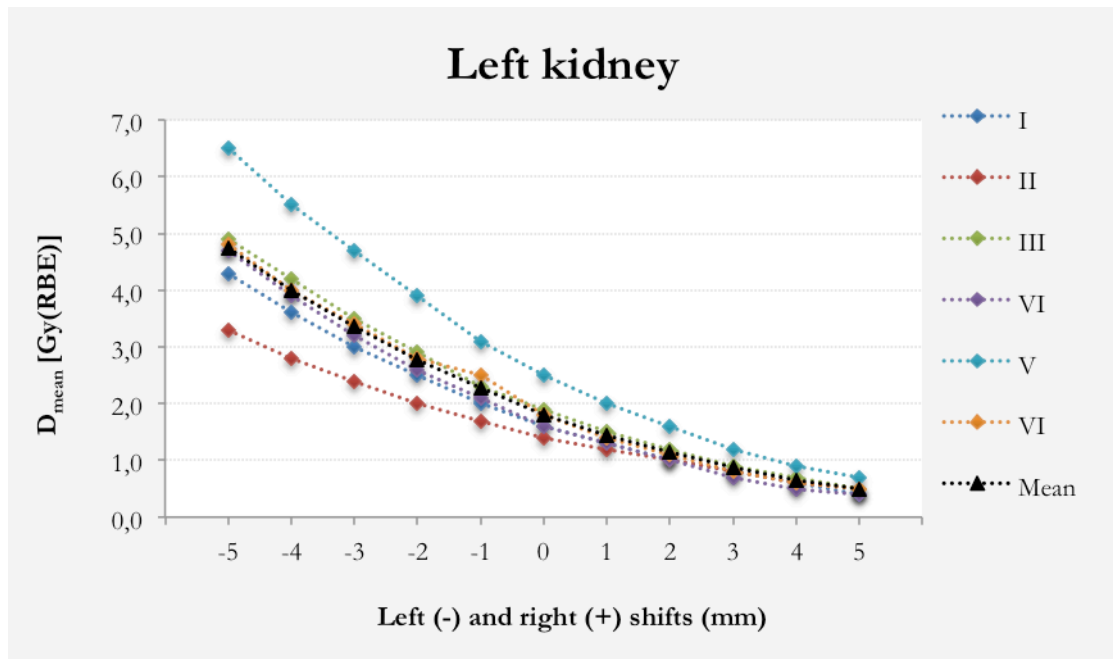
Figure 4-24: The individual results for the D_{mean} for the left kidney following the introduction of setup errors of 1-5 mm are displayed. The figure displays the result for patient I-VI including the mean values across the patient group. The setup errors are displayed on the x-axis and the D_{mean} on the y-axis. The zero shifts correspond to the reference plan.

The doses to the thyroid

The Figure 4-25 displays the group-averaged results for the D_{mean} for the thyroid following the introduction of setup errors of 1-5 mm. The thyroid doses were mainly affected by the setup errors in the ventral and dorsal direction. Compared to the reference plan the ventral setup errors appeared as the most important dose-increasing parameter, with e.g. the D_{mean} changing from 7,2 Gy (RBE) in the reference plan to 8,2 Gy (RBE) and 9,7 Gy (RBE) in the plans recalculated with the 2 mm and 5 mm ventral setup errors, respectively. A somewhat more moderate increase in dose was seen as a consequence of the cranial setup errors. The opposite tendency was found following the dorsal and caudal setup errors, with

a steady diminishing D_{mean}. Furthermore, the right and the left shifts did not alter the D_{mean} significantly.
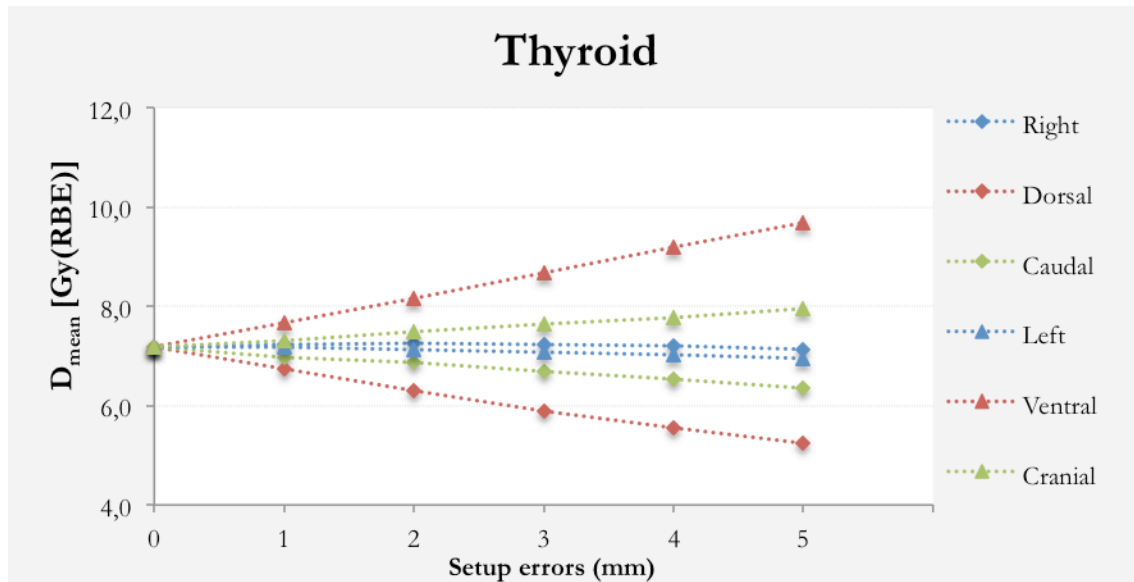
Figure 4-25: The resulting group-averaged D_{mean} for the thyroid following setup errors of 1 mm to 5 mm. The setup errors are displayed on the x-axis. The D_{mean} is displayed on the y-axis. The 0 setup error represents the value from the reference plan.

The Figure 4-26 displays the individual results for the $V_{5Gy\,(RBE)}$ for the thyroid following the introduction of setup errors of 1-5 mm. The figure displays the result for patient I-VI, including the mean values for the patient group. Large variation could be observed from patient to patients, both regarding the doses in the reference plans, which range from 16% for patient II to 82% for patient VI, but also to which extent the setup errors affected the doses.

Most consistent was the results for patient II with the $V_{5Gy\,(RBE)}$ changing from 16% in the reference plan to 17,2% and 20,4% following the setup errors of 2 mm and 5 mm in the ventral direction, respectively. The results for patient V and patient VI exhibited a different pattern than the results for the other patients with a more rapid dose-increase seen for these two. For patient V, the $V_{5Gy\,(RBE)}$ increased from 70,9% in the reference plan to 80,5%

and 89,8% in the plans with the 2 mm and 5 mm setup errors, respectively. The corresponding results for patient VI yielded a fluctuation in $V_{5Gy\,(RBE)}$ from 82,4% to 95,3% and 99,7%, respectively.
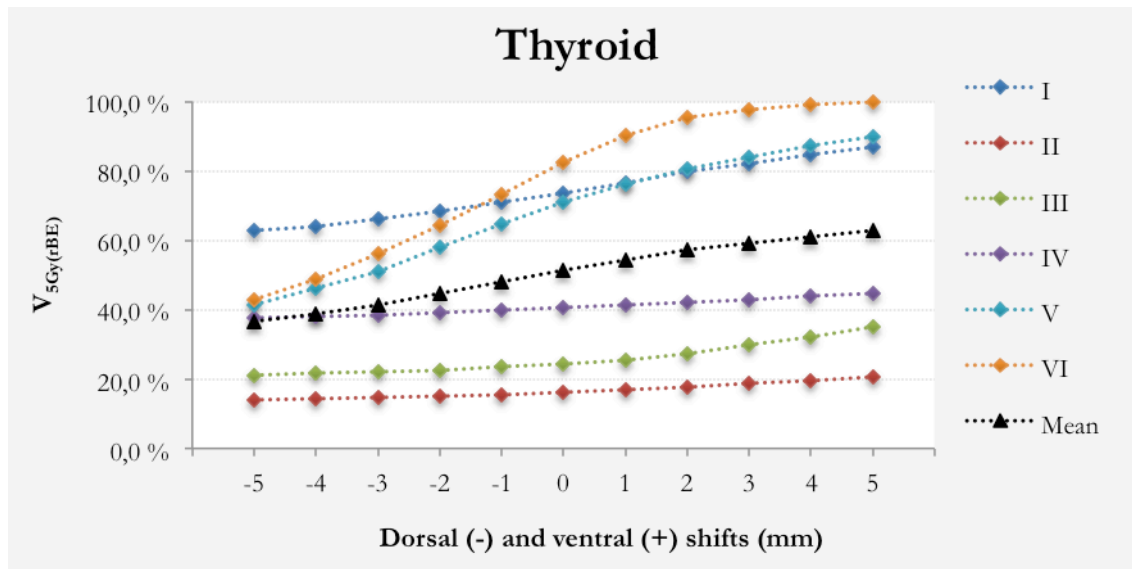
Figure 4-26: The individual results for the $V_{5\,Gy\,(RBE)}$ for the thyroid following setup errors of 1-5 mm are displayed. The figure displays the result for patient I-VI including the mean values across the patient group. The setup errors are displayed on the x-axis and the D_{mean} is displayed on the y-axis. The zero shifts correspond to the reference plan.

The doses to the eyes

The Figure 4-27 displays the group-averaged results for the D_{mean} for the right eye following the introduction of setup errors from 1 mm to 5 mm. The setup errors in the caudal, cranial, dorsal and ventral directions were most important when it came to the consequences for the eye doses. Following increasingly larger shifts in both the caudal and ventral directions, a continuous increase in the D_{mean} was found. The dose increase was slightly larger as a consequence of caudal shifts. The dorsal and cranial shifts caused an almost equal reduction in the D_{mean}. Furthermore, the lateral shifts only had a negligible impact on eye doses.
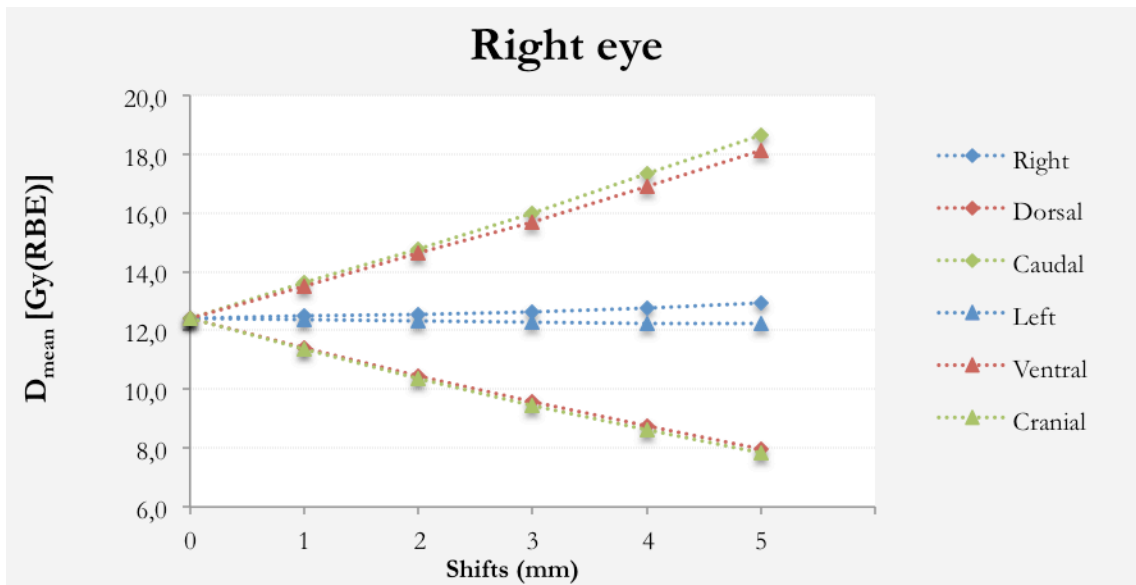
Figure 4-27: The resulting group-averaged D_{mean} for the right eye following the introduction of setup errors from1 mm to 5 mm. The setup errors are displayed on the x-axis. The D_{mean} is displayed on the y-axis. The 0 setup error represents the value from the reference plan.

Figure 4-28 displays the individual results for the $V_{5Gy(RBE}$ for the left kidney following the introduction of setup errors from 1mm to5 mm. The figure displays the result for patient I-VI including the mean values across the patient group.

It was found that almost identical patterns could be seen for all the patients. The group-averaged $V_{5Gy(RBE}$, represented by the black triangles, changed from 67,9% in the reference plan to 74,9% and 84% in the plans with the 2 mm and 5 mm setup errors, respectively. Following the cranial setup errors of the same magnitude the $V_{5Gy(RBE}$ changed to 60,2% and 48,2%, respectively. For the results for patient VI, a small deviation in from the rest of the patients could be observed in the situation with the cranial shifts, with a slightly dampened reduction in $V_{5Gy\ (RBE)}$.
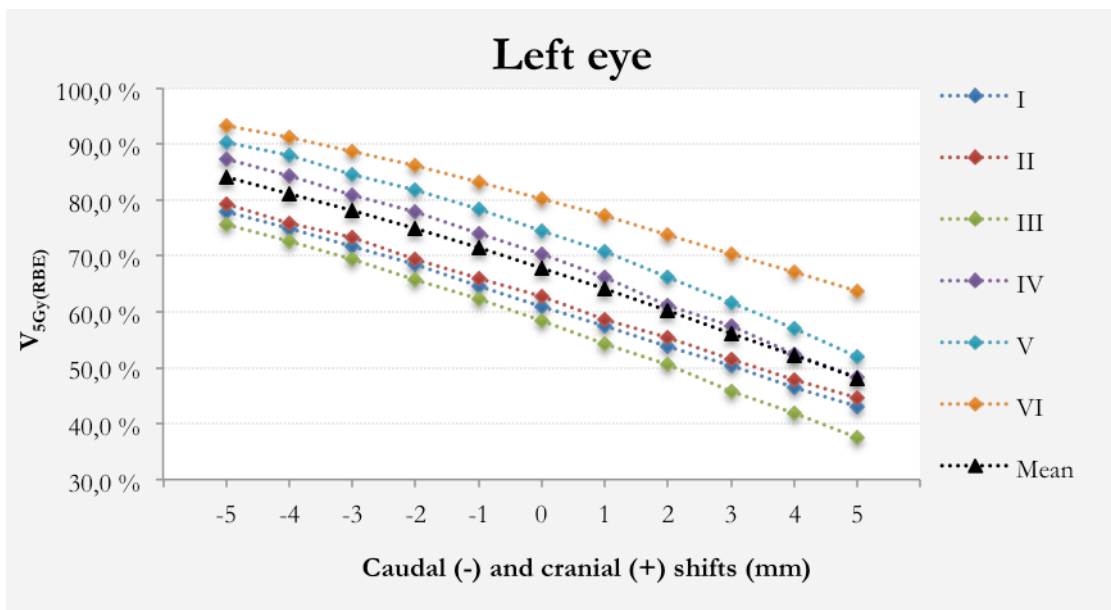
Figure 4-28: The individual results for the $V_{5\,Gy\,(RBE)}$ for the left eye following the introduction of setup errors from 1-5 mm are displayed. The figure displays the result for patient I-VI including the mean values across the patient group. The setup errors are displayed on the x-axis and the D_{mean} on the y-axis. The zero shifts correspond to the reference plan.

Figure 4-29 displays the individual results for the D_{mean} for the right eye following the introduction of setup errors from 1-5 mm. The figure displays the result for patient I-VI including the mean values for the patient group. The results reveal that the dosimetric effects of the dorsal and ventral setup errors were consistent across the patient group. The group-averaged D_{mean}, represented by the black triangles, changed from 12,4 Gy (RBE) in the reference plan to 14,8 Gy (RBE) and 18,7 Gy (RBE) after the introduction of 2 mm and 5 mm shifts, respectively. Following the dorsal setup errors of the similar magnitude the D_{mean} changed to 10,5 Gy (RBE) and 8,0 Gy (RBE), respectively.
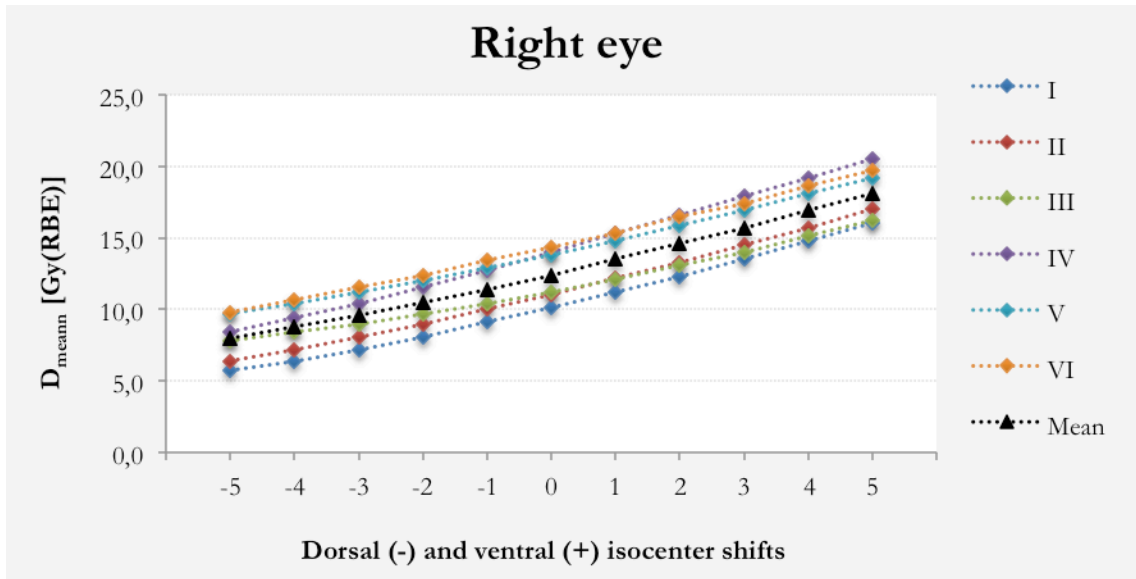
Figure 4-29: The individual results for the D_{mean} for the right eye following the introduction of setup errors from 1-5 mm are displayed. The figure displays the result for patient I-VI including the mean values across the patient group. The setup errors are displayed on the x-axis and the D_{mean} on the y-axis. The zero shifts correspond to the reference plan.

5 DISCUSSION

5.1 The water phantom study

To demonstrate how density changes in a proton beam path would affect the proton range and depth dose distribution, a treatment planning study was performed on water phantoms designed in the treatment planning system. Systematic insertion of volumes assigned with a HU value of 1000 (representing bone) and volumes assigned with a HU value of – 1000 (representing air) was performed and the corresponding changes in the proton range and the target volume dose coverage were studied.

By analysing the central beam axis depth doseprofiles, it was demonstrated that the main effect of introducing density changes in the beam path was an alteration of the beam penetration depth, with somewhat different consequence depending on whether the inhomogeneity was induced by volumes of bone or air. Depending on the density of the inserted material, the SOBP dose plateau was shifted closer to (bone) or further away (air) from the source respectively. The effect was significantly more pronounced when inserting air than bone, with the range, represented by the distal position of the d90%, being changed, almost linearly, with a factor of $\frac{dR}{dx} =$ +0,94 for air and with a factor of $\frac{dR}{dx} =$ -0,48 for bone, both obtained from a polynomial fit function applied on the respective data points. The significantly larger change in range, that was observed when inserting volumes of air compared to volumes of bone, is due to the differences in the densities in the two applied materials, and consequently the differences in their corresponding water equivalent density. In a scenario like those investigated in this study, where water is entirely replaced with a homogenous material of a different density, the change in range is directly related to the water equivalent density of the interposed material. This is expressed by the formula $\Delta R = t - t\rho_{eq}$ where t is the physical thickness in units of length, and ρ_{eq} is the water equivalent density of the replacing material (19) (s 101).

The distal slope of the depth dose profiles was unperturbed by the change in density which was introduced proximal to the target volume, this demonstrated by the unaltered distal dose fall-off (d80%-d20%). However, the slope of the curves in the entrance region – proximal to the SOBP plateau– was altered, reflecting a change of the dose deposition in this region. The change depended both on the variation in density (bone versus air versus water) and on the position in depth for the inserted air and bone volumes. According to

the Bethe-Bloch formula, the energy loss a proton experience when traversing a material is proportional to the density of the material (17). Bone, being a more dense material than water, consequently increases the energy loss for protons per unit of traversed matter relative to the energy loss for protons traversing water, when all other conditions and parameters are unchanged. Air is a less dense material than water, and accordingly this in turn has the consequence a decrease in the energy loss per unit of traversed air relative to water. Thus, when the proton beam hits the bone, the energy deposition increases in the region covered by bone, followed by a decrease when the proton beam is entering water again. Similarly, dose deposition decreases while the proton beam traverses the air compared to water, and increases again in the region with water.

In the second part of the water phantom study the aim was to investigate how a geometric misalignment of a target volume with respect to the beam, would affect the proton dose distribution. The situation was investigated in both the homogenous and the heterogeneous phantoms and simulated by introducing isocenter shifts parallel and orthogonal to the beam direction. It was found that isocenter shifts parallel to the beam direction (along the y-axis) had no major impact on the dose distribution for both homogeneous and heterogeneous phantoms. Since, in this situation, the density along the particle path was not changed relative to the situation with no shifts, the water equivalent density remained the same and the particle range was not affected (1). Thus the impact on the dose distribution here was insignificant. The loss in the 95% target coverage found in phantom A_{water} after the isocenter shifts orthogonal to the beam direction, was solely caused by a spatial shift of the dose distribution towards the shift directions. This resulted in the target volume being partly shifted "out" of the 95 % dose level at the opposite side. An additional disturbance in the dose distributions were seen in the heterogeneous phantoms, with decreased homogeneity due to the appearance of hot-and cold spots inside the target volume, as well a large cold spots at the distal border of the target volume. Two factors contribute to the observed effects. Firstly, and the most important factor, was that the isocenter shift was perpendicular to the beam direction, thus resulting in a misalignment of the heterogeneity in the centre of the phantom relative to the beam. The shift caused the proton beam to traverse through a material with different density, hence altering the initially estimated particle range and the corresponding dose distribution.

The second effect, described by Goitein (52) and referred to in the ICRU report 78 (19, p. 102), is known as the edge scattering effect. The edge scattering occurs in situations where the media irradiated is partly intersected with a material of different density. The effect is a result of the different amount of multiple scattering processes that occurs in the involved materials. In the border region between the two materials, the scattering processes that occurs in the most dense material will scatter the protons laterally, thus into the less dense material. This results in hot spots to occur at the least dense side. Consequently, because more protons are scattered laterally away from the denser region, cold-spots occur on the side with highest density. Since air hardly scatters protons at all, the edge scattering effect was significantly more pronounced in phantom C_{air}, than in phantom B_{bone}, given that the density difference between water and air is larger than the density difference between water and bone. The edge scattering effect could also be observed in the reference plans in phantom B_{bone} and C_{air}.

5.2   Robustness analysis of craniospinal treatment plans

Craniospinal treatment plans were created with the IMPT technique on 6 anonymous 3D CT image data sets of pediatric patients, which have previously had been treated with conventional radiation therapy using a combination of photon and electron treatment fields. The IMPT treatment plans were used as reference plans in the investigation of the dosimetric effect of calibration curve errors and setup errors.

All of the craniospinal reference treatment plans had PTV dose coverage of high conformity and homogeneity, and satisfied in general the plan evaluation criteria stated in this study. Excellent dose conformity and homogeneity in craniospinal proton treatment plans have been previously demonstrated for both the IMPT technique (47) and the passive scattering technique (6, 7, 49) and thus confirms the present findings in this study.

Dose sparing was achieved with respect to the normal tissue distal to the target volume and for the OAR situated at a certain distance from the PTV. This was expected due to the advantageous physical characteristics of the proton beam, and is associated with the rapid dose fall-off behind the Bragg Peak plateau, which, in turn, is one of the main rationales for using protons for the craniospinal irradiation (6, 7). The doses to the OARs in proximity of the target volume did, not surprisingly, receive higher doses, with the highest

doses provided to the eyes and the thyroid. The results from the evaluation of the doses to the heart, the lungs and the kidneys in the reference treatment plans, agreed reasonable well with the findings from other studies, in which it was applied age specific target volumes and similar beam arrangements. The doses to the thyroid, however, were generally higher in this study than reported elsewhere (6, 7, 49), and varied considerably across the patient group with the D_{mean} ranging from 8% to 31,9% of the prescribed dose. As a comparison, Giebeler et al. reported D_{mean} to the thyroid of 1.5 % of the prescribed dose in their study (49). The differences between the study from Giebeler et al and this study can be explained by the fact that in this study the thyroid was not assigned with dose-volume objectives during the optimization process, and hence not specifically constrained in terms of the dose level. In the study of Giebeler et al, however, the thyroid was assigned a constraint that imposed the 5 % isodose line not to cross the medial boundary of the thyroid contour, this achieved by thickening the compensator in that particular area. Furthermore, due to slightly different beam arrangements, the thyroid in this study was covered by the lateral oblique cranial fields, as opposed to in the study of Giebeler et al., where the thyroid was situated in the area covered by the upper spinal field, shielded by both the lateral and the distal field boundary and hence benefitted from the favourable sharp dose gradient behind the Bragg Peak dose plateau.

Another noteworthy observation from this study is the considerable spread in the doses to the OAR across the patient group, as opposed to the small spread in dose for the target volume doses. This can be explained by the large span in size of the defined volume.

The analysis of the effects of the calibration curve errors revealed no substantial amendments in the overall doses to the target volumes. The dose alterations in the spinal canal were in general negligible, neither undershoot nor overshoot affected the 95% dose coverage. This was not unexpected as all the treatment plans were created with an age-specific CTV, thus encompassing the spinal canal with a large "margin" distally. Furthermore, a 5 mm margin was added at the proximal end of the spinal canal when designing the PTV. A more surprising observation was that there was no degradation of the 95% dose coverage of the CTV volume distal in the vertebral area, as one would expect when introducing range errors. The observed loss in the 95% CTV dose coverage appeared exclusively in the brain area. The reference plans were however created including a distal field specific range margin of 2 mm, this defined relative to the PTV. Thus the 95%

isodose line conformed around the distal part of the vertebra at a distance of approximately 1-2 mm. The applied margin was sufficient in maintaining the 95% dose coverage at this area, regardless of the imposed range errors of 1% to 5%.

The overshoot and undershoot exhibited somewhat different effects with respect to the doses to the brain. The overshoot caused a small, but systematic decrease in the overall doses, however no degradation of the 95% dose coverage was observed. Compared to the reference plan, undershoot resulted in an increased dose inhomogeneity in the brain, this was also the case for the overshoot, however to a much smaller extent. Following the imposed calibration curve error of +5%, an area of loss in the 95% dose coverage emerged along the inside of the cranium, particularly towards the lateral sides (Figure 4-14c)). This observed effect typically arises from a situation where the HU values from the planning CT are underestimated during the calculation of the proton beam range in the patient (42). The subsequent consequence is that the planned positions of the Bragg Peaks in depth are abridged. Thus, the loss in the 95% dose coverage observed at the left side of the brain in Figure 4-14c), originated from the shortened proton range of the right lateral oblique beam, and conversely, the band of cold spots observed at the right side, derived from the shortened proton range of the left lateral oblique beam.

The OARs included in the dosimetric evaluations in this study were the heart, the eyes, the kidneys and the thyroid. It was found that only tissues distal to, and in close proximity to the target volume were affected by the calibration curve error. Further, the overshoot and undershoot induced opposing effects. The overshoot is stemming from the overestimation of the HU values from the planning CT used for the calculation of the proton beam range in the patient (42). This result in the planned positions of the Bragg Peaks in depth being prolonged and accordingly the high dose area is moved distally. From the analysis of the doses to the OARs it was demonstrated that for the thyroid the result of this positional change in the high dose area, was a substantial increase in the doses. The result revealed that a 3% overshoot lead to a mean increase of the D_{mean} in the order of approximately 47%. This is an important finding, considering that the radiation induced thyroid dysfunctions following craniospinal irradiation in pediatric patients, are well documented (53, 54).

In this study the dosimetric effect of calibration curve errors of $\pm 1\%$ to $\pm 5\%$ was evaluated. However, the range error arising from the planning CT is considered to be in the order of 3% to 5%, and common values applied in the calculation of uncertainty margins in clinical practice, ranges from 2,5% to 3,5% (40). The calibration curve is typically generated by the stoichiometric method, previously described in 2.4.1, which provides a good estimation of the proton stopping power. Another method, referred to as the direct-fit method, utilizes measurements of the test materials in both the CT scanner and in a proton beam when generating the calibration curve. By making image- and site-specific calibration curves based on the direct-fit method, the range uncertainty arising from the planning CT can be reduced to $\pm 1\%$ to $\pm 2\%$ of the range (36, p. 429).

The uncertainty in the conversion from HU values to proton stopping power relations derives from the different mechanism of energy loss experienced by photons and protons traversing a material. The proton stopping power values depends on the physical density, chemical composition and the mean excitation energy (denoted I) of the traversed material. The HU values are directly derived from the photon linear attenuations coefficients and the HU values are depending on the parameters applied during the CT acquisition. Hence, there is no simple one-to-one relationship between the proton stopping power and the HU values (33). Considerable efforts are currently being made in the development of a proton CT, which possibly could reduce the range uncertainty to less than $\pm 1\%$. A proton CT utilizes the proton beam itself in the image acquisition. By irradiating the patient with low-intensity proton beams of high energy (330 MeV), and subsequently measure the position, direction and energy loss of each departing proton, the volumetric distribution of the relative stopping power of the protons can be reconstructed. The technique is intended to be used both in treatment planning and for verification of proton range prior to treatment (55).

The analysis from this present study showed that the setup errors had negligible impact on the doses to the spinal canal. Further, only moderate reductions in the 95% dose coverage could be observed for the CTV and the brain. Small areas of underdosage were seen, but for both the brain and the CTV the $V_{95\%}$ was > 97%, this was found irrespective of any setup errors.

The underdosage following the induced lateral setup error appeared exclusively at the edge of the CTV in the vertebral area, as demonstrated in Figure 4-18b), and was caused by a rigid shift of the dose distribution. Thus, a lateral expansion of the irradiated area with e.g. an additional CTV-PTV margin would eliminate the present loss in 95% dose coverage. As previously also demonstrated in the water phantom simulations (Figure 4.6), the shifting of the patient perpendicular to the beam resulted in some additional dose deteriorations. The proton range in the patient is determined by the diverse tissue along the beam path. The lower density conditions in the lungs, compared to the density conditions in the spine, resulted in the edge scattering effect described above, this again resulting in an increase in the dose in the lung area. Furthermore, the proton range was prolonged and hence the position of the Bragg peaks. As a result the energy deposition was moved distally in the patient. This latter effect explains the increased heart doses, which was observed following the setup errors in the left directions.

It has been revealed in previous studies that complex tissue heterogeneities, such as the bone-tissue-air relations in the head, induce both large dose perturbations due to multiple coulomb scattering, which result in a substantial less steep slope of the distal fall-off of the Bragg Peaks, and an alteration of the proton range (56, 57). In the current study this effect was demonstrated by the increased amount of hot spots and cold spots, which were present, especially in the skull basis area, both in the reference treatment plans, and in plans with the imposed setup- and calibration curve errors (Figure 4-12, Figure 4-19 and Figure 4-20).

The analysis of the dosimetric effect of the setup errors on the OARs yielded individual patient results with a reasonable consistency between the patients, despite the initial quite large spread of the dosimetric values. However, some differences were observed regarding the sensitivity to the imposed setup errors. This was mainly related to the size of the volumes of the OAR.

The scenarios investigated in this study are mimicking situations that normally will occur in the clinical situations during radiation treatment with protons. Similar errors and misalignments of a proton beam as e.g. investigated with the water phantoms, can in a clinical situation be caused by anatomical changes in the patient, like for instance the occurrence of air pockets in the intestines, filling of air cavities in the head and neck area or

geometric deviations causing a bony structure to be moved into or out of, or move relative to the beam, amongst other. The obtained results clearly illustrate the challenge of how to manage such uncertainties during proton therapy, due to the sharp distal SOBP dose edge and the sensitivity for heterogeneities characteristic for proton particles.

From radiotherapy with photons the concept of CTV–PTV margins has emerged. The purpose of the margin is to ensure sufficient dose coverage to the CTV, despite the random and systematic variations that occur during the course of treatment. The margins are often determined on the basis of institution dependent knowledge about the distribution of setup errors and organ motion for different treatment regions (11, 58). However, the results from the present study confirm that this strategy cannot fully be adopted in order to manage uncertainties in proton therapy. The geometrical errors itself are modality independent and possible to be managed with a CTV-PTV margin. However, as demonstrated, setup errors can cause large density changes in the beam path. The effect that differences between calculated and actual density in a treatment situation will have on the proton particle range, necessitates an additional margin in the beam direction. This implies different CTV-PTV margins laterally and in depth, with the consequence that PTV would have to be designed individually for each beam direction (19). With the passive scattering technique, the PTV is discarded and instead the field parameters are determined relative to the CTV. The managing of uncertainties is solved by building the uncertainty margins into the field- and patient-specific blocks and compensators for each beam direction (38). With the active scanning technique, the concept of beam specific PTVs has been investigated and performed favourable compared to the conventional PTV consept, however, this approach is, at present time, only applicable in single field optimized treatment plans (59). Considering IMPT and the managing of the uncertainty issues, work has been done for implementing range and setup uncertainties into the IMPT optimization process. This is referred to as robust optimization (28).

It is a strength to this study that the method used to simulate and estimate the potential effects of the range- and setup errors, is well known, evaluated and recommended as a simple and useful tool for analysing the sensitivity of a treatment plan for the specified errors (13, 14, 60).

This study has however some limitations. Firstly, only single errors were considered, which do not fully reflect the reality in a clinical situation where the patient position, the patient geometry and the density composition is a product of combination of rotational errors, setup errors, interfield errors, organ motion, range errors and anatomical deformations. Secondly, only a few selected errors were studied, applying a small study group, this limits the strengths of the results.

6 CONCLUSION AND OUTLOOK

In this study the effects of density changes in the beam path, setup errors and calibration curve errors were investigated. The study showed that the density changes could cause severe alterations of the proton range. No large reductions in the 95% dose coverage to the target volumes were found, following the introduction of calibration curve errors or setup errors. However, in areas of complex tissue density heterogeneities error-induced dose disturbances occurred with increased amount of hotspots and cold spots. For OAR in close proximity to the target volumes, large increase in doses was observed.

Several interesting challenges regarding craniospinal treatment plans could be addressed in future projects:

- The investigation of the sensitivity of the junction area in craniospinal treatment plans for interfield motions.
- The investigation of the potential effects of rotational errors and organ motions on the proton dose distribution in craniospinal treatment plans.
- The investigation of robustness optimization methods in craniospinal treatment planning.

In addition; the variation in patient anatomy is one of the most important uncertainties in proton therapy, and could cause large changes in the delivered dose distribution compared to the planned dose distributions. Studies, with the aim of developing adaptive strategies to deal with anatomical changes should be conducted.

Bibliography

1.   Intensity Modulated Radiation Therapy Collaborative Working G. Intensity-modulated radiotherapy: current status and issues of interest. International journal of radiation oncology, biology, physics. 2001 Nov 15;51(4):880-914. PubMed PMID: 11704310.

2.   Yu CX. Intensity-modulated arc therapy with dynamic multileaf collimation: an alternative to tomotherapy. Physics in medicine and biology. 1995 Sep;40(9):1435-49. PubMed PMID: 8532757.

3.   Wilson RR. Radiological use of fast protons. Radiology. 1946 Nov;47(5):487-91. PubMed PMID: 20274616.

4.   Particle Therapy Co- Operative Group Available from: http://ptcog.web.psi.ch/.

5.   Allen AM, Pawlicki T, Dong L, Fourkal E, Buyyounouski M, Cengel K, et al. An evidence based review of proton beam therapy: The report of ASTRO's emerging technology committee. Radiotherapy and Oncology. 2012 4//;103(1):8-11.

6.   Howell RM, Giebeler A, Koontz-Raisig W, Mahajan A, Etzel CJ, D'Amelio AM, Jr., et al. Comparison of therapeutic dosimetric data from passively scattered proton and photon craniospinal irradiations for medulloblastoma. Radiation oncology. 2012;7:116. PubMed PMID: 22828073. Pubmed Central PMCID: 3430590.

7.   Yoon M, Shin DH, Kim J, Kim JW, Kim DW, Park SY, et al. Craniospinal irradiation techniques: a dosimetric comparison of proton beams with standard and advanced photon radiotherapy. International journal of radiation oncology, biology, physics. 2011 Nov 1;81(3):637-46. PubMed PMID: 20932690.

8.   Oeffinger KC, Mertens AC, Sklar CA, Kawashima T, Hudson MM, Meadows AT, et al. Chronic health conditions in adult survivors of childhood cancer. The New England journal of medicine. 2006 Oct 12;355(15):1572-82. PubMed PMID: 17035650.

9.   Seeram E. Computed tomography : physical principles, clinical applications and quality control. 3rd ed. Philadelphia: W.B. Saunders; 2009. XIX, 536 s. p.

10.   Langen KM, Jones DT. Organ motion and its management. International journal of radiation oncology, biology, physics. 2001 May 1;50(1):265-78. PubMed PMID: 11316572.

11.   van Herk M. Errors and margins in radiotherapy. Semin Radiat Oncol. 2004 Jan;14(1):52-64. PubMed PMID: 14752733.

12.   Arjomandy B. Evaluation of patient residual deviation and its impact on dose distribution for proton radiotherapy. Medical dosimetry : official journal of the American Association of Medical Dosimetrists. 2011 Autumn;36(3):321-9. PubMed PMID: 21074402.

13.   Lomax AJ. Intensity modulated proton therapy and its sensitivity to treatment uncertainties 2: the potential effects of inter-fraction and inter-field motions. Physics in medicine and biology. 2008 Feb 21;53(4):1043-56. PubMed PMID: 18263957. Epub 2008/02/12. eng.

14.   Lomax AJ. Intensity modulated proton therapy and its sensitivity to treatment uncertainties 1: the potential effects of calculational uncertainties. Physics in medicine and biology. 2008 Feb 21;53(4):1027-42. PubMed PMID: 18263956. Epub 2008/02/12. eng.

15.   Graham DT, Cloke PJ. Principles of radiological physics. 4th ed. Edinburgh ; New York: Churchill Livingstone; 1996. 448 p. p.

16.   Ytre-Hauge K, Universitetet i Bergen . Institutt for fysikk. Measurements and Monte Carlo simulations of neutron doses from radiation therapy with photons, protons and carbon ions. [Bergen]: University of Bergen; 2013. XII, 128 s. p.

17.   Leo WR. Techniques for nuclear and particle physics experiments : a how-to approach. 2nd rev. ed. Berlin: Springer; 1994. XVIII, 378 s. p.

18.   NIST. PSTAR - stopping-power and range tables for protons: National Institute of Standards and Technology. Available from: http://physics.nist.gov/PhysRefData/Star/Text/PSTAR.html.

19.   International commission on Radiation Units and Measurements I. ICRU Report 78: Prescribing, recording and reporting proton-beam therapy. Journal of the ICRU: 2007.

20.   Gottschalk B. Physics of Proton Interactions in Matter. In: Paganetti H, editor. Series in medical physics and biomedical engineering. Boca Raton, FL: CRC Press/Taylor & Francis; 2012. p. 1 online resource (s 20-58).

21.   Podgorsak EB. Radiation Physics for Medical Physicists. Berlin, Heidelberg: Springer-Verlag Berlin Heidelberg; 2010.

22.   Bomford CK, Miller H, Kunkler IH, Sheriff SB, Walter J. Walter and Miller's textbook of radiotherapy : radiation physics, therapy and oncology. 5th ed. Edinburgh: Churchill Livingstone; 1993. 607 s. p.

23.   Goitein M, SpringerLink (Online service). Radiation Oncology: A Physicist's-Eye View. New York, NY: Springer Science+Business Media, LLC; 2008.

24.   Purdy JA, Poortmans P, Perez CA, Levitt SH. Physics of Radiotherapy Planning and Delivery. In: Levitt SH, Purdy JA, Perez CA, Poortmans P, SpringerLink (Online service), editors. Technical Basis of Radiation Therapy Practical Clinical Applications. Berlin, Heidelberg: Springer Berlin Heidelberg; 2012.

25.   Purdy JA, Poortmans P, Perez CA. Three-Dimentional Treatment Planning and Conformal Therapy. In: Levitt SH, Purdy JA, Perez CA, Poortmans P, SpringerLink (Online service), editors. Technical Basis of Radiation Therapy Practical Clinical Applications. Berlin, Heidelberg: Springer Berlin Heidelberg; 2012.

26.   Otto K. Volumetric modulated arc therapy: IMRT in a single gantry arc. Medical physics. 2008 Jan;35(1):310-7. PubMed PMID: 18293586.

27.   Korea NCCi. Proton Therapy Facility.

28.   Trofimov A, Unkelbach J, Craft D. Treatment-Planning Optimization. In: Paganetti H, editor. Proton therapy physics. Series in medical physics and biomedical engineering. Boca Raton, FL: CRC Press/Taylor & Francis; 2012. p. 1 online resource (s 461-87).

29.   Sloepsema R. Beam Delivery Using Passive Scattering. In: Paganetti H, editor. Proton therapy physics. Series in medical physics and biomedical engineering. Boca Raton, FL: CRC Press/Taylor & Francis; 2012. p. 1 online resource (s 422-54.).

30.   Varian Medical Systems I. Eclipse 11: Proton Planning Dosimetry. U.S.A: Varian Medical Systems. Inc. Palo Alto, CA, U.S.A; 2012.

31.   Lomax A. Physics of Treatment Planning Using Scanned Beams. In: Paganetti H, editor. Proton therapy physics. Series in medical physics and biomedical engineering. Boca Raton, FL: CRC Press/Taylor & Francis; 2012. p. 1 online resource (s 335-79).

32.   Kelada O. The potential advantages and disadvantages of cancer therapy using charged particles compared with megavoltage x-rays: Particle Therapy Cancer Research Institute. Available from: http://www.ptcri.ox.ac.uk/about/literaturereview.shtml.

33.   Schneider U, Pedroni E, Lomax A. The calibration of CT Hounsfield units for radiotherapy treatment planning. Physics in medicine and biology. 1996 Jan;41(1):111-24. PubMed PMID: 8685250.

34.   Schaffner B, Pedroni E. The precision of proton range calculations in proton radiotherapy treatment planning: experimental verification of the relation between CT-HU and proton stopping power. Physics in medicine and biology. 1998 Jun;43(6):1579-92. PubMed PMID: 9651027.

35.   Espana S, Paganetti H. The impact of uncertainties in the CT conversion algorithm when predicting proton beam ranges in patients from dose and PET-activity distributions. Physics in medicine and biology. 2010 Dec 21;55(24):7557-71. PubMed PMID: 21098912.

36.   Palta J, Yeung D. Precision and Uncertainty in Proton Therapy for Nonmoving Targets. In: Paganetti H, editor. Proton therapy physics. Series in medical physics and biomedical engineering. Boca Raton, FL: CRC Press/Taylor & Francis; 2012. p. 1 online resource (s 413-33).

37.   Varian Medical Systems I. Eclipse Reference Guide, Treatment Planning for Proton Beam: Varian Medical Systems, Inc. 3100 Hansen Way

Palo Alto, CA 94304-1030, USA; 2011.

38.   Moyers MF, Miller DW, Bush DA, Slater JD. Methodologies and tools for proton beam design for lung tumors. International journal of radiation oncology, biology, physics. 2001;49(5):1429-38.

39.   Engelsman M. Physics of Treatment Planning for Single-Field Uniform Dose. In: Paganetti H, editor. Proton therapy physics. Series in medical physics and biomedical engineering. Boca Raton, FL: CRC Press/Taylor & Francis; 2012. p. 1 online resource (s 305-33).

40.   Paganetti H. Range uncertainties in proton therapy and the role of Monte Carlo simulations. Physics in medicine and biology. 2012 Jun 7;57(11):R99-117. PubMed PMID: 22571913. Pubmed Central PMCID: 3374500.

41.   Varian Medical Systems I. Proton Algorithm Reference Guide: Varian Medical Systems, Inc. 3100 Hansen Way

Palo Alto, CA 94304-1030, USA; 2011.

42.   McGowan SE, Burnet NG, Lomax AJ. Treatment planning optimisation in proton therapy. The British journal of radiology. 2013 Jan;86(1021):20120288. PubMed PMID: 23255545.

43.   Lomax A. Intensity modulation methods for proton radiotherapy. Physics in medicine and biology. 1999 Jan;44(1):185-205. PubMed PMID: 10071883. Epub 1999/03/11. eng.

44.   Feuvret L, Noel G, Mazeron JJ, Bey P. Conformity index: a review. International journal of radiation oncology, biology, physics. 2006 Feb 1;64(2):333-42. PubMed PMID: 16414369.

45.   Levernes S. Volum og doser i ekstern stråleterapi - Definisjoner og anbefalinger. Østerås: Statens Strålevern, 2012.

46. Haukeland University Hospital DoOaMP. Prosedyre for CNS planlegging. 2010.

47. Brodin NP, Rosenschöld PMA, Aznar MC, Kiil-Berthelsen A, Vogelius IR, Nilsson P, et al. Radiobiological risk estimates of adverse events and secondary cancer for proton and photon radiation therapy of pediatric medulloblastoma. Acta oncologica. 2011;50(6):806-16. PubMed PMID: 21767178.

48. Cochran DM, Yock TI, Adams JA, Tarbell NJ. Radiation dose to the lens during craniospinal irradiation-an improvement in proton radiotherapy technique. International journal of radiation oncology, biology, physics. 2008 Apr 1;70(5):1336-42. PubMed PMID: 18029111.

49. Giebeler A, Newhauser WD, Amos RA, Mahajan A, Homann K, Howell RM. Standardized treatment planning methodology for passively scattered proton craniospinal irradiation. Radiation oncology. 2013 Feb 3;8(1):32. PubMed PMID: 23375151.

50. Eifel PJ, Donaldson SS, Thomas PR. Response of growing bone to irradiation: a proposed late effects scoring system. International journal of radiation oncology, biology, physics. 1995 Mar 30;31(5):1301-7. PubMed PMID: 7713789.

51. Measurements IcoRUa. ICRU Report 83 Prescribing, Recording, and Reporting Photon-Beam Intensity-Modulated Radiation Therapy (IMRT). Journal of the ICRU: 2010.

52. Goitein M. A technique for calculating the influence of thin inhomogeneities on charged particle beams. Medical physics. 1978 Jul-Aug;5(4):258-64. PubMed PMID: 683162.

53. Paulino AC. Hypothyroidism in children with medulloblastoma: a comparison of 3600 and 2340 cGy craniospinal radiotherapy. International journal of radiation oncology, biology, physics. 2002 Jul 1;53(3):543-7. PubMed PMID: 12062595.

54. Packer RJ, Cogen P, Vezina G, Rorke LB. Medulloblastoma: clinical and biologic aspects. Neuro-oncology. 1999 Jul;1(3):232-50. PubMed PMID: 11550316. Pubmed Central PMCID: 1920747.

55. Freeman T. The potential of proton CT http://medicalphysicsweb.org/cws/article/research/53211: IOP publishing; 2013. Available from: http://medicalphysicsweb.org/cws/article/research/53211.

56. Sawakuchi GO, Titt U, Mirkovic D, Mohan R. Density heterogeneities and the influence of multiple Coulomb and nuclear scatterings on the Bragg peak distal edge of proton therapy beams. Physics in medicine and biology. 2008 Sep 7;53(17):4605-19. PubMed PMID: 18678928.

57.   Urie M, Goitein M, Holley WR, Chen GT. Degradation of the Bragg peak due to inhomogeneities. Physics in medicine and biology. 1986 Jan;31(1):1-15. PubMed PMID: 3952143.

58.   van Herk M, Remeijer P, Rasch C, Lebesque JV. The probability of correct target dosage: dose-population histograms for deriving treatment margins in radiotherapy. International journal of radiation oncology, biology, physics. 2000 Jul 1;47(4):1121-35. PubMed PMID: 10863086.

59.   Park PC, Zhu XR, Lee AK, Sahoo N, Melancon AD, Zhang L, et al. A Beam-Specific Planning Target Volume (PTV) Design for Proton Therapy to Account for Setup and Range Uncertainties. International journal of radiation oncology, biology, physics. 2012;82(2):e329-e36.

60.   Albertini F, Hug EB, Lomax AJ. Is it necessary to plan with safety margins for actively scanned proton therapy? Physics in medicine and biology. 2011 Jul 21;56(14):4399-413. PubMed PMID: 21709340. Epub 2011/06/29. eng.